LINEAR POLARIZATION OF AGN JETS

A Dissertation

Submitted to the Faculty

of

Purdue University

by

Mary Ann Hodge

In Partial Fulfillment of the

Requirements for the Degree

of

Doctor of Philosophy

May 2019

Purdue University

West Lafayette, Indiana

THE PURDUE UNIVERSITY GRADUATE SCHOOL
STATEMENT OF DISSERTATION APPROVAL

Dr. Matthew Lister, Chair

Department of Physics and Astronomy

Dr. Kyoung-Soo Lee

Department of Physics and Astronomy

Dr. Maxim Lyutikov

Department of Physics and Astronomy

Dr. Martin Kruczenski

Department of Physics and Astronomy

Approved by:

Dr. John Finley

Head of the Department Graduate Program

TABLE OF CONTENTS

Page

LIST OF TABLES

LIST OF FIGURES

Figure Page

Figure Page

ABSTRACT

Hodge, Mary Ann Ph.D., Purdue University, May 2019. Linear Polarization of AGN Jets. Major Professor: Matthew Lister.

Active galactic nuclei (AGN) jets are energetic phenomena where twin jets of plasma emerge perpendicular to the plane of the accretion disk surrounding supermassive black holes in galactic centers. Radio-loud jets are largely divided into classes based on the angle of observation (blazars versus radio galaxies), spectral line widths (Flat Spectrum Radio Quasars/FSRQs versus BL Lac objects/BL Lacs), and location of the synchrotron peak frequency in their spectral energy distribution (high-spectral peaked/HSP, intermediate-spectral peaked/ISP, or low-spectral peaked/LSP).

The linear fractional polarization of the radio emission and the direction of the polarization plan (electric vector position angle, "EVPA") can be measured, providing information on the properties of the jets' magnetic field. This study uses and describes some processing of data from the MOJAVE program, taken with the VLBA at 15 GHz, to investigate the polarization behavior of 387 AGN.

The most polarized jets have good alignment between the EVPA and the local jet direction, and higher stability in both fractional polarization and the EVPA. This characterization best describes BL Lacs, which are notably different from FSRQs. HSP BL Lacs have lower fractional polarization than LSP BL Lacs, with fractional polarization partially dependent on apparent jet speeds. These results have supported a scenario where HSP BL Lacs and LSP BL Lacs are similar objects with differing relativistic beaming factors, while FSRQs and BL Lacs as a class have inherent differences in the makeup of their magnetic fields.

1. Introduction

Relatively recent work suggests there are more than 2 trillion galaxies in the universe (Conselice et al., 2016). It is further thought that all, or at least most, of these galaxies have a supermassive black hole (SMBH) of $\approx 10^6 - - - 10^{10} M_\odot$ at their center. When the area surrounding these black holes is extraordinarily bright, they are called active galactic nuclei (AGN). This light is usually a product of the accretion disk and its surrounding gas, but 15-20 percent of AGN are radio-loud (Kellermann et al., 1989) with the radio emission primarily originating from relativistic twin jets of plasma emerging perpendicular to the plane of the accretion disk. These jets are often observed to be linearly polarized, which is the focus of this work.

1.1 AGN Jets

1.1.1 Basic Jet Properties

Astrophysical jets from AGN are extremely energetic phenomena, capable of extending kiloparsecs or even megaparsecs (Bagchi et al., 2014) outside the host galaxy at velocities that reach a significant fraction of the speed of light. The process by which jets are produced (and why they occur) is still mysterious, but is thought to involve magnetic fields generated through energy extraction of the accretion disk (Blandford and Payne, 1982) or black hole rotation (Blandford and Znajek, 1977). Most AGN — with the exception of one class discussed in Section 1.1.3 — are characterized by the following regions, shown in Figure 1.1: 1. a dusty torus, which surrounds the accretion disk ($\approx 10^{15}$ m from the black hole); 2. the broad line region (BLR), a series of fast-moving clouds named for their emission line widths, often obscured by the torus depending on the orientation of the observer ($\approx 10^{14}$ m); and 3.

the narrow line region (NLR), another series of slower clouds at a greater distance from the black hole and the torus ($\approx 10^{17}$ m) (Urry and Padovani, 1995).

Jets are extremely luminous. At γ-ray wavelengths, in the region of 100 MeV-300 GeV, they make up the large majority of sources away from the galactic plane (Ackermann et al., 2015). The typical spectral energy distribution (SED, a graph of frequency versus flux density) shows thermal emission over a large frequency range, and two noticeable bumps: one near infrared/X-ray wavelengths, and another in the γ-ray region. The former is thought to be a result of synchrotron radiation. The latter is a matter of some debate, specifically whether its origin is leptonic or hadronic. The leptonic scenario posits that the higher energy emission is produced by inverse Compton scattering, using the same electrons that produce the lower energy synchrotron radiation. The necessary photons could come from the original synchrotron process — which is called synchrotron self-Compton (SSC, Bloom and Marscher 1996) — or from one of the regions of gas and dust in the vicinity of the jet, which is called external Compton (EC). In the hadronic scenario, there is an unknown mixture of proton-synchrotron processes and those involving pions produced by the energetic protons (Mannheim and Biermann, 1992; Mannheim, 1993).

1.1.2 Relativistic Effects

The bulk flow velocities of AGN jets are known to reach high Lorentz factors, so it is necessary to briefly cover the ways in which the emitted photons are altered by relativistic effects. I will begin with superluminal motion, the phenomenon where luminous objects can appear to move faster than light. This is due to the emitting object "chasing" its own photons. Consider a case where some source ejects a relativistic luminous feature at speed v and angle θ relative to the line of sight, where $\theta = 0$ corresponds to the feature pointing directly at the observer. The feature emits a set of photons at time $t = 0$, and another set at time t. For the two groups of photons, the difference in distance along the line of sight at time t is $ct - vt\cos\theta$, which

can be divided by c to find the difference in arrival times to the observer. During this period, the apparent distance traveled by the feature across the sky is $vt\sin\theta$. The observed speed will therefore be:

$$v_{obs} = \frac{vt\sin\theta}{(t - \frac{v}{c}t\cos\theta)}. \tag{1.1}$$

The can be simplified in terms of $\beta = v/c$ to find an expression for the apparent speed:

$$\beta_{app} = \frac{\beta\sin\theta}{1 - \beta\cos\theta}. \tag{1.2}$$

For large v and small θ, β_{app} will exceed c. Scientific concerns related to superluminal motion are covered in Chapter 4.

Relativistic beaming and aberration also affect which photons are observed. The equation

$$\cos\theta = \frac{\cos\theta' + \beta}{1 + \beta\cos\theta'} \tag{1.3}$$

describes the relationship between the viewing angle in the observer frame (θ) and viewing angle in the rest frame (θ') (Gabuzda, 2015). This means that we can receive photons that may be emitted sideways or even backwards with respect to the jet velocity frame. If a photon is emitted perpendicular to the motion in the rest frame ($\theta' = \pi/2$), $\cos\theta$ will be equal to β. Then

$$\sin\theta = \frac{1}{\Gamma}, \tag{1.4}$$

(Gabuzda, 2015) where Γ is the Lorentz factor $(1 - \beta^2)^{-1/2}$. For large $\Gamma/\beta \approx 1$, $\theta \approx 1/\Gamma$. For an object emitting isotropically and relativistically, the radiation will be beamed into a cone with a half-angle $1/\Gamma$. The observer will accordingly receive a larger amount of flux than if the object was stationary; the specific intensity will be transformed as $I_\nu(\nu) = \delta^3 I'_{\nu'}(\nu')$ (Rybicki and Lightman, 1979), where δ is the Doppler factor

$$\delta = \frac{1}{\Gamma(1 - \beta\cos\theta)}. \tag{1.5}$$

All radio jets are thought to be relatively symmetric, with a mirrored jet emerging on the other side of the host galaxy's black hole. Other than in radio galaxies, which

have high θ, the "counterjet" is rarely seen since its radiation is largely beamed away from the observer.

Another concern is the transformation of time scales. The equation

$$\Delta t = \delta^{-1} \Delta t' \tag{1.6}$$

describes the relationship between the time interval measured in the source frame ($\Delta t'$) and the time interval measured in the observer frame (Δt) (Longair, 2011). The observed time interval will therefore be shorter than the time interval as measured in the source frame, especially for highly relativistic jets seen close to the line of sight.

1.1.3 Classification Schema

One of the primary ways to classify AGN jets is by viewing angle, rather than inherent properties. The reasons for this are due to AGN morphology and the relativistic beaming outlined above. When viewed side-on, the dusty torus can completely absorb emission from the BLR, leading to the general type 1/type 2 dichotomy for radio weak and quiet AGN (Urry and Padovani, 1995).

For radio-loud AGN with relativistic jets, the angle between the line of sight and the jet greatly affects the observed flux density. "Radio galaxies" are the relatively weaker objects in terms of flux, viewed at a larger angle to the line of sight. They are further divided by the Fanaroff-Riley classification (Fanaroff and Riley, 1974) which splits them into two categories: FR-I and FR-II. FR-I galaxies are sometimes called "low-power" and are thought to have slower flow speeds (Bicknell et al., 1990), but their main identifier is rapidly decreasing luminosity as the jet travels farther from the nucleus of its host galaxy (they are "edge-darkened.") FR-II galaxies, on the other hand, are "edge-brightened," as they terminate in bright hotspots where the jet collides with the intergalactic medium.

Jets viewed almost head-on are called "blazars" and are extremely bright due to relativistic beaming. Blazars are also divided into two categories based on the strength of their optical emission lines. BL Lac objects (named after the blazar

BL Lacertae), in contrast to flat spectrum radio quasars (FSRQs), have featureless spectra (rest frame emission line widths under 5 Angstroms); BL lacs are thought to lack a BLR, perhaps due to differences in the radiative efficiency of their accretion disks (Ghisellini, 2016). This definition is not ideal — spectral line widths are not necessarily constant over time, and BL Lacertae itself does not always qualify as a BL Lac object (Vermeulen et al., 1995). Despite the presence of "intermediate" BL Lac/FSRQ objects and proposed alternative schema (Ghisellini et al., 2011), this division is the one most in use, with the classes still generally being distinct across several statistics such as the ones discussed in Chapter 3. Current radio unification theory (Urry and Padovani, 1995) is that BL Lacs and FSRQs are the beamed, small-viewing angle counterparts of FR-I and FR-II radio galaxies, respectively.

Beyond these classes, blazars are sometimes further (or alternatively) divided by the location of their synchrotron SED peak. The three classes are: high-spectral peaked (HSP) with ν_p above 10^{15} Hz; intermediate-spectral peaked (ISP) with ν_p between 10^{14} Hz and 10^{15} Hz; and low-spectral peaked (LSP) with ν_p below 10^{14} Hz. The large majority of FSRQs are LSP, with BL Lacs being more evenly divided between synchrotron SED peak categories — HSP AGN are typically found at low redshifts, which are rare for FSRQs. HSP BL Lacs appear distinct from FSRQs in many of the same ways as other BL Lacs, but have properties (such as their radio variability and ratio of γ-ray to radio flux) which set them apart from LSP BL Lacs as well (Lister et al., 2011; Richards et al., 2014). The most accepted current theory is that HSP BL Lacs are truly BL Lacs, but consist of the least beamed within the population (Lister et al., 2011). Chapters 3 and 4 further address this model.

The majority of this work concerns blazars, with emphasis on the polarization differences between BL Lacs and FSRQs. The behavior of blazar polarization is thought to be at least somewhat deterministic (i.e., not totally stochastic; see Kiehlmann et al. 2016), but there is no clear consensus on which model(s) are correct. By studying the polarization in greater detail, the possible explanations can be further constrained, leading to a better understanding of how jets work in general.

1.2 Linear Polarization

1.2.1 Polarization of Jets

In astronomy, it is common to express the polarization characteristics of light in terms of Stokes parameters (Stokes, 1851). The four parameters are I, Q, U, and V, with I representing total intensity/the sum of all states, Q and U representing linear polarization at 90 degrees and 45 degrees, respectively, and V representing circular polarization. The degree of circular polarization in jets is generally much lower than the degree of linear polarization, and all further discussion of "polarization" will refer to linear polarization unless otherwise specified. Stokes I is always positive, but the other parameters have a sign which depends on direction — for example, a negative Q signifies linear polarization oriented more vertically than horizontally. We then use two main characteristics to describe polarization. They are fractional polarization, often abbreviated as m, and the electric vector position angle (EVPA, also occasionally called the polarization angle). In Stokes parameters, they are:

$$m = \frac{\sqrt{U^2 + Q^2}}{I} \tag{1.7}$$

and

$$EVPA = \frac{1}{2}\arctan(\frac{U}{Q}). \tag{1.8}$$

The EVPA is taken as degrees from north towards east, purely by convention. Because the EVPA represents the orientation of a plane, it has an ambiguity in π such that, for example, 0° and 180° are the same EVPA.

Since synchrotron radiation is the mechanism by which radio emission is produced in jets, it follows that polarization is a commonly seen feature. Theoretically, linear polarization from synchrotron radiation can reach as high as 70 percent, but in practice there are relatively few jets with measured values exceeding a few tens of percent. The jet core, or brightest feature at the base of the jet for a given wavelength (see Section 2.1.2), is less polarized than jet features further downstream (with "downstream" meaning farther away from optically thick regions closer to the black hole.)

This is likely due to magnetic fields becoming better ordered with distance down the jet, and possibly less depolarization by dense gas. Polarization quantities, and even general intensity, are highly variable and can change on minute timescales (Meyer et al., 2019).

In the blazar regime, BL Lacs tend to be more polarized than FSRQs and have EVPAs with more predictable behavior (Cawthorne et al., 1993; Lister and Homan, 2005). Explanations for this pattern include jet speeds and related shock strengths (Lister and Homan, 2005), slight viewing angle differences (Agudo et al., 2014), and the rate of emerging new features (Gabuzda et al., 2000). In an ideal scenario, the observed EVPA would be perpendicular to the magnetic field, but this cannot always be taken as true for measured AGN jet EVPAs due to relativistic effects (Lyutikov et al., 2005). Still, EVPAs are a useful tool for discovering the nature of magnetic fields in jets; in particular, EVPAs are an indicator of an underlying magnetic field structure, either helical or toroidal (Gabuzda, 2003). These possibilities are investigated with data in Chapters 3 and 4.

1.2.2 Measurement Complications

Besides relativistic effects, there are several other factors that must be considered when analyzing polarization data. Faraday rotation occurs when the polarized light passes through a magnetized medium, rotating the plane of linear polarization (described in Burn 1966.) For jets, this medium can be internal jet plasma, or the interstellar medium between the jet and the observer. For a jet with an intrinsic EVPA $EVPA_0$, its observed EVPA is given by

$$EVPA_{obs} = EVPA_0 + RM\lambda^2 \tag{1.9}$$

where λ refers to wavelength. The rotation measure (RM) is a measure of the degree of the rotation, with

$$RM = \frac{e^3}{8\pi^2\epsilon_0 m^2 c^3} \int n_e B \cdot dl \tag{1.10}$$

where e is electron charge, ϵ_0 is the permittivity of free space, m is electron mass, c is the speed of light, n_e is electron charge density, B is the magnetic field, and dl is the path length from the observer to the source. The RM can be estimated by measuring the EVPA simultaneously at different wavelengths.

The presence of helical or toroidal magnetic fields would cause a Faraday rotation gradient perpendicular to the jet, a topic of multiple studies (Gabuzda et al., 2004; Asada et al., 2002). Depolarization can occur as a result of Faraday rotation (Burn, 1966), or when regions of orthogonal polarizations are combined within the finite angular size of the interferometric restoring beam.

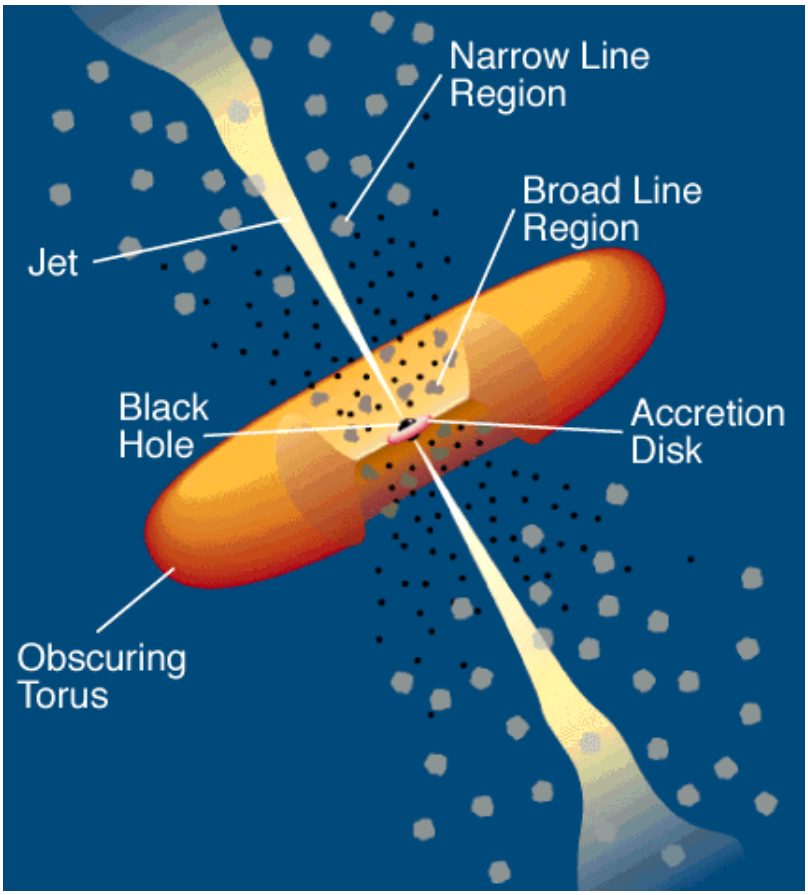

Figure 1.1. Schematic of the standard AGN model based on Urry and Padovani 1995.

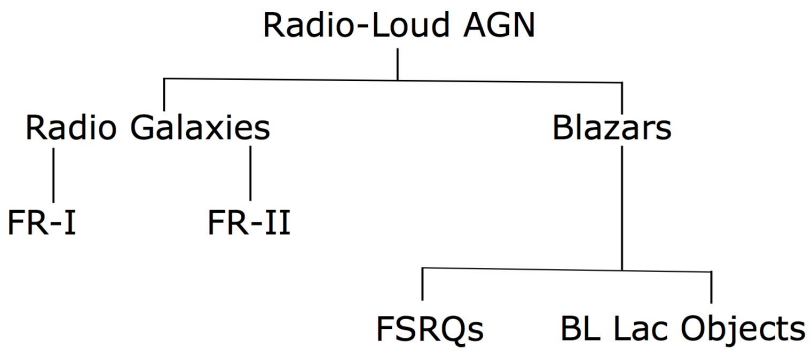

Figure 1.2. Classification scheme for types of radio-loud AGN.

2. Instrumentation and Data Reduction

2.1 Observing with the VLBA

2.1.1 The VLBA

The majority of measurements described in this thesis have been made with the VLBA (Very Long Baseline Array), a radio interferometer operated by the National Radio Astronomy Observatory (NRAO). The VLBA consists of ten, 25 meter telescopes spread across the United States from the Virgin Islands to Hawaii. Through VLBI (very long baseline interferometry), the VLBA can achieve a higher resolution than any single-aperture telescope.

Each telescope observes the same object in the sky; the signal arrives at slightly different times due to the different geographical locations of each antenna. The amplitudes and phases of the incoming radio signals are combined in pairs to yield "visibilities" as a function of the projected baseline (u, v) coordinates, based on the relative orientation and distance between the antennas (Cornwell et al., 1999). These are a function of time since, as the Earth rotates, the antenna locations change relative to the observed source. This process produces a sampling of the true visibility function, $V(u, v)$, which is a Fourier transform of the source intensity distribution convolved with the primary beam (Clark, 1999). The largest antenna baseline determines the resolution of the interferometer, and the number and spacing of the antennas determine the quality of the sampling (and thus the final image).

The "CLEAN" imaging algorithm is used to deconvolve the intrinsic intensity distribution of the source and the synthesized beam (Högbom, 1974). Further description of the general calibration procedures is available in the AIPS (Astronomical Image Processing System) Cookbook (http://www.aips.nrao.edu/cook.html), with specific description of the polarization calibration in Section 2.2.1

2.1.2 MOJAVE Polarized Images

The data in this thesis are mainly associated with the MOJAVE (Monitoring of Jets in Active galactic nuclei with VLBA Experiments) program (Lister and Homan, 2005). While MOJAVE began in 2002, archival observations have allowed us to investigate hundreds of AGN over a period of >20 years. The list of monitored AGN includes several samples chosen on the basis of radio flux density, *Fermi*-LAT γ-ray energy flux, or inclusion in other monitoring samples; for a full list of current and previously monitored sources, see http://www.physics.purdue.edu/astro/MOJAVE.

The length of time between MOJAVE observations of a particular source is dependent on the jet's angular expansion speed. Especially for the study of polarization, the topic of this thesis, consistent monitoring is desirable. The EVPA in particular possesses an n-π ambiguity, such that 0° and 180° are equivalent. If the EVPA is observed infrequently, "swings" in the EVPA, also known as rotation events, may be missed. Another concern is determining the direction of EVPA swings. A rotation 89° west may be confused for a rotation 91° east, but frequent observations lower the odds of such large angle changes occurring during observational gaps. For example, Abdo et al. 2010b reported a 208° rotation including a gap of almost 90° in 1253−055/3C 279; Kiehlmann et al. 2016 later claimed that with additional observations of the same period, the EVPA was revealed to change direction instead of undergoing a long continuous rotation. Consistent, frequent observations from the University of Michigan Astronomy Observatory (UMRAO) single 25m telescope data archive shows behavior that is missing or unclear using MOJAVE observations alone. An example is the rotation of 3C 446/2223-052 beginning in 2010, shown in Figure 2.1. Our observations, spaced roughly half a year apart, show steady behavior while the UMRAO data indicate a fairly continuous clockwise rotation.

On the other hand, MOJAVE serves a unique purpose due to the high resolution of the produced images. With VLBI, MOJAVE is often able to resolve the core from extended jet emission. From a polarization perspective, this is important for

understanding the structure of the jet and for recognizing new features (or knots of emission, also called "components") emerging from the core, which can rotate the EVPA and alter the fractional polarization (Cohen et al., 2018). While the core feature typically dominates blazar radio emission, the core polarization as measured by MOJAVE does not always match the polarization measured with lower angular resolution telescopes, due to these features or Faraday depolarization from the jet and surrounding area. For an example of this, see Figures 2.2 and 2.3.

Part of my study has been to produce images similar to Figure 2.4. The left-most object is an image of BL Lac with contour lines representing the total intensity (the unpolarized version of the image, with a total intensity color scale, is shown in Figure 2.5). The colors superimposed on the contour lines represent the fractional polarization. On the right is a copy of the BL Lac image, but with the direction of the EVPA superimposed instead of the fractional polarization color scale. The spurious polarization (the EVPA lines existing outside of the intensity contours) is mainly due to imperfect correction of the antenna leakage terms (see Section 2.2.1). These errors in polarization result in more overall error in regions where the total intensity is low. Further description of the image details is available in Lister et al. 2018, with some discussion in Section 3.1.

The compact feature near the top of the image in Figure 2.4 is the core. This is typically thought to be the point where the jet becomes optically thin, but it is not necessarily the true base of the jet, in the close vicinity of the black hole (see e.g. Marscher 2016 and references therein). A "core shift" effect exists, in which the position of the radio core changes based on observing frequency (Marcaide and Shapiro, 1984). This is likely due to opacity associated with synchrotron self-absorption (Konigl, 1981). The effect is exponential (Sokolovsky et al., 2011), and past a certain turnover frequency dependent on the jet, the full structure is optically thin to high-frequency radio observations.

In Figure 2.4, BL Lac bends to the southwest before another bend to the southeast. Although jets represent enormous amounts of energy and force, they often appear

curved or bent rather than straight. Blazars especially have small intrinsic opening angles (Pushkarev et al., 2017), meaning that we are looking down a very narrow cone of emission; bends are therefore highly exaggerated by projection effects. Some jets may also simply be bent intrinsically, due to factors related to the black hole or to the local (especially parsec-scale) environment (Kharb et al., 2010). Since the MOJAVE sample is largely determined by radio flux density, and emission towards our line of sight is relativistically boosted, the sample may be biased towards jets which have some feature pointed in our direction at some time (Kharb et al., 2010). The "at some time" clause is key because moving features within the jet do not always follow the same apparent path outward (Lister et al., 2013a). Currently, precession of the accretion disk is thought to be the most likely cause of jet "wobbling" (Agudo, 2009).

2.2 Data Reduction

2.2.1 Archival Polarization Calibration

MOJAVE has also made use of VLBA archival data which was not taken as part of the MOJAVE program. Unlike the MOJAVE observations, polarization calibration for this archival data was not originally included in the immediate, standard reduction process. The addition of data is useful in general, but in particular, the archival observations are useful for interpreting the long-term behavior. While AGN are variable on short-term timescales, they are also known to be variable on time scales of years or even decades (Hovatta et al., 2007). Some AGN exhibit stable EVPAs for years before rotation events or long periods of unrest, and flares in fractional polarization may be rare or short-lived such that long-term observing is necessary to find them. The beginning of my thesis work was therefore spent creating polarized images from these archival observations.

I calibrated these observations one epoch at a time, with each archival epoch usually including observations of multiple AGN. The first step to creating polarized images was to check that a particular epoch was compatible with MOJAVE standards.

I began by confirming that the observation used two feeds (or detectors) of orthogonal circular polarization (RR and LL for "right" and "left") and that the correlator output included polarization cross-hands "LR" and "RL". These are necessary to gain information on all Stokes parameters (see Cotton 1999 for details). Next, I looked at the time coverage of the ten antennas. It was not uncommon for an antenna to be down for part of the observation due to unexpected problems such as poor weather. Eight of the antennas are in the mainland U.S., with the other two on Maunakea in Hawaii and in St. Croix in the U. S. Virgin Islands. These final two are especially important to establish long baselines for adequate (u, v) coverage. I did not process an epoch if either of these two telescopes was absent for over half the observing time. It was also necessary to check that the range and the location of the frequency bands was consistent with other MOJAVE observations, which are centered at 15.3 GHz. If any of these qualifications were not met, I did not process the epoch further.

The next step was running general calibration procedures with AIPS, the standard VLBA software. The relevant AIPS tasks for this thesis are "LPCAL" and "CLCOR," necessary to correct for instrumental polarization caused by "leakage" of one hand of circular polarization into the other orthogonal feed. This leakage can be modeled and is referred to as the instrumental leakage terms, or "D-terms" (Roberts et al., 1984). The antennas have altitude-azimuth mounts, and as the AGN is tracked across the sky, the EVPAs of the true AGN emission rotates. The contribution from instrumental polarization remains constant, however. The LPCAL algorithm uses this fact to subtract a simple polarization model from the data and determine the resulting leakage coefficients (each having a real and imaginary part) at each VLBA antenna.

Next, I plotted these leakage terms, with an example shown in Figure 2.6. ("IF" is short for intermediate frequency, which represents a frequency sub-band of the full observed bandwidth either in RR or LL; see Thompson 1999). The letters correspond to the leakage coefficients gained from running LPCAL on a particular source; the white crosses represent the median of these coefficients for each antenna IF. Since

the leakage coefficients are only dependent on the antenna and its receiver system, ideally all sources in Figure 2.6 should have the same coefficients. In the particular case graphed, the correction was poor for 3C 279/1253-055 at antenna "NL". This is because 3C 279 is generally a poor calibrator; it has a complex polarization structure, but the LPCAL algorithm assumes a simple model consisting of the core and one or two polarized features. When a source appeared consistently in disagreement with the other sources across multiple antennas, it was removed from the median calculation. Beyond complicated polarization structure, this could also occur for various other reasons such as a source having low flux or being at a low declination.

The final step was correcting for an instrumental rotation of the EVPA. Prior to upgrades on the VLBA hardware, the leakage terms remained somewhat stable over time. As discussed in Gomez et al. 2002, they could drift or experience sudden change due to receiver upgrades, weather concerns including seasonal temperature changes, and similar factors, but the majority of antennas experienced slow change. After finding the D-term coefficients in the paragraph above, I plotted their imaginary phase terms against the ones from previous epochs. By rotating them with different EVPAs until they matched the previous epoch at several stable antennas, I was able to find the correct relative EVPA correction, since the leakage terms can be assumed to not vary over a short time period. An example of what this looked like is shown in Figure 2.7, which shows the left circular and right circular leakage terms of one IF of one antenna. For the first (or "reference") epoch, an absolute EVPA correction is required. This was found by using the UMRAO, and comparing observations of the EVPA of several sources with approximately simultaneous measurements using the VLBA.

The D-term corrections were occasionally too poor to create images, perhaps due to poor weather conditions, missing antennas, or a lack of appropriate calibrators. The phases for observations with two IFs (rather than the standard four) were difficult to match with previous epochs, so these were set aside for later comparison against each other. For the remainder, I applied the found EVPA correction to the data in

AIPS with CLCOR. After, I output the final, corrected data with AIPS and imaged it, choosing appropriate total intensity and polarization contours.

2.2.2 Data Finalization

Beyond calibrating archival observations, I also performed various tasks to prepare the images and data for publication (Lister et al., 2018). Part of this work was similar to the data calibration process, in the sense that I used self-consistency between epochs. While the EVPA is generally highly variable — this is discussed in greater detail in Section 3.2.7 — there are certain AGN for which it remains relatively steady for a period long enough to be seen with MOJAVE's observing cadence. I identified cases where a particular epoch was associated with an EVPA which appeared as an outlier next to its contemporaries. If an epoch then had EVPAs which looked offset in many sources, I flagged it as a possible bad calibration.

As noted in Section 1.2.1, synchrotron radiation can theoretically result in fractional polarizations of up to 70 percent. For blazar jets, 10 percent is quite high. As part of the data verification process, I investigated all fractional polarizations above approximately 50 percent. All of these were either impossibly high (i.e., greater than 100 percent) or also appeared out of place next to nearby epochs. I also flagged these observations as having probable bad calibrations. In the following chapters, I describe the scientific analysis of this set of data.

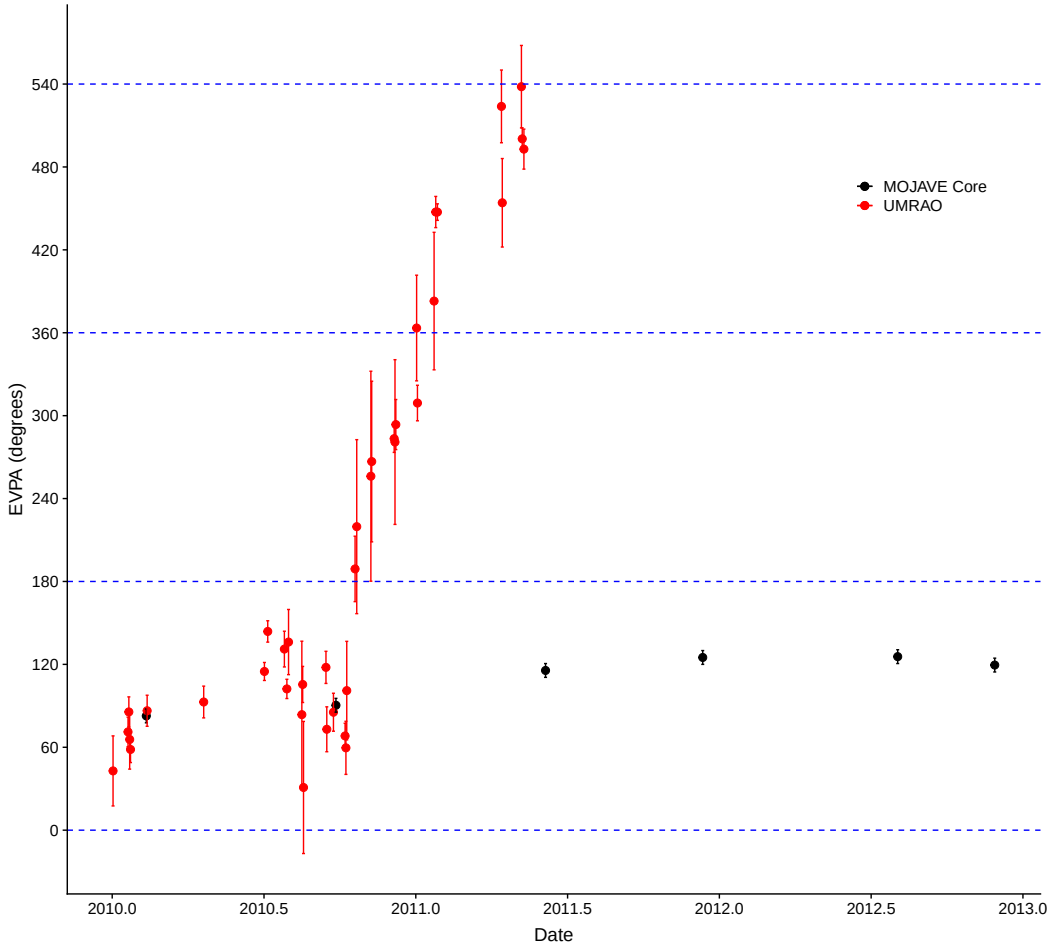

Figure 2.1. Evolution of the EVPA for 3C 446/2223-052. Data from the MOJAVE program is core-only and in black; data from the UMRAO program is red.

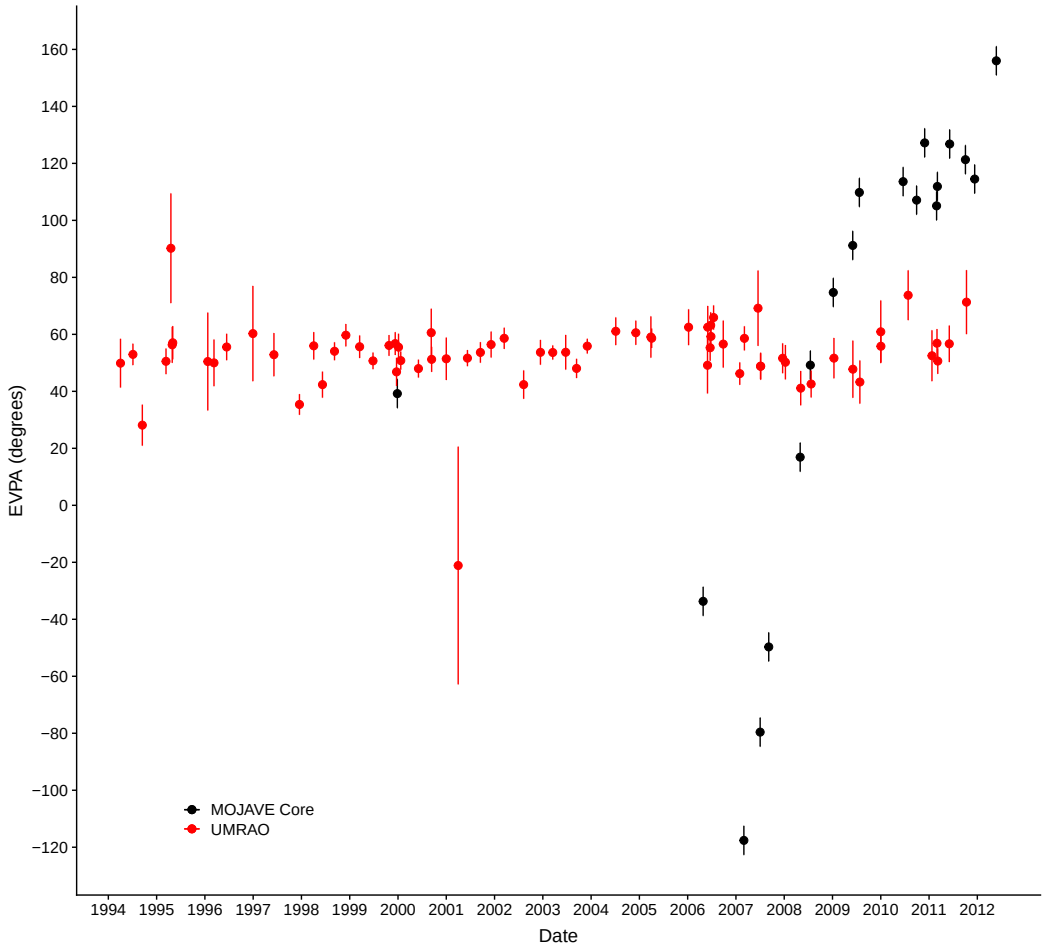

Figure 2.2. Evolution of the EVPA for AP Librae/1514-241. Data from the MOJAVE program is core-only and in black; data from the UMRAO program is red. MOJAVE EVPAs have been rotated to within 90° of the previous epoch's EVPA.

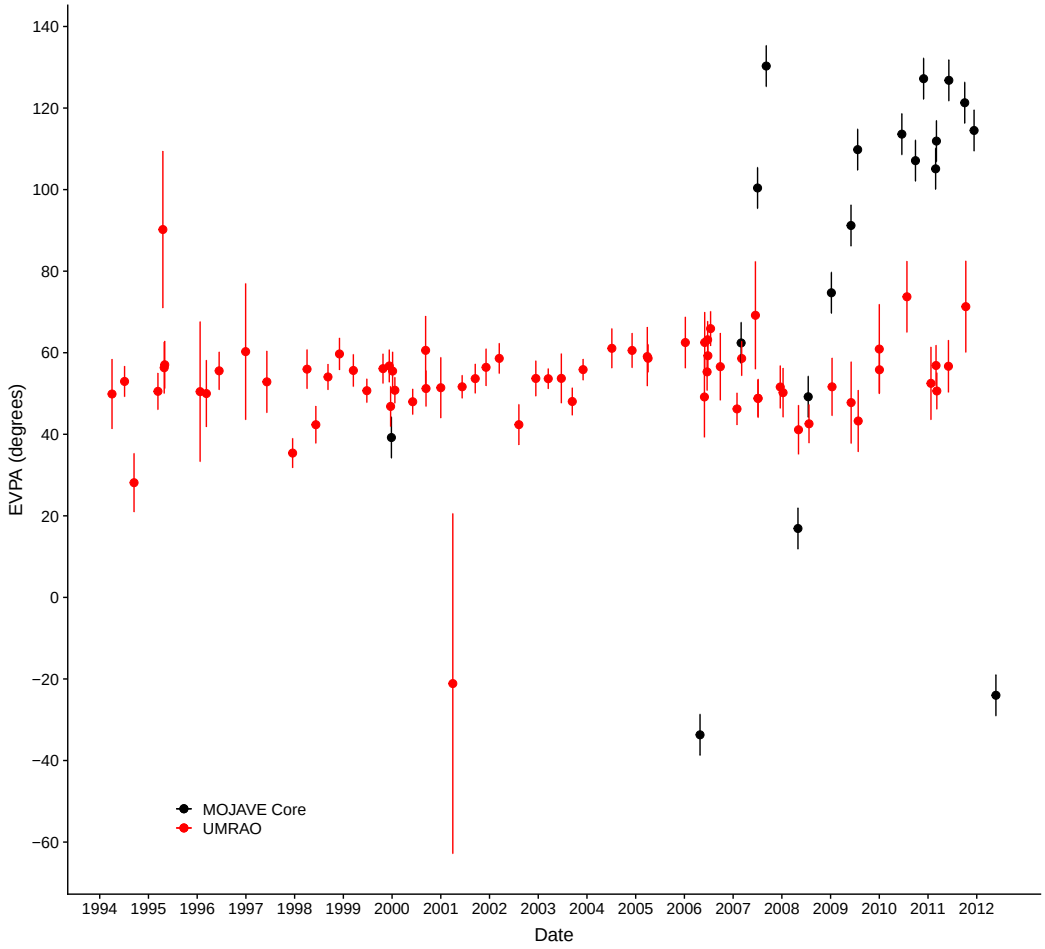

Figure 2.3. Evolution of the EVPA for AP Librae/1514-241. Data from the MOJAVE program is core-only and in black; data from the UMRAO program is red. MOJAVE EVPAs have been rotated to within 90° of the UMRAO median EVPA.

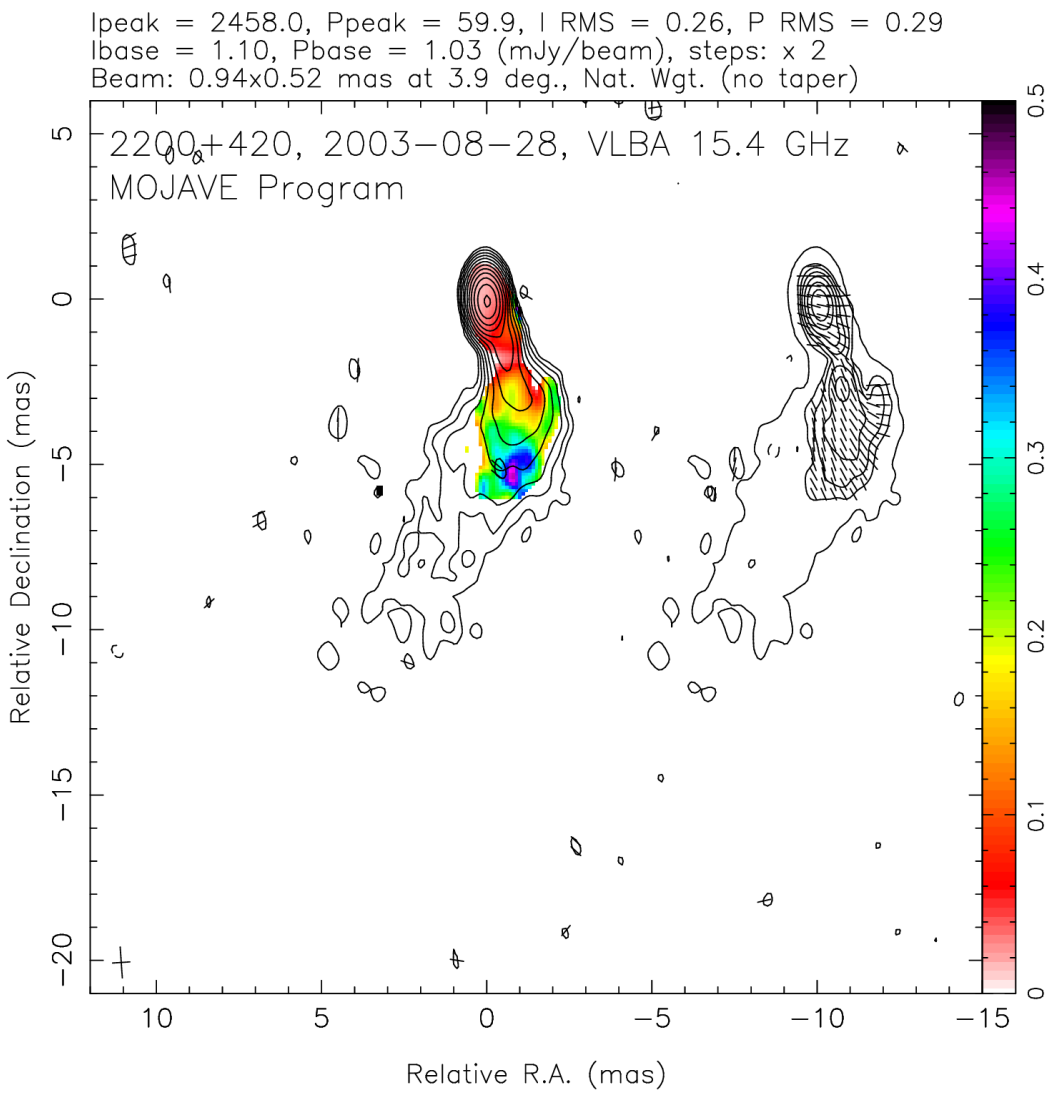

Figure 2.4. A polarized VLBA image of BL Lac taken as part of the MOJAVE program. Further description in text.

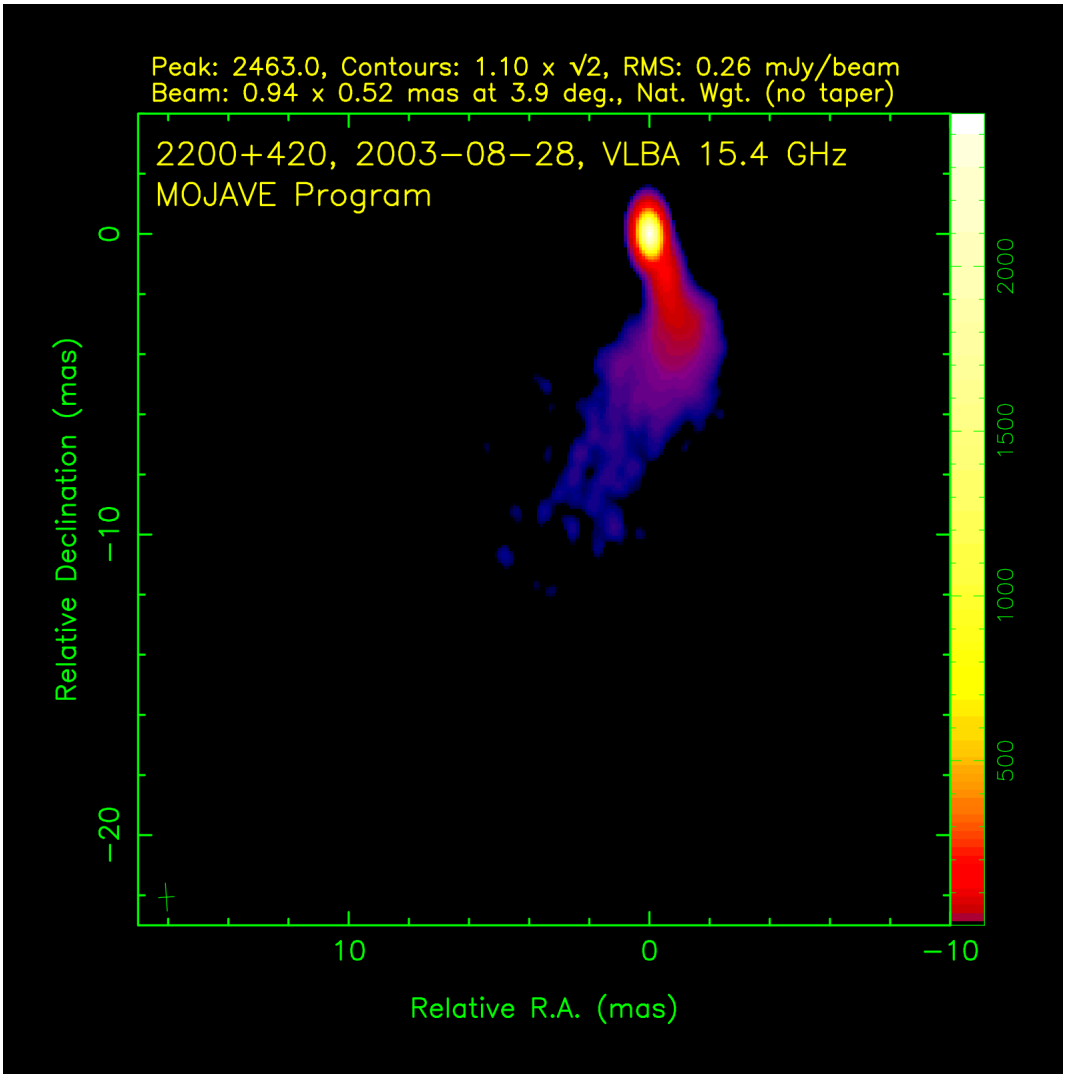

Figure 2.5. A total intensity-only VLBA image of BL Lac taken as part of the MOJAVE program. Further description in text.

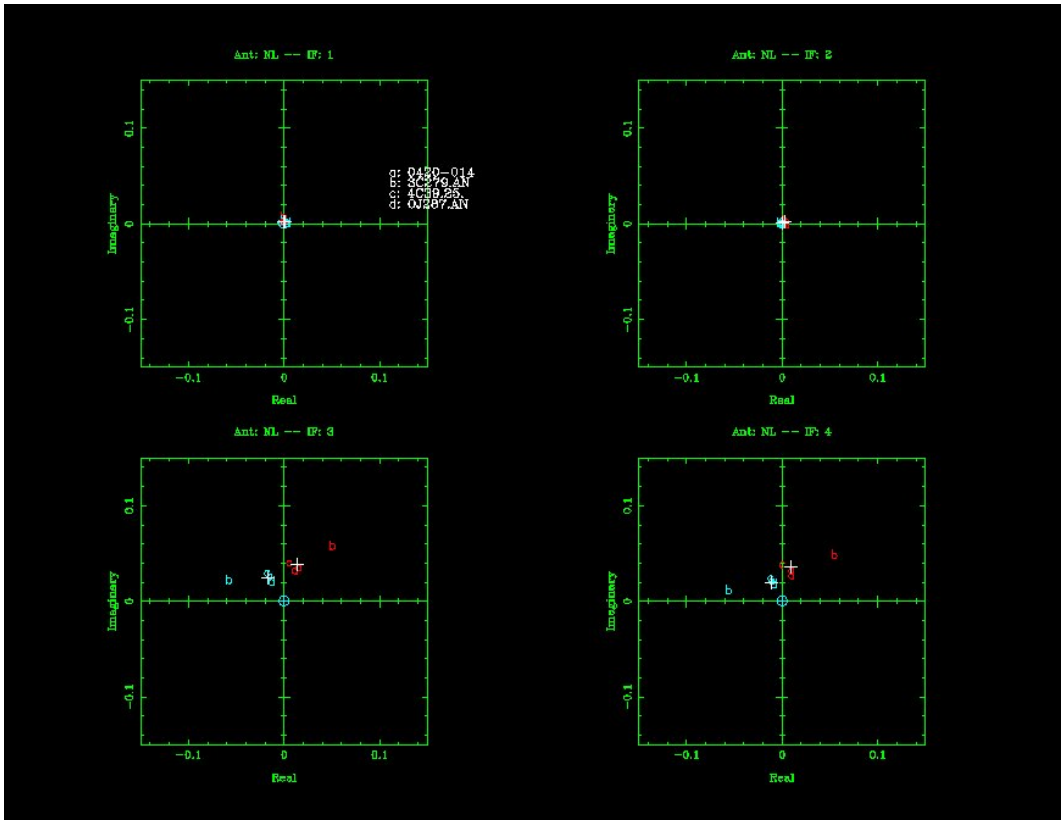

Figure 2.6. Plot of leakage terms after correction.

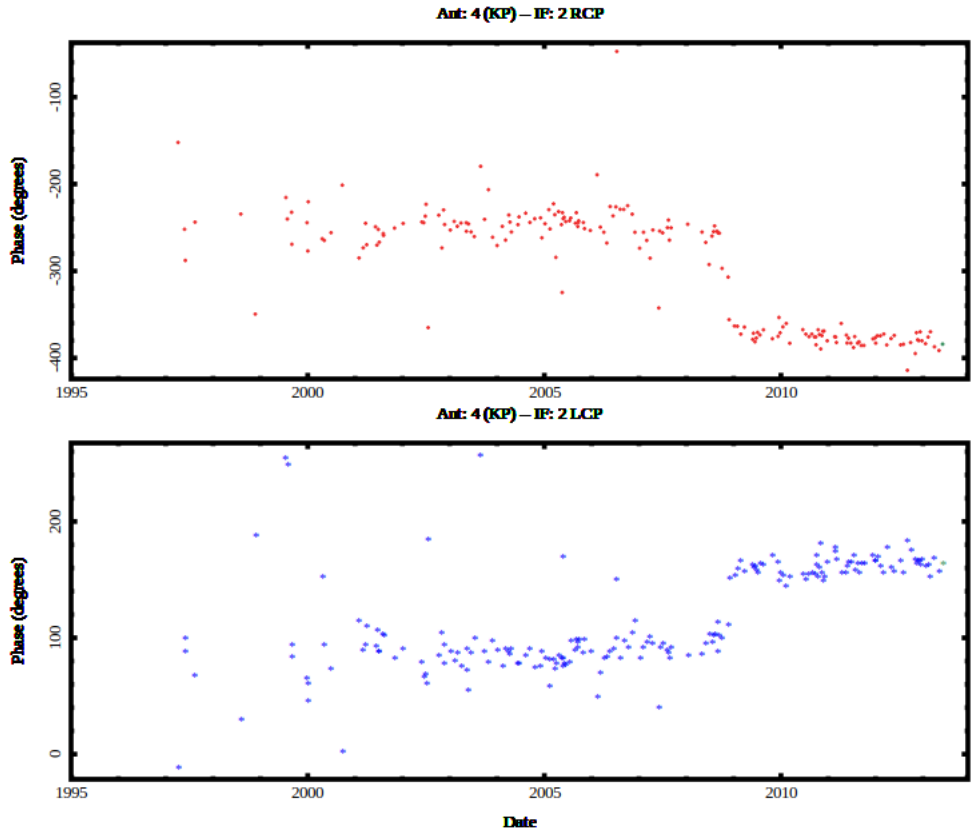

Figure 2.7. D-term phases across multiple epochs for IF 2 of the Kitt Peak VLBA antenna at 15 GHz.

3. Core Polarization

In this chapter, we present findings on the core linear polarization properties of MOJAVE AGN. In doing so, we attempt to answer the questions posed in Chapter 1 of this thesis, while updating and expanding on previous MOJAVE results. This chapter has been adapted from "MOJAVE XVI: Multiepoch Linear Polarization Properties of Parsec-Scale AGN Jet Cores" (Hodge et al., 2018), which contains the full tables 3.1 and 3.3. The adopted cosmology is $\Omega_m = 0.27$, $\Omega_\Lambda = 0.73$, and $H_0 = 71$ km s^{-1} Mpc^{-1} (Komatsu et al., 2009).

3.1 AGN Sample and Observational Data

We have analyzed the parsec-scale radio core polarization and total intensity properties of 387 AGN selected from the MOJAVE survey, which have at least five VLBA epochs at 15 GHz between 1996 January 19 and 2016 December 31. These AGN all have ≈ 100 mJy or greater of correlated VLBA flux density at 15 GHz, and are derived from several flux-density limited and representative samples. The MOJAVE 1.5 Jy sample encompasses all 181 AGN above J2000 declination $-30°$ known to have exceeded 1.5 Jy in VLBA 15 GHz flux density at any epoch between 1994.0 and 2010.0 (Lister et al., 2013b). With the launch of the *Fermi* observatory in 2008, two new γ-ray-based AGN samples were added to MOJAVE. The 1FM sample (Lister et al., 2011) consists of all 116 AGN in the 1FGL catalog (Abdo et al., 2010a) above declination $-30°$ and galactic latitude $|b| > 10°$ with average integrated *Fermi* LAT > 0.1 GeV energy flux above 3×10^{-11} erg cm^{-2} s^{-1}. In 2013, a new hard spectrum MOJAVE sample of 132 AGN was added, which had declination $> -20°$, total 15 GHz VLBA flux density > 0.1 Jy, and mean *Fermi* 2LAC catalog (Ackermann et al., 2011) or 3LAC catalog (Ackermann et al., 2015) spectral index harder than 2.1.

Of the 387 AGN presented in this analysis, 304 are members of one or more of the above samples. An additional 78 AGN are members of either the pre-cursor survey to MOJAVE (the 2cm VLBA survey; Kellermann et al. 1998), the low-luminosity MOJAVE AGN sample (Lister et al., 2013b), the 3rd EGRET γ-ray catalog (Hartman et al., 1999), the 3FGL *Fermi* LAT γ-ray catalog (Acero et al., 2015a), or the ROBOPOL optical polarization monitoring sample (Pavlidou et al., 2014). Finally, we have included five AGN that were originally candidates for the above samples, but did not meet the final selection criteria. All AGN have 15 GHz VLBI flux density greater than 100 mJy and at least five epochs of observation with polarization.

We gathered observer frame synchrotron peak frequency values from the literature (mainly Ackermann et al. 2015) where possible. For roughly half the sample, we used the ASDC SED Builder tool (Stratta et al., 2011) to determine the peak frequency from a parabolic fit to published multiwavelength data in the ($\log \nu$, $\log(\nu F_\nu)$) plane, where F_ν is the flux density at frequency ν. In the case of 24 sources, there were insufficient available data to determine a synchrotron peak frequency. We assigned a SED peak classification based on the rest frame peak values ν_p following the typical standard discussed in Section 1.1.3. For 46 BL Lacs without known redshifts and eight optically unidentified sources, we assumed a redshift of 0.3 in calculating the rest frame SED peak value. The known AGN redshifts and their literature references are listed in Table 3.1, along with optical class and SED peak classification. Table 3.2 contains a breakdown of sample AGN by optical and SED peak classification. The single epoch polarization results published in Lister and Homan 2005 were based on a flux-density limited sample of 135 AGN, of which four were ISP and the remainder were LSP. This study covers an additional 252 AGN, for a final total of 312 LSP, 30 ISP, and 21 HSP AGN, with the latter two categories consisting entirely of BL Lacs.

We reduced the polarimetric data (see Table 3.1) according to the procedures described in Lister and Homan 2005 and Lister et al. 2018. The core was in almost all cases distinguishable as the most compact feature in the radio map, located at the bright end of the jet (see Hodge et al. 2018 and Lister et al. 2016a for notes on

individual sources). We determined its position by fitting Gaussians to the (u, v) visibility data using Difmap (Shepherd, 1997). The mean I, Q, and U of the nine contiguous 0.1 mas wide image pixels centered on the core were then used to determine the core's linear fractional polarization and EVPA. The fractional polarization was considered an upper limit equal to five times the P rms noise level divided by I when P fell below the lowest contour of the relevant image presented in Lister et al. 2018. The latter were chosen at a level where the amount of spurious blank sky polarization was minimal. Approximately 12% of the available fractional polarization measurements are upper limits, and thus have an unknown corresponding EVPA. The uncertainty in fractional polarization is approximately 7% of the given values, due to uncertainties of 5% in I and P, and the EVPA is accurate within 5°, based on comparisons with near-simultaneous single-dish measurements taken at UMRAO (Aller et al. 2003). A previous MOJAVE study found that the core rotation measures are variable in time, and at 15 GHz, the median core EVPA rotation was less than 4° (Hovatta et al., 2012). For these reasons, we do not correct our measurements for Faraday rotation. Detailed description of the observational sampling is available in Lister et al. 2018.

3.2 Data Analysis and Discussion

3.2.1 Statistical Tests

The MOJAVE program observes each individual AGN with a cadence that is appropriate for its angular jet expansion speed, thus some AGN are more densely sampled in time than others. The unequal span of coverage time and frequency of sampling therefore affects some statistics; for example, any measures of maximum polarization or of flux variability are dependent on how long and how frequently the AGN has been observed, since greater time coverage creates more opportunity for the AGN to be observed in a flaring state. On the other hand, median statistics ($m_{\rm med}$, $I_{\rm med}$, and $|EVPA - PA|_{\rm med}$) are less dependent on these factors and so we calculate

them using all available epochs on the source. For all other derived quantities, we compensate for sampling biases by using only five epochs of observation spanning a standardized time length of 2.3 years. This time range represents the median total coverage time of all the AGN which had only five polarization image epochs. For each source we use the most recent period with at least five epochs of observation; when a source has more than five observations during that time range, we choose five epochs at random and use these consistently for each calculation. Of the 387 AGN in the sample, 86 do not have a period which qualifies, i.e., at least five observations within any 2.3 year period. We further omit AGN from statistical quantities where five epoch measurements are not available to be used in the calculation — for example, the EVPA statistics require five epochs with measured polarization values (not upper limits). We tabulate all the derived quantities in Table 3.3. We computed two-tailed Kolgoromov-Smirnoff (KS) tests and correlation tests with Kendall's τ coefficient using the R core package (R Core Team, 2017); for censored data comparisons we used the Peto & Peto modification of the Gehan-Wilcoxon test (Lee, 2017). "Significant" statistical test results refer to those whose chance probability is below 5%. For more information on bias correction, the mentioned tests, and the handling of censored data, see the appendix.

3.2.2 Fractional Polarization

We describe the magnitude of polarization of each AGN core with two statistical quantities: the median fractional polarization ($m_{\rm med}$) and the maximum fractional polarization ($m_{\rm max}$). In Figure 3.1, we show distributions of median fractional polarization, over all epochs of each AGN, for the most common categories of optical/SED class (50 AGN are omitted due to too many upper limit measurements to ascertain a confident median; an additional five narrow line Seyfert 1 galaxies and nine AGN of unknown optical class are not shown). The maximum fractional polarization distributions of the BL Lacs and FSRQs are shown in Figure 3.2.

The median fractional polarizations are similar to the single-epoch percentages found in Lister and Homan 2005 (Figure 3.3). The maximum fractional polarizations are higher, as would be expected based on core variability; the highest fractional polarization is almost 15%, as opposed to the 10% found previously. BL Lacs as an entire group remain more polarized than FSRQs, but that relationship does not hold across all SED peak categories.

LSP BL Lacs are the most fractionally polarized, with an average median over 3%, and are significantly different from both HSP BL Lacs (KS test result $p = 0.0097$) and FSRQs (KS test result $p = 2.7 \times 10^{-9}$). HSP BL Lacs and FSRQs are similar, however, and each of their median fractional polarization distributions has a mean below $\sim$2%. The median fractional polarization of BL Lacs is strongly anti-correlated ($p = 9.1 \times 10^{-5}$, correlation coefficient τ =-0.26) with synchrotron SED peak frequency (shown in Figure 3.7; other optical classes are shown in Figure 3.8, although there is no apparent relation). This trend for BL Lacs was previously reported by Lister et al. 2011 and Linford et al. 2012b, of which the former theorized that AGN with lower synchrotron peaks may be more Doppler boosted than their high synchrotron peaked counterparts, resulting in higher core polarization. This was partially based on the low core brightness temperatures of HSP BL Lacs, a relationship which still holds true (Homan, D. C. et al., in preparation).

An alternate explanation proposed by Angelakis et al. 2016 is based on a shock-in-jet model. In this scenario, the volume immediately downstream of the shock is the origin of emission near the synchrotron SED peak frequency and above. If the shock orders an underlying magnetic field, then higher polarization might be expected closer to these frequencies. While Angelakis et al. 2016 use this theory to describe the same anti-correlation in optical polarization, at 15 GHz we are also probing closer to the peak frequency of LSP BL Lacs than HSP BL Lacs, which could explain the lower polarization of the latter.

In Lister et al. 2011 beam depolarization effects were given as a possible reason for the difference between LSP BL Lac and FSRQs, as the former have much lower

redshifts on average. In our sample, there is a cohort of seven high-redshift FSRQs with fractional polarization which is lower than average, but no trend between redshift and fractional polarization exists below $z = 2.5$. The highest redshift FSRQs alone cannot therefore be responsible for the relatively low polarization of the class. In Lister and Homan 2005 and Aller et al. 1999, the (mostly LSP) BL Lacs also had greater core polarization than FSRQs; these authors suggested the cause was slower flow speeds in BL Lacs. Slower flows could create stronger transverse shocks compared to oblique ones in FSRQs, leading to a more ordered magnetic field and better alignment between the EVPA and the local jet direction.

We note that $m_{\rm med}$ is unavailable for all of the 17 radio galaxies in our sample, of which all but III Zw 2 have at least half their core m measurements classified as upper limits. This suggests that their polarization as a class is low. In contrast, $m_{\rm med}$ is available for $\sim$60% of HSP BL Lacs despite the fact that their I is typically lower than that of the radio galaxies, i.e., the upper limits are not caused by low general intensity. The low polarization in radio galaxies is likely due to higher angles to the line of sight, resulting in relativistic aberration as described in Wardle 2013 and Section 1.1.2.

3.2.3 EVPA Alignment with the Inner Jet

In order to investigate possible alignments between the core EVPA direction and each jet, we determined an inner jet position angle (jet PA, in degrees from north towards east relative to the core) at each epoch using the VLBA data. For the majority of AGN, we used the method described in Lister et al. 2013b, which takes a flux-weighted position angle average of the components near the core generated by the CLEAN imaging algorithm (Högbom, 1974). This method fails in cases where there is an emission gap between the core and downstream features; in the case of all epochs of 39 AGN we therefore used the position angle of the closest downstream Gaussian-fitted jet feature, as was done in Lister and Homan 2005. In some individual epoch

images, it was impossible to determine a jet PA due to a complete lack of apparent downstream jet emission. These are indicated in Table 3 of Hodge et al. 2018.

For the epochs described in Section 3.2.1, we rotated the EVPA to within 90° of the jet PA (by adding or subtracting 180°), subtracted it from the PA, and took the absolute value of this angle difference to get an EVPA offset value. The distribution of median offsets for each AGN class are shown in Figure 3.4. The EVPAs of BL Lacs are more often aligned with the local jet direction (i.e., low offset values), in contrast to FSRQs. A KS test between the LSP BL Lac and FSRQ offset distributions returns a p-value of 1.69×10^{-5} that they derive from the same parent population. None of the BL Lac subclass distributions are significantly different from each other. These findings on the difference in alignment between FSRQs and BL Lacs in general agree with the single-epoch results presented in Lister and Homan 2005 (see Figure 3.5), which contained mainly LSP AGN. Beyond the aforementioned shocks, another suggested scenario is that both types of jets possess a helical magnetic field; the slower flow speeds of BL Lacs could lead to a different pitch angle such that they have a stronger toroidal component to their magnetic field, leading to better EVPA-jet alignment compared to FSRQs (Gabuzda et al., 2000; Asada et al., 2002). It should be mentioned, though, that various other VLBI studies of radio core EVPA/PA alignment in AGN jets have reported contradictory findings on whether alignment, anti-alignment, or both cases are expected (see Agudo et al. 2018 and references therein).

Of the studies suggesting an anti-alignment between core EVPAs and the jet direction (e.g., Helmboldt et al. 2007), some at 5 GHz have found that only FSRQs, not BL Lacs, prefer an EVPA-jet PA offset of near 90° (Pollack et al., 2003; Aller et al., 2003). Our data show no apparent clustering at 90°, but the FSRQ distribution is skewed towards misalignment (median $|EVPA - PA|_{\rm med}$=48°). Figure 3.6 shows that the most fractionally polarized AGN cores, mainly LSP BL Lacs, tend to have EVPAs closely aligned with the local jet direction — a trend which persists if each optical class is inspected individually ($p = 5.3 \times 10^{-13}$, τ =-0.27). This supports a

scenario where the magnetic field is more ordered when transverse to the jet. We further discuss the EVPA/PA and their time evolution in Section 3.2.6.

3.2.4 Fractional Polarization Variability

Because of the stochastic nature of AGN light curves, there has been no clear consensus on what constitutes an ideal statistical measure of flux or fractional polarization variability over time, as discussed by Richards et al. 2014. Many commonly-used statistics depend on frequent and/or regular observations of all sources, and are therefore not well-suited to the MOJAVE data. We use the variability index of Aller et al. 1999, and later adopted by Jorstad et al. 2007, defined by:

$$m_{\rm var} = \frac{(m_{\rm max} - \sigma_{\rm max}) - (m_{\rm min} + \sigma_{\rm min})}{(m_{\rm max} - \sigma_{\rm max}) + (m_{\rm min} + \sigma_{\rm min})}. \tag{3.1}$$

The error for a particular epoch, σ, is approximately 7%, based on the definition of fractional polarization and the 5% errors in P and I as described in Lister et al. 2018. As discussed by Aller et al. 2003 and in Appendix A, this measure is not accurate when the minimum values fall below the signal to noise threshold. We therefore omit any AGN where one or more of the five fractional polarization measurements discussed in Section 3.2.1 is an upper limit. We also throw out any cases where the errors are high enough to result in a negative variability index.

The variability of fractional polarization (Figure 3.9) is not significantly dependent on synchrotron peak frequency, although we note that FSRQs appear more variable than HSP BL Lacs (KS test result $p = 0.005$). Studies of fractional polarization variability tend to be rare, although Jorstad et al. 2007 found FSRQs cores to be more variable than (mostly LSP) BL Lacs in a small sample of 15 AGN at 43 GHz. The AGN cores with the smallest fractional polarization variability are more likely to have small EVPA-jet misalignments (Figure 3.10; $p = 0.009$, $\tau = 0.11$).

3.2.5 Total Intensity Variability

We also use Equation 3.1, replacing m with Stokes I, to derive the variability index $I_{\rm var}$ for the total intensity. Figure 3.11 shows the $I_{\rm var}$ distributions for FSRQs and BL Lac subclasses. Interestingly, while HSP and LSP BL Lacs have similar distributions, ISP BL Lacs peak at a higher variability index — they are significantly different from HSP BL Lacs ($p = 0.009$) and nearly so for LSP BL Lacs ($p = 0.06$). With the exception of ISP BL Lacs, FSRQs are the most variable blazar class. Tests for a similar parent distribution produced results of $p = 0.03$ for FSRQs vs. LSP BL Lacs and $p = 0.002$ for FSRQs vs. HSP BL Lacs. Past radio studies of total intensity variability have shown somewhat mixed results; Aller et al. 2003 also found no significant differences between FSRQs and BL Lacs in their single dish, 5-15 GHz UMRAO study spanning 1984-2001. Richards et al. 2014 tested two samples, observed with the OVRO 40m telescope at 15 GHz from 2008-2011, and found the same for their γ-ray selected AGN, but that BL Lacs were significantly more variable in their radio-selected sample.

Due to the association between Doppler factor and variability (Tingay et al., 2001), in a scenario where a lower synchrotron peak frequency corresponds with higher Doppler beaming, LSP BL Lacs would be expected to have the highest level of variability among the subclasses. Richards et al. 2014 also reported a group of highly variable ISP BL Lacs, but additionally found that LSP BL Lacs were significantly more variable than HSP BL Lacs.

Total intensity variability appears to be anti-correlated with fractional polarization in our sample, with a notable deficit of highly variable cores with high fractional polarization (Figure 3.12). We performed a Kendall τ non-parametric test of correlation, which yielded a $p = 0.04$ probability for no correlation ($\tau = -0.09$). This trend disappears if the BL Lac and FSRQ populations are tested separately, making it likely that the anti-correlation is simply due to the presence of low variability, highly polarized LSP BL Lacs. Values for $I_{\rm var}$ are generally lower than those of $m_{\rm var}$,

indicating that the fractional polarization undergoes greater percentage change during the same time period. The two variability indices are correlated, with a τ test yielding $p = 0.003$, $\tau = 0.13$ for no correlation (see Figure 3.13). There is a lack of AGN cores which are variable in total intensity while remaining stable in fractional polarization. On the other hand, the fractional polarization can be highly variable even in cases where the total intensity shows little variability.

3.2.6 EVPA Variability

The characterization of EVPA variability is not straightforward due to the 180° ambiguity in the measurements, and requires a special procedure. We begin by adding or subtracting 180° from all the EVPA measurements for a particular AGN such that they lie within the range of 0°–180°. We then add a +180°-shifted copy of each of these values, creating a total range of 0°–360°. We bin this set of data using sequentially larger bins until at least one bin contains half the data. The midpoint of that bin is established as the mode of the EVPAs, and we then rotate the original (un-copied) set of EVPAs by the same amount (multiples of 180°) so that they lie within ±90° of this mode. Our $EVPA_{\rm var}$ statistic is defined as the standard deviation of these angles. In Figures 3.14 and 3.15, we show examples of cores with low and high EVPA variability, respectively.

We plot the distributions of this statistic in Figure 3.16. Examining them by optical class, the FSRQ variabilities follow an approximate normal distribution, but BL Lacs are skewed towards lower variability (KS test p-value of 0.0005 between FSRQs and LSP BL Lacs). In the optical, Angelakis et al. 2016 reported an anti-correlation between synchrotron peak frequency and EVPA variability for a sample of 79 AGN; the mean of our BL Lac distributions become progressively lower with increasing synchrotron peak, but none of the subpopulations are significantly different, and a statistical test between synchrotron peak frequency and EVPA variability showed no

significant correlation ($p = 0.3$). We found no discernible cause for the divide into low variability and high variability groups for LSP BL Lacs in Figure 3.16.

As was the case with the median EVPA-jet PA alignment, the EVPA variability is also anti-correlated with fractional polarization (Figure 3.17, $p = 1.9 \times 10^{-13}$, τ =-0.32) and positively correlated with fractional polarization variability (Figure 3.18, $p = 4.1 \times 10^{-7}$, $\tau = 0.22$), i.e., AGN with preferred EVPA directions have greater fractional polarization which is more stable over time. These results are consistent with a strong, standing transverse shock at the base of the jet. When evidence for standings shocks is observed, they frequently appear to be near the cores of blazars in VLBI images (Jorstad et al., 2017; Lister et al., 2013b). It is possible that others may exist closer to the base of the jet, but are unseen due to the finite angular resolution of the VLBA at 15 GHz ($\simeq$0.5 mas) (Gómez et al., 2016).

There are highly variable jets of moderate misalignment, but few jets which are highly aligned or misaligned and simultaneously highly variable (Figure 3.19). While the scenario above explains a preference for stability in aligned jets, the lack of misaligned and unstable jets is interesting. This grouping is not due to the algorithms used to calculate either variable, as it disappears if the data are replaced with random numbers. Without greater numbers, it is difficult to determine whether this trend is significant or coincidental, however.

Our measure of EVPA variability does not include any information about the rotation of the EVPA with respect to the local jet direction. The jet PAs of MOJAVE AGN typically do not vary on the level of the core EVPAs, but there are some individual exceptions where systematic changes of up to a few degrees per year are seen (Agudo et al., 2007; Lister et al., 2013b). To address whether EVPA rotations coincide with rotations of the jet PA, we first subtracted the jet PA from the EVPA; essentially, taking all angles relative to the PA at each epoch rather than from the north direction on the sky. We then followed the method described for $EVPA_{\rm var}$ to obtain $(EVPA - PA)_{\rm var}$. We plot the empirical cumulative distribution functions (CDFs) of $(EVPA - PA)_{\rm var}$ and $EVPA_{\rm var}$ for the main optical classes in Figure 3.20.

For each of these classes, the CDF of $(EVPA-PA)_{\rm var}$ is similar to that of $EVPA_{\rm var}$, and the separation between classes is preserved, e.g. FSRQs are more variable than BL Lacs. As expected, taking into account the jet PA variations only slightly changes the overall EVPA variability statistics.

3.2.7 EVPA Stability

We find that many of the EVPAs are fairly stable — 24% of the AGN with available values have an $EVPA_{\rm var}$ of less than 10°. In contrast, Aller et al. 2003 found "long-term stability" in only seven of their 62 sources at 14.5 GHz, potentially due to greater influence from features near the core which are not resolvable by a single dish telescope (Aller et al., 1999). We have further investigated the possibility of AGN with stable EVPAs by also computing $EVPA_{\rm var}$ based on all epochs, rather than the relatively unbiased five epochs used in Section 3.2.6 and the majority of this chapter. We constrain this calculation to AGN with at least 10 measurements of EVPA; of the 171 AGN which meet this criterion, only 10 (listed in Table 3.4) have an $EVPA_{\rm var}$ of less than 10°. Of these 10 AGN, eight have an EVPA mode value within 20° of the mean jet PA. This relationship agrees with the trends regarding EVPA-jet PA alignment and EVPA variability reported in the previous section. In Figure 3.21, we show the histogram of EVPAs for OX 161, which is the least variable with an $EVPA_{\rm var}$ of 4.7°. For all AGN with at least 10 measurements of EVPA, the median coverage time — from first epoch with EVPA to last epoch with EVPA — is 10.7 years. The percentage of AGN with stable EVPAs ($EVPA_{\rm var}$ under 10°) is 6%. This is a large decrease from the 24% result calculated from 2.3 year periods, and is more consistent with the findings of Aller et al. 2003, which were based on ∼15 years of monitoring data. It is well-known that AGN are variable on long-term timescales in addition to their short-term variability (Hovatta et al., 2007); the results presented here stress that long-term monitoring is essential to understanding the EVPA as well.

Although we use a standard deviation to describe the level of EVPA variability, it should be noted that the general shape of AGN EVPA distributions is unknown. Aller et al. 2003 found some sources to change between two preferred EVPAs, suggesting a bimodal distribution. We investigated graphs of the EVPAs similar to Figure 3.21 for all AGN and found that two high peaks in a graph was rare; when they did occur, they could conceivably be a result of sampling from a normal distribution. The intrinsic behavior will be easier to discern as MOJAVE progresses and new observations are made.

3.2.8 Correlations with Luminosity

We have calculated the median core luminosity of each AGN with known redshift, assuming a flat spectral index, as:

$$L_{\rm med} = \frac{4\pi d_{\rm L}^2 I_{\rm med}}{(1+z)}, \tag{3.2}$$

where $d_{\rm L}$ is the luminosity distance and $I_{\rm med}$ is the median core intensity. The latter is approximately equal to the core flux density, since the cores are typically unresolved. In Figure 3.22, we plot the median luminosity versus the median fractional polarization for all available cores. The lowest core luminosities are associated with low core fractional polarization, and consist primarily of HSP BL Lacs. Given that the highly compact core emission is most likely Doppler boosted, this lends further support to the scenario described in Lister et al. 2011, in which HSP BL Lacs are less beamed and also less polarized due to lower Doppler factors; this trend would also be expected based on the model of Angelakis et al. 2016. However, we find no relationship between our EVPA-based statistics and the median luminosity, which suggests that the low polarization is unrelated to inherent magnetic field properties.

3.2.9 Narrow Line Seyfert 1s

Five of the AGN in our sample are classified as narrow line Seyfert 1 galaxies (NLSy1). All of them have a relatively low median fractional polarization, with the highest reaching only 1.14%. They also have EVPAs misaligned with the jet PA, with $|EVPA - PA|_{\rm med}$ ranging from 44° to 80°. For four of these five, we were able to calculate the variability in total intensity. These values are also relatively low compared to blazars, with the highest $I_{\rm var}$ equal to 0.26 (the mean FSRQ value is 0.24). Due to the number of measurements qualified as upper limits, the fractional polarization variability and EVPA variability could only be determined for two of the NLSy1s.

3.2.10 Correlations with γ-ray Emission

In this section, we parallel the analysis of Sections 3.2.2 through 3.2.6 with a basis on AGN detection status by *Fermi's* Large Area Telescope (LAT). Because of the lower energy cutoff of the LAT instrument, it more readily detects AGN with higher synchrotron peak frequencies. Conversely, AGN selected on the basis of bright radio emission prefer lower peaked sources, representing a separate population (Lister et al., 2011). The *Fermi*-LAT AGN catalog is almost entirely dominated by blazars, which suggests that the brightest γ-ray AGN have high Doppler beaming factors (Acero et al., 2015b). Therefore, an AGN sample selected on the basis of low-frequency radio emission (e.g., the 3CR survey Bennett 1962), in which lobe-dominant objects are common, will have fewer LAT detections since it is non-orientation biased. In order to limit our analysis to radio-selected blazars, we only examine the LAT detection statistics of AGN included in the MOJAVE 1.5 Jy VLBA flux-density limited sample, and exclude the radio galaxies, NLSy1s, and optically unidentified sources. We also exclude the galactic plane region ($|b| > 10°$) due to the greater difficulties of identifying reliable *Fermi* associations (Acero et al., 2015b). We ultimately consider 155 AGN with optical class as follows: 97 FSRQs and 24 BL Lacs associated with a LAT

detection; and 33 FSRQs and 1 BL Lac with no *Fermi* third source catalog (Acero et al., 2015b) association.

We begin by revisiting the conclusions of Hovatta et al. 2010, an early study which investigated γ-ray connections with radio polarization using a similar subset of the original 1.5 Jy Sample (a total of 123 AGN) and the *Fermi* LAT Bright Source List (0FGL; Abdo et al. 2009). In Hovatta et al. 2010, 0FGL AGN (those detected in the first three months of the *Fermi* mission) were found to have greater polarized flux than non-0FGL AGN during the year post-*Fermi* launch. The median fractional polarization of 0FGL AGN was also higher than non-0FGL AGN in the same year, but no difference was found between medians calculated from the six years pre-launch. We have similarly divided our observations into pre- and post-launch periods (before and after August 2008) and calculated the median fractional polarization for each AGN separately within the time frames. We plot the results in Figure 3.23. In contrast to Hovatta et al. 2010, we do not find LAT-detected AGN to have a higher median fractional polarization during the LAT observing era. We also find no significant differences between the LAT-detected and non-LAT-detected AGN in either era.

However, non-LAT-detected AGN more often lack a measurable median fractional polarization due to higher numbers of upper limit measurements — 12% of non-LAT-detected AGN have unknown $m_{\rm med}$ in the pre-LAT era, and 20% in the post-LAT era. By comparison, 4% and 3% of LAT-detected AGN have unknown $m_{\rm med}$ in the pre- and post-LAT eras, respectively. This agrees with the VLBA 5 GHz findings of Linford et al. 2012a, which claimed non-LAT-detected AGN were more often unpolarized, but when their measurements were polarized enough to be qualified as detections, they had comparable fractional polarization to LAT-detected AGN. We investigated further by dispensing with the use of $m_{\rm med}$ and directly comparing the fractional polarization values, including censored points, of the five epochs per AGN described in Section 3.2.1. This was done without dividing the data into pre- and post-LAT eras. Our statistical test did not reveal significant differences ($p = 0.15$). In Section 3.2.2, we discussed differing fractional polarizations among optical classes, and the LAT-

detected set of AGN has a far greater ratio of BL Lacs to FSRQs. We note that the significance of the preceding results, or lack thereof, does not change when the analysis is limited to only FSRQs.

Previous research has suggested that LAT-detected AGN are more variable in both total intensity (Richards et al., 2014) and fractional polarization (Hovatta et al., 2010). In our sample, both LAT-detected variability distributions have greater means, but we cannot confirm significant differences (KS test $p = 0.13$ for total intensity variability and $p = 0.13$ for fractional polarization variability as well). While we find no difference in median EVPA-jet PA offset based on LAT detection status, we do find a significant difference in EVPA variability. In Figure 3.24, we show that non-LAT-detected AGN are skewed toward low values of $EVPA_{\rm var}$, and a KS test results in a p-value of 0.005 for the same parent distribution ($p = 0.008$ if only FSRQs are compared).

Higher EVPA variability in LAT-detected AGN could be explained by a connection between γ-ray flaring and EVPA rotation. Optical EVPA rotation events have only been observed in γ-ray-loud AGN (Blinov et al., 2018). The relationship between radio EVPA events and γ-ray flaring is less certain; Jorstad et al. 2001 found a statistical link between periods of high γ-ray activity and the ejection of radio knots, partially through analysis of the radio polarization. Additionally, the radio polarization behavior of multiple AGN have been modeled at the time of γ-ray flares with data from the UMRAO (Aller et al., 2014, 2016). These shock-based models, however, also predict increases in fractional polarization and radio flux density during γ-ray flares. Greater variability in fractional polarization and total intensity might then be expected for LAT-detected AGN, which is not seen to a significant degree in our data.

3.3 Summary

We have investigated the linear polarization properties of a sample of 387 parsec-scale AGN jet cores, using 15 GHz VLBA data. In the first paper in the MOJAVE series, it was found that BL Lacs in general are more polarized than FSRQs and have EVPAs which are better aligned with the local jet direction (Lister and Homan, 2005). We have confirmed these findings and expanded on them with a larger AGN sample representing a broader range of synchrotron peak frequencies. With new multi-epoch measurements, we have also explored a variety of statistics related to AGN variability. Our conclusions are as follows:

1. Although HSP BL Lacs and FSRQs have similar median fractional polarization, LSP BL Lacs are significantly more polarized. Radio galaxies have too many censored data points for calculation of a median, which suggests that they have relatively low fractional polarization.

2. BL Lacs have EVPAs that tend towards alignment with the jet PA, while FSRQs are skewed towards misalignment. BL Lac populations have similar median EVPA-jet PA alignment regardless of synchrotron peak. The most polarized cores have EVPAs almost parallel with the jet PA.

3. HSP BL Lacs are less variable in fractional polarization than FSRQs, but we find no significant differences among other optical/SED peak classes. The least variable AGN cores tend to have EVPAs aligned with the local jet direction.

4. ISP BL Lacs appear the most variable in total intensity; the HSP and LSP BL Lac distributions are similar, and both less variable than FSRQs. Fractional polarization is more variable than total intensity, and the two variabilities are positively correlated.

5. The EVPAs of BL Lacs are less variable than the EVPAs of FSRQs, and they do not appear dependent on synchrotron peak frequency. AGN cores with low EVPA variability are more likely to have high fractional polarization and low

variability in fractional polarization. Our results show little change when the jet PA is subtracted from the EVPA before calculation of the variability; in other words, the angle difference between the jet PA and EVPA is similar in variability to the EVPA alone.

6. Of the five NLSy1s in our sample, all have low fractional polarization compared to blazars. Additionally, their EVPAs are not aligned with the jet PA.

7. AGN detected at γ-ray energies by *Fermi*-LAT are not significantly more fractionally polarized than non-detected AGN. However, their EVPAs are significantly more variable.

Overall, we believe these results are indicative of inherent differences between BL Lacs and FSRQs, perhaps in shock strength and geometry; by contrast, differences in polarization based on synchrotron peak and γ-ray detection can generally be explained by Doppler boosting. The latter explanation will be investigated further in Chapter 4.

Table 3.1. General Properties of the AGN Sample

Source	Alias	1.5 Jy	LAT	Optical Class	$\log(\nu_{\rm peak})$ (Hz)	Redshift	Ref.
(1)	(2)	(3)	(4)	(5)	(6)	(7)	(8)
0003+380	S4 0003+38	N	Y	Q	13.2	0.229	Schramm et al. (1994)
0003−066	NRAO 005	Y	N	B	13.1	0.3467	Jones et al. (2005)
0006+061	TXS 0006+061	N	Y	B	13.8	1.56263	Albareti et al. (2017)
0007+106	III Zw 2	Y	N	G	13.3	0.0893	Sargent (1970)
0010+405	4C +40.01	N	N	Q	13.0	0.256	Thompson et al. (1992)
0011+189	RGB J0013+191	N	Y	B	13.9	0.477	Shaw et al. (2013)
0015−054	PMN J0017−0512	N	Y	Q	13.7	0.226	Shaw et al. (2012)
0016+731	S5 0016+73	Y	N	Q	12.7	1.781	Lawrence et al. (1986)

Note. — Columns are as follows: (1) B1950 name, (2) other name, (3) MOJAVE 1.5 Jy catalog inclusion, (4) status of Fermi-LAT detection, (5) optical classification where Q = FSRQ, B = BL Lac, G = radio galaxy, N = narrow line Seyfert 1, and U = unidentified, (6) rest frame log synchrotron peak frequency in Hz (for sources with no known redshift, z=0.3 was used), (7) redshift, (8) reference for redshift (or optical class, for BL Lacs without known redshift).

[1]Located within 10 degrees of the galactic plane; omitted from γ-ray comparisons.

Table 3.2. Optical and Synchrotron Peak Classifications

Optical Class	LSP	ISP	HSP	Unknown	Total
FSRQ	223	0	0	16	239
BL Lac	64	30	21	3	118
Radio Galaxy	14	0	0	3	17
NLSy1	5	0	0	0	5
Unidentified	6	0	0	2	8
Total	312	30	21	24	387

Table 3.3. Derived Core Quantities

Source	$m_{\rm med}$ (%)	$m_{\rm max}$ (%)	$m_{\rm var}$	$I_{\rm med}$ (Jy beam^{-1})	$I_{\rm var}$	$EVPA_{\rm var}$ (deg)	$(EVPA-PA)_{\rm var}$ (deg)	$\lvert EVPA-PA\rvert_{\rm med}$ (deg)
(1)	(2)	(3)	(4)	(5)	(6)	(7)	(8)	(9)
0003+380	0.8	0.9	···	0.42	0.22	···	···	19
0003−066	5.0	9.0	0.06	0.75	0.08	8	10	10
0006+061	2.1	4.5	0.49	0.13	0.10	5	4	17
0007+106	···	···	···	0.67	···	···	···	66
0010+405	···	0.3	···	0.47	0.11	···	···	24
0011+189	3.6	4.6	0.09	0.10	0.05	10	9	15
0015−054	1.6	2.1	0.21	0.20	0.43	44	38	43
0016+731	1.8	···	···	1.21	···	···	···	30
0019+058	0.8	3.0	0.90	0.25	0.08	30	32	48
0027+056	2.1	2.7	0.30	0.44	0.10	8	8	53

Note. — Columns are as follows: (1) B1950 name, (2) median fractional polarization in %, (3) maximum fractional polarization in %, (4) fractional polarization variability, (5) median total (Stokes I) intensity in Jy/beam, (6) total intensity variability, (7) EVPA variability in degrees, (8) EVPA variability computed relative to jet PA in degrees, (9) median absolute difference between EVPA and jet PA in degrees.

Table 3.4. AGN with Stable Core EVPAs

Alias	Number of Epochs	Coverage Time (years)	Optical/SED Class	$EVPA_{\rm var}$ (deg)	EVPA Mode (deg)	Mean PA (deg)
(1)	(2)	(3)	(4)	(5)	(6)	(7)
NRAO 005	18	9.7	LSP B	8.5	18.5	2
GB6 J0929+5013	11	5.1	ISP B	8.3	103.0	111
B2 1040+24A	10	4.5	Q	8.5	96.0	87
OP 112	11	16.9	LSP B	6.4	35.0	40
OQ 240	11	7.1	HSP B	8.1	143.0	141
4C +14.60	11	14.6	LSP B	6.9	325.5	324
4C +56.27	26	14.6	LSP B	9.4	208.5	200
OV 591	11	6.1	Q	9.7	36.5	117
4C −02.81	16	15.3	Q	5.9	90.5	101
OX 161	10	7.8	Q	4.7	307.0	269

Note. — Columns are as follows: (1) AGN name, (2) number of EVPA epochs used to calculate $EVPA_{\rm var}$, (3) years between first and last EVPA epoch, (4) optical/SED peak classification where Q = FSRQ and B = BL Lac (all FSRQs are low-synchrotron-peaked), (5) EVPA variability in degrees calculated with all available EVPA epochs, (6) EVPA mode in degrees rotated to within 180° of the mean jet PA, (7) circular mean of the jet PA calculated with all available epochs.

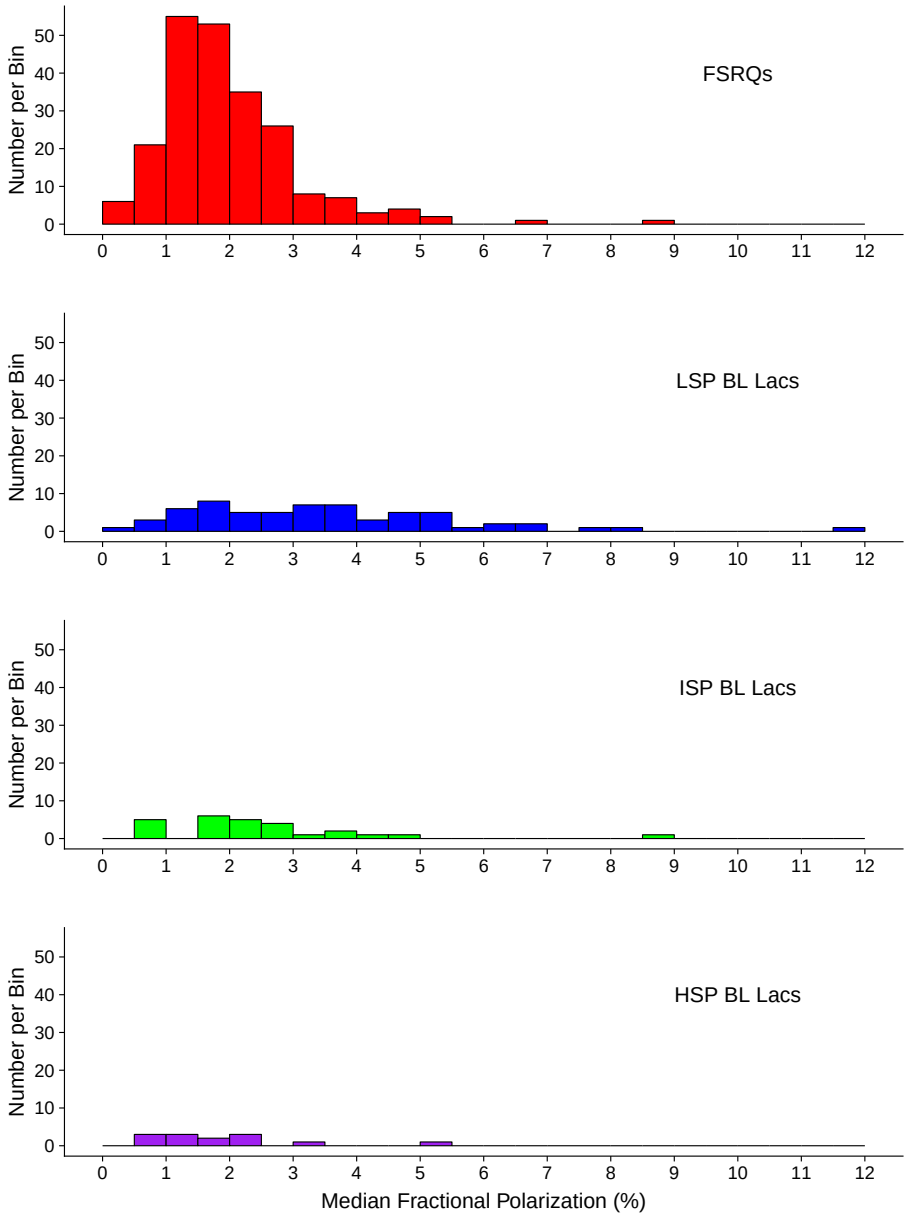

Figure 3.1. Distributions of median fractional polarization $m_{\rm med}$, grouped by optical/synchrotron peak classification.

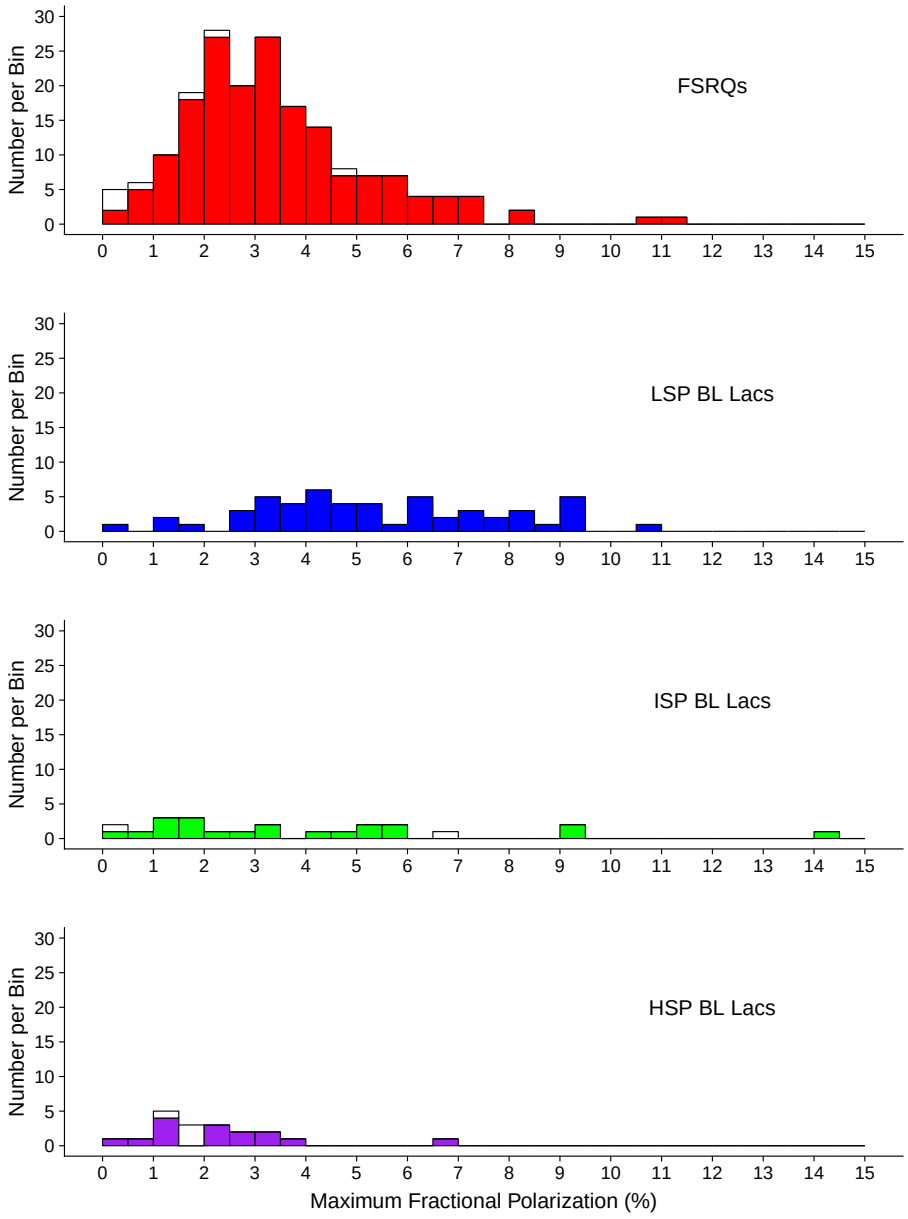

Figure 3.2. Distributions of maximum fractional polarization $m_{\max}$, grouped by optical/synchrotron peak classification. Unfilled bins represent upper limit measurements.

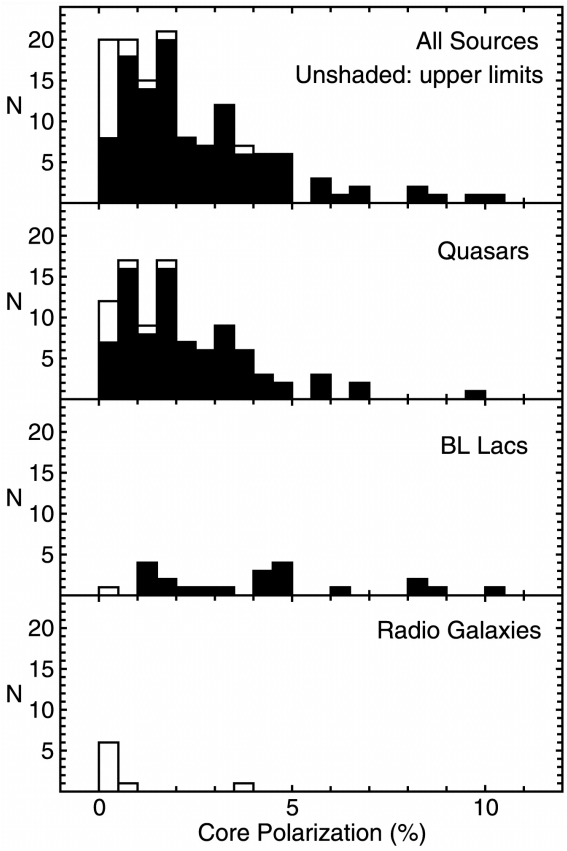

Figure 3.3. Single-epoch fractional polarizations from Lister and Homan 2005, shown for comparison purposes.

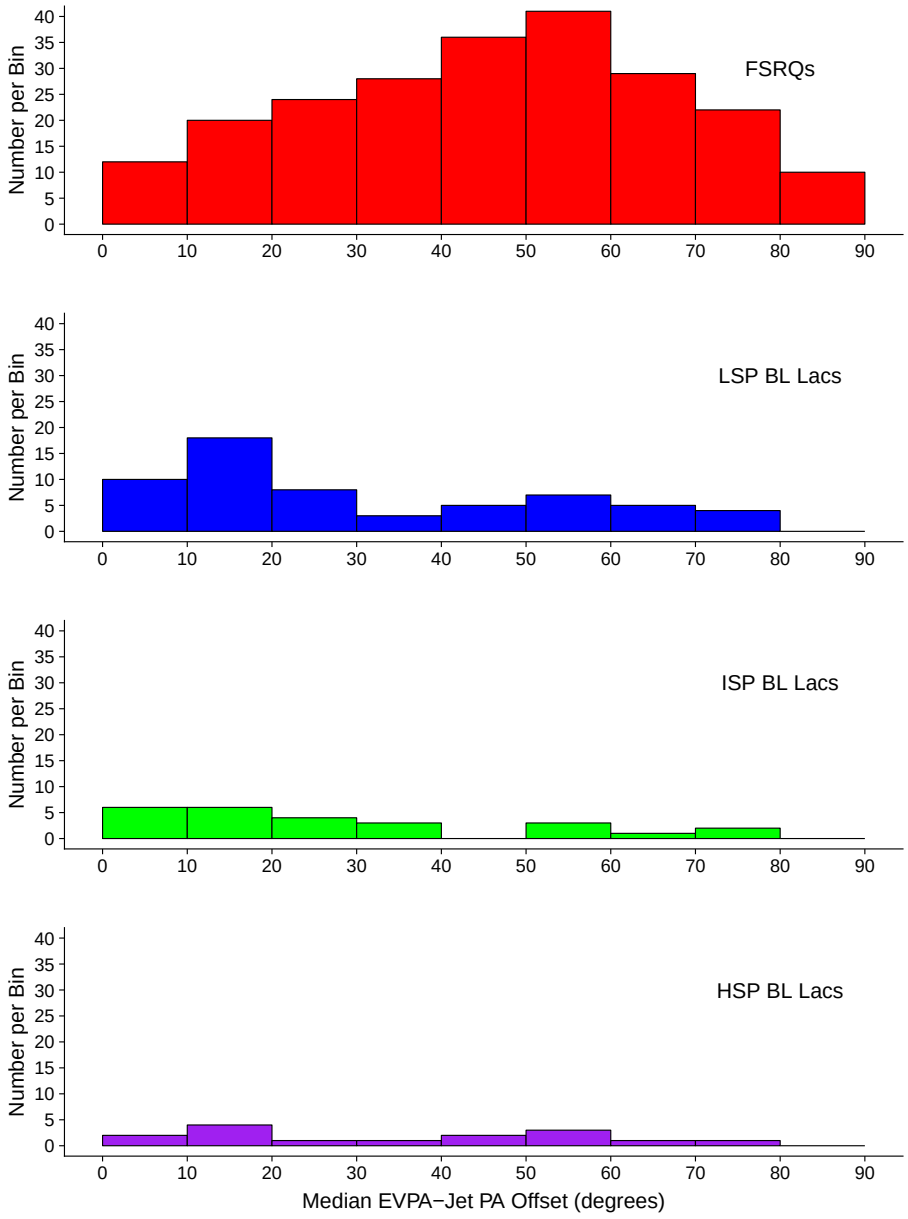

Figure 3.4. Distributions of median EVPA-jet PA offset $|EVPA - PA|_{\rm med}$, grouped by optical/synchrotron peak classification.

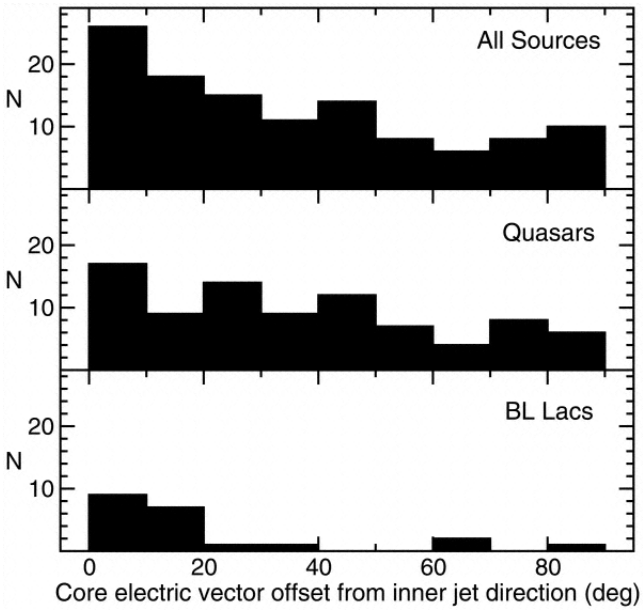

Figure 3.5. Single-epoch EVPA-jet PA offsets from Lister and Homan 2005, shown for comparison purposes.

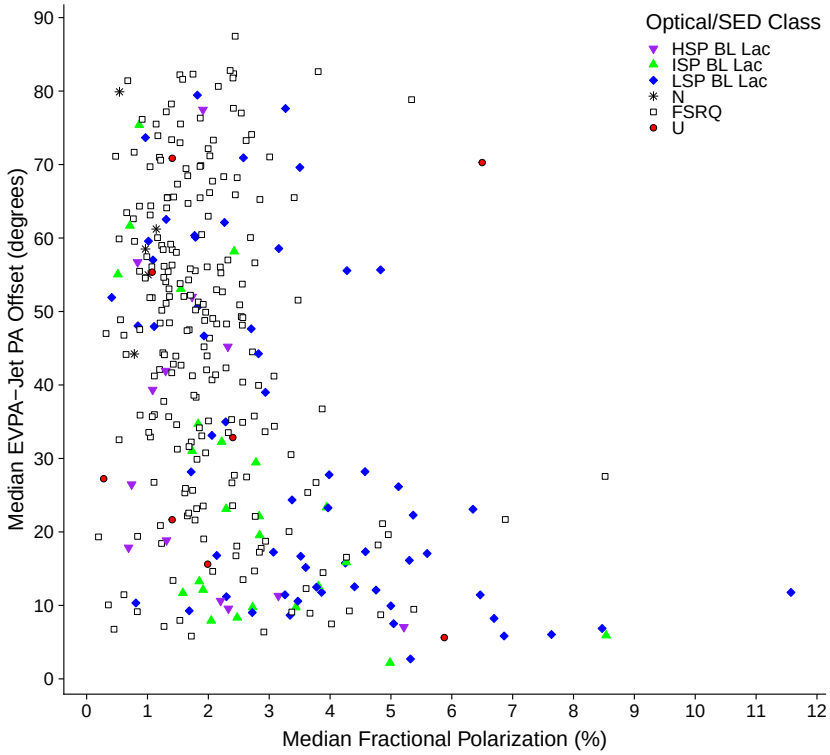

Figure 3.6. Median fractional polarization $m_{\rm med}$ versus median EVPA-jet PA offset $|EVPA - PA|_{\rm med}$ for each AGN over time. Purple inverted triangles are HSP BL Lacs, green triangles are ISP BL Lacs, blue diamonds are LSP BL Lacs, black stars are NLSy1s, unfilled squares are FSRQs, and red circles have an unknown optical class or synchrotron peak frequency. A Kendall τ test of correlation yields $p = 5.3 \times 10^{-13}$ for no correlation.

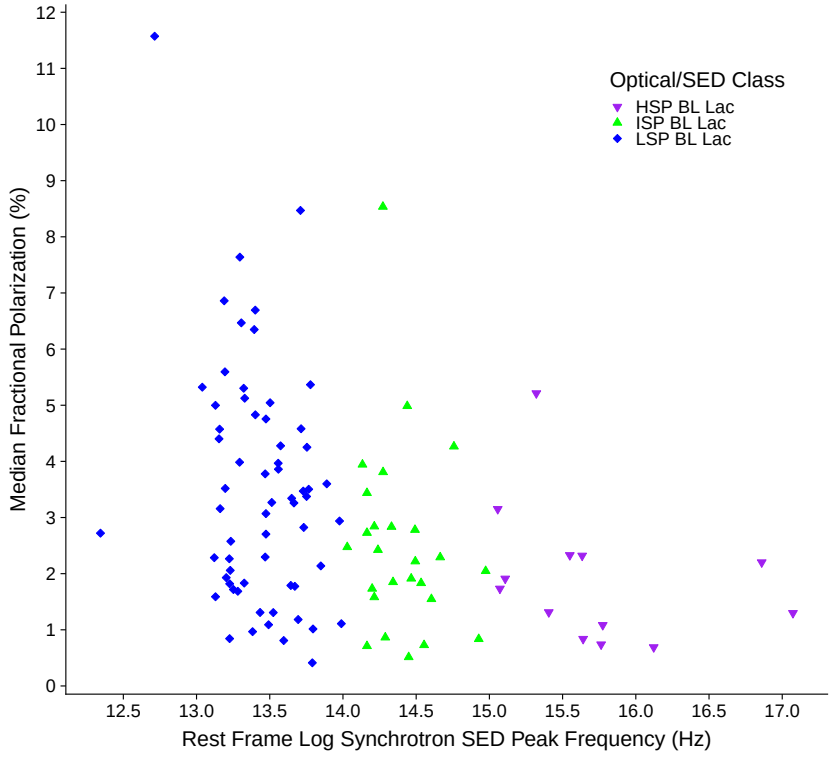

Figure 3.7. Rest frame log synchrotron SED peak frequency versus median fractional polarization $m_{\rm med}$ for BL Lacs in the sample. Purple inverted triangles are HSP BL Lacs, green triangles are ISP BL Lacs, and blue diamonds are LSP BL Lacs. From left to right, the most polarized outliers in each class are S5 0346+80, GB6 J0929+5013, and GB6 J0154+0823. A Kendall τ test of correlation yields $p = 9.1 \times 10^{-5}$ for no correlation.

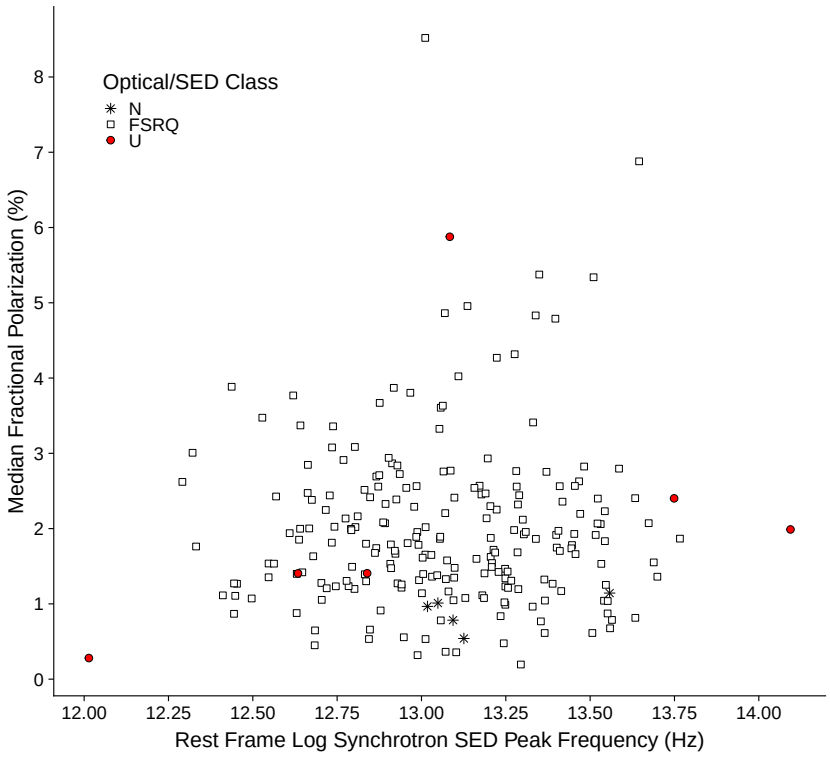

Figure 3.8. Rest frame log synchrotron SED peak frequency versus median fractional polarization m_{med} for non-BL Lacs in the sample. Black stars are NLSy1s, unfilled squares are FSRQs, and red circles have an unknown optical class. The highly polarized outlier is PKS 1236+077. There is no significant correlation.

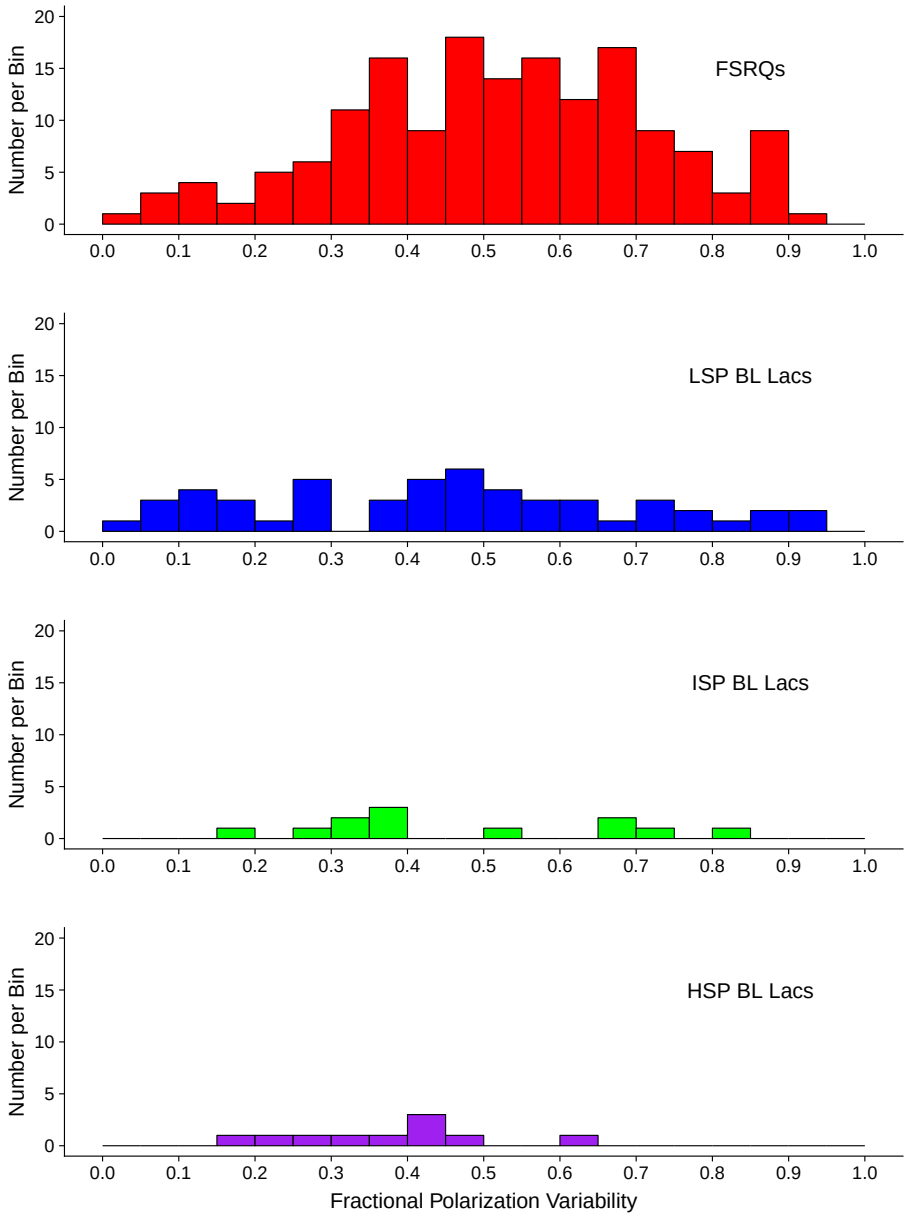

Figure 3.9. Distributions of fractional polarization variability $m_{\rm var}$, grouped by optical/synchrotron peak classification.

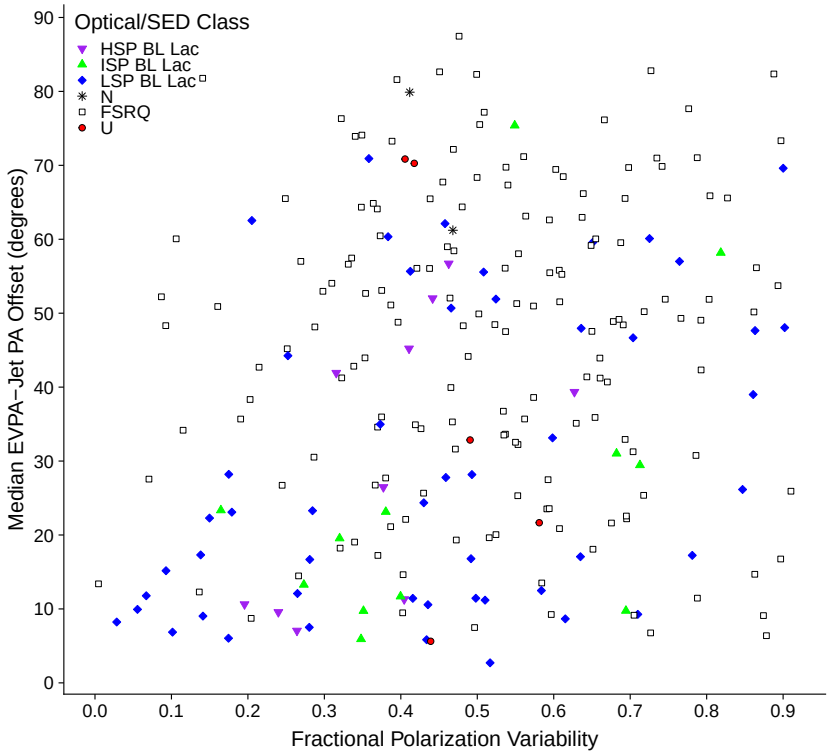

Figure 3.10. Variability in fractional polarization $m_{\rm var}$ versus median EVPA-jet PA offset $|EVPA - PA|_{\rm med}$ for each AGN over time. Purple inverted triangles are HSP BL Lacs, green triangles are ISP BL Lacs, blue diamonds are LSP BL Lacs, black stars are NLSy1s, unfilled squares are FSRQs, and red circles have an unknown optical class or synchrotron peak frequency. A Kendall τ test of correlation yields $p = 0.009$ for no correlation.

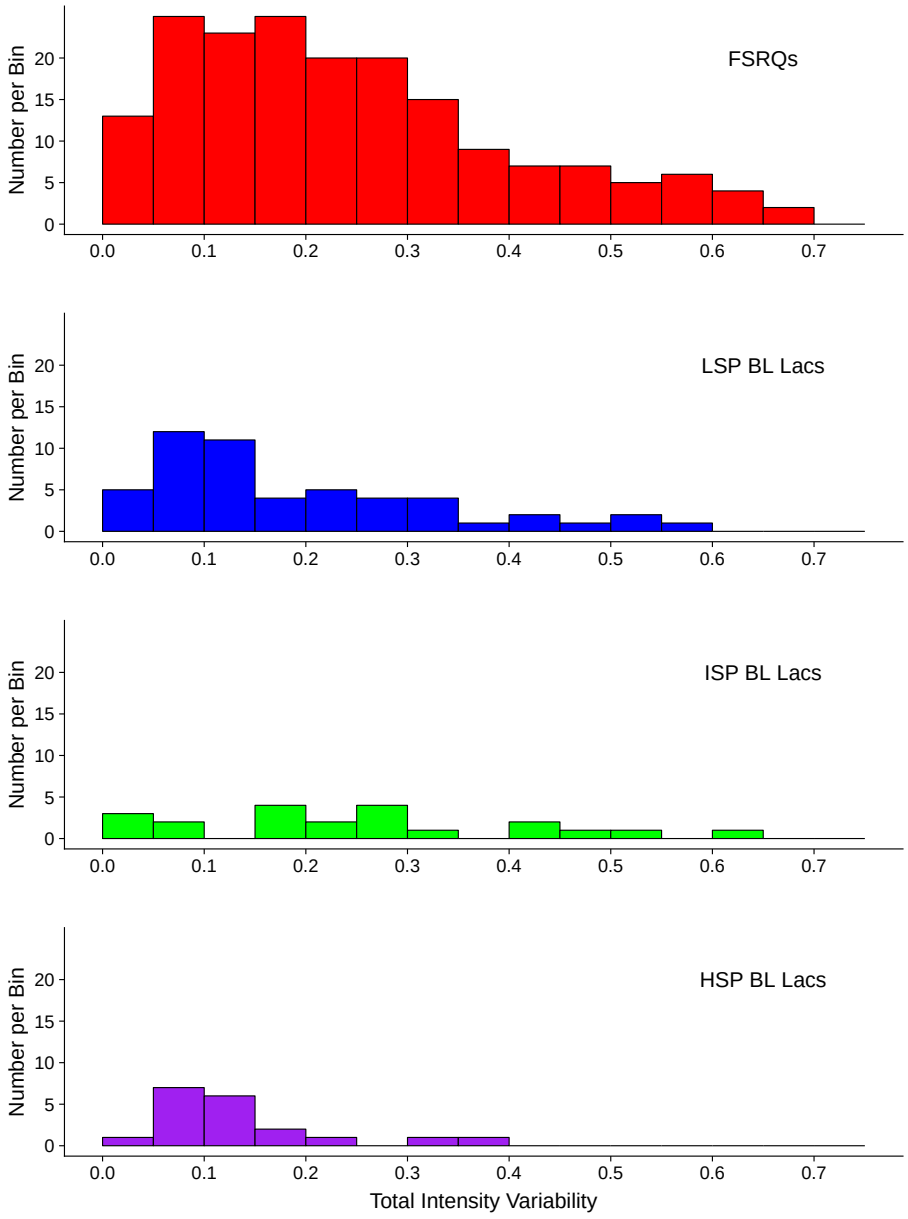

Figure 3.11. Distributions of total intensity variability $I_{\rm var}$, grouped by optical/synchrotron peak classification.

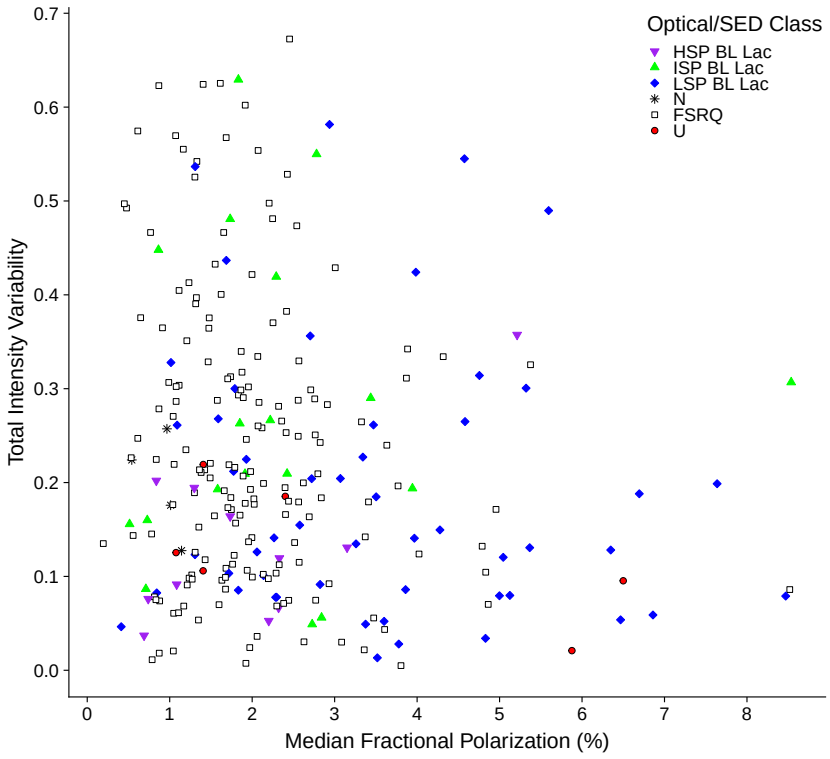

Figure 3.12. Median fractional polarization $m_{\rm med}$ versus total intensity variability $I_{\rm var}$ for each AGN over time. Purple inverted triangles are HSP BL Lacs, green triangles are ISP BL Lacs, blue diamonds are LSP BL Lacs, black stars are NLSy1s, unfilled squares are FSRQs, and red circles have an unknown optical class or synchrotron peak frequency. A Kendall τ test of correlation yields $p = 0.04$ for no correlation.

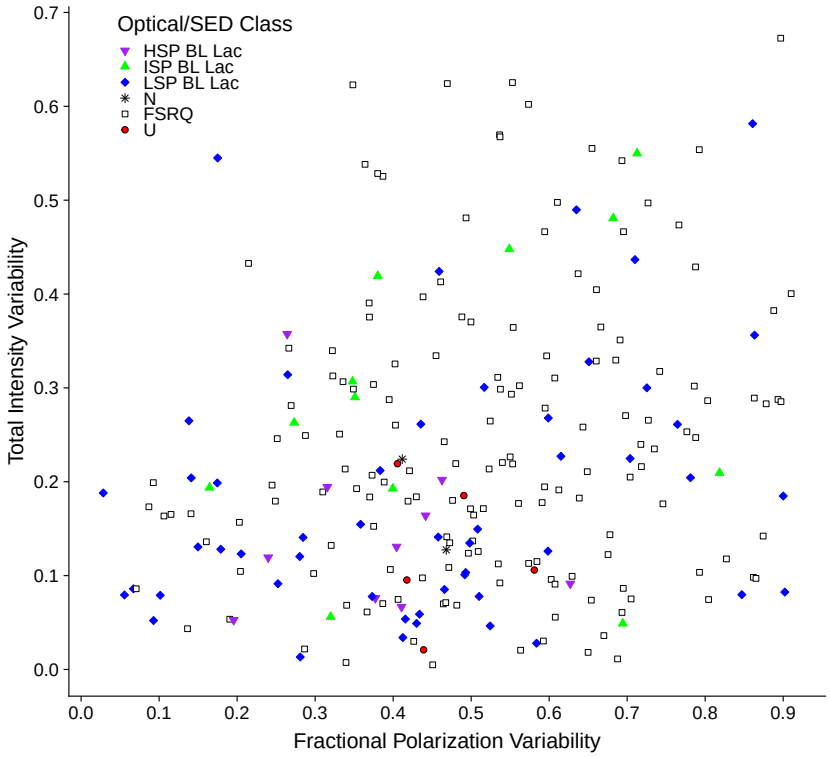

Figure 3.13. Variability in fractional polarization $m_{\rm var}$ versus variability in total intensity $I_{\rm var}$ for each AGN over time. Purple inverted triangles are HSP BL Lacs, green triangles are ISP BL Lacs, blue diamonds are LSP BL Lacs, black stars are NLSy1s, unfilled squares are FSRQs, and red circles have an unknown optical class or synchrotron peak frequency. A Kendall τ test of correlation yields $p = 0.003$ for no correlation.

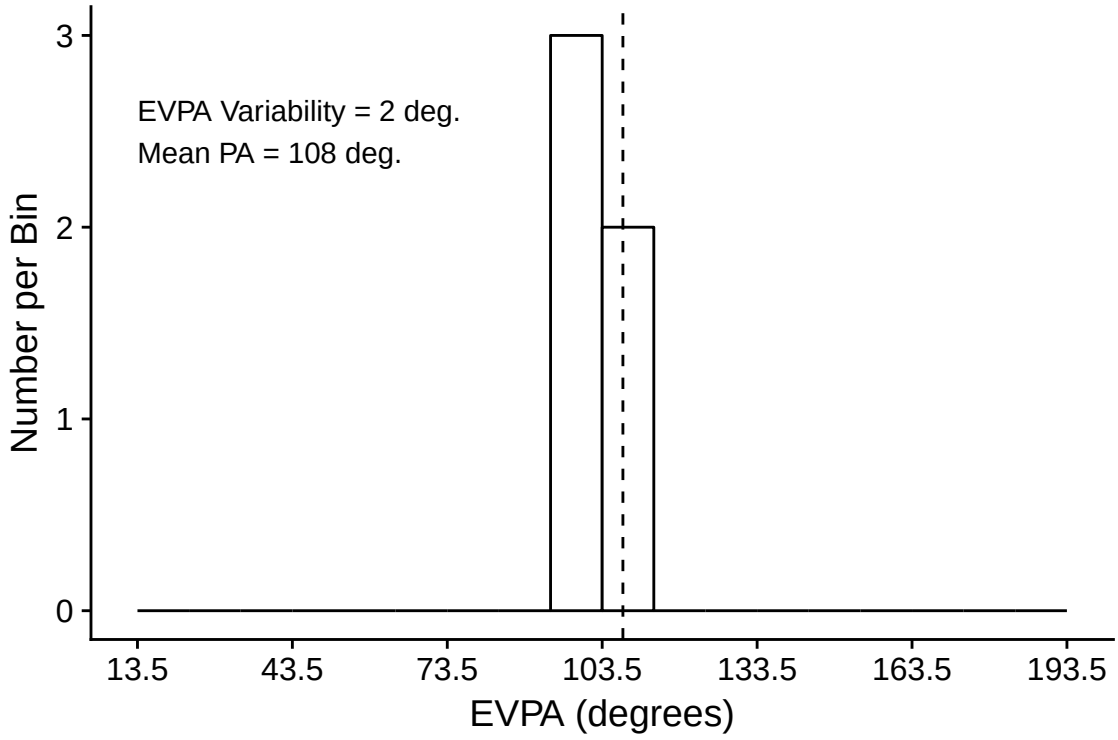

Figure 3.14. The EVPAs used in calculating the standard deviation for 0925+504/GB6 J0929+5013. This AGN is an ISP BL Lac with low EVPA variability $EVPA_{\rm var}$. The circular mean of the jet PAs measured at the same epochs is displayed as a vertical dashed line.

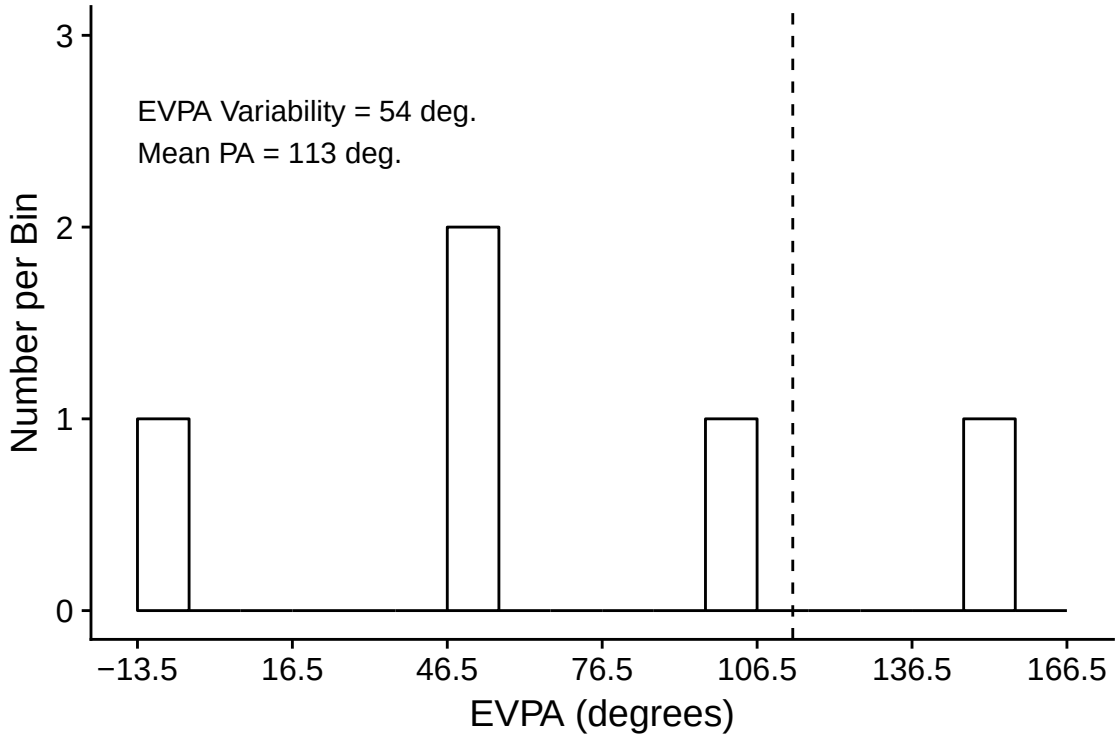

Figure 3.15. The EVPAs used in calculating the standard deviation for 3C 395. This AGN is an FSRQ with high EVPA variability $EVPA_{\rm var}$. The circular mean of the jet PAs measured at the same epochs is displayed as a vertical dashed line.

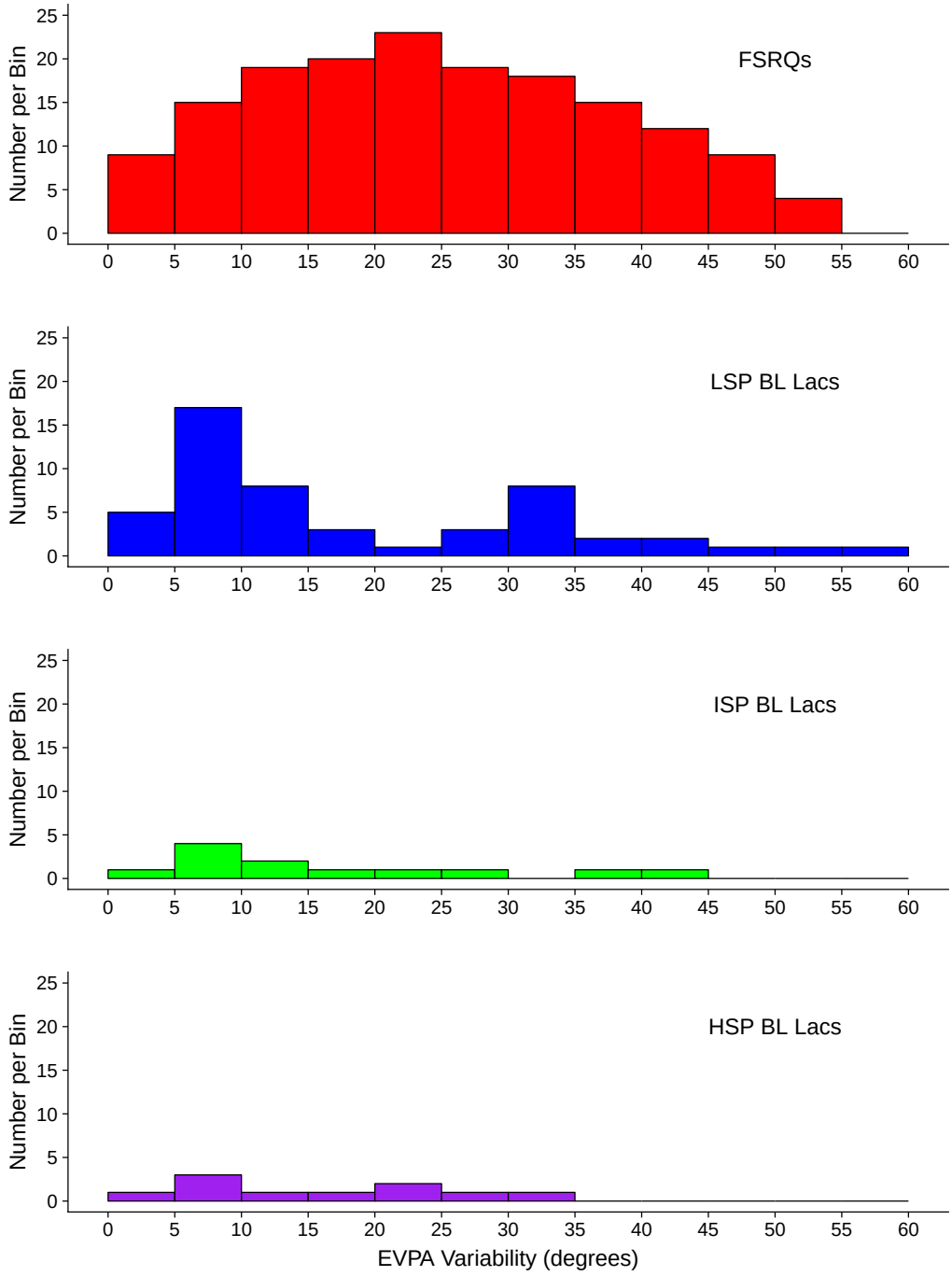

Figure 3.16. Distributions of EVPA variability $EVPA_{\rm var}$, grouped by optical/synchrotron peak classification.

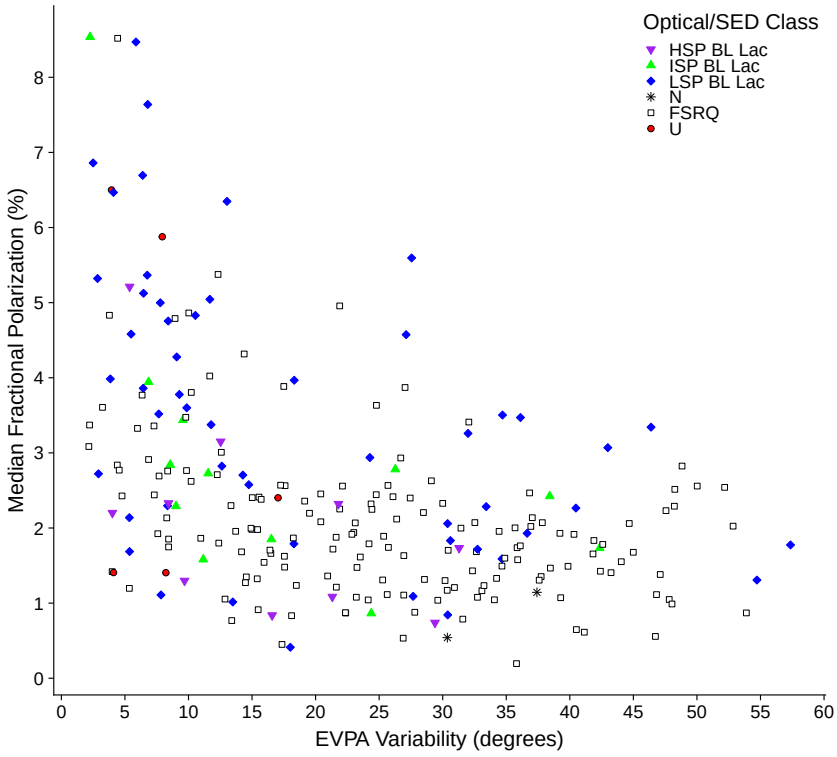

Figure 3.17. EVPA variability $EVPA_{\rm var}$ versus median fractional polarization $m_{\rm med}$ for each AGN over time. Purple inverted triangles are HSP BL Lacs, green triangles are ISP BL Lacs, blue diamonds are LSP BL Lacs, black stars are NLSy1s, unfilled squares are FSRQs, and red circles have an unknown optical class or synchrotron peak frequency. A Kendall τ test of correlation yields $p = 1.9 \times 10^{-13}$ for no correlation.

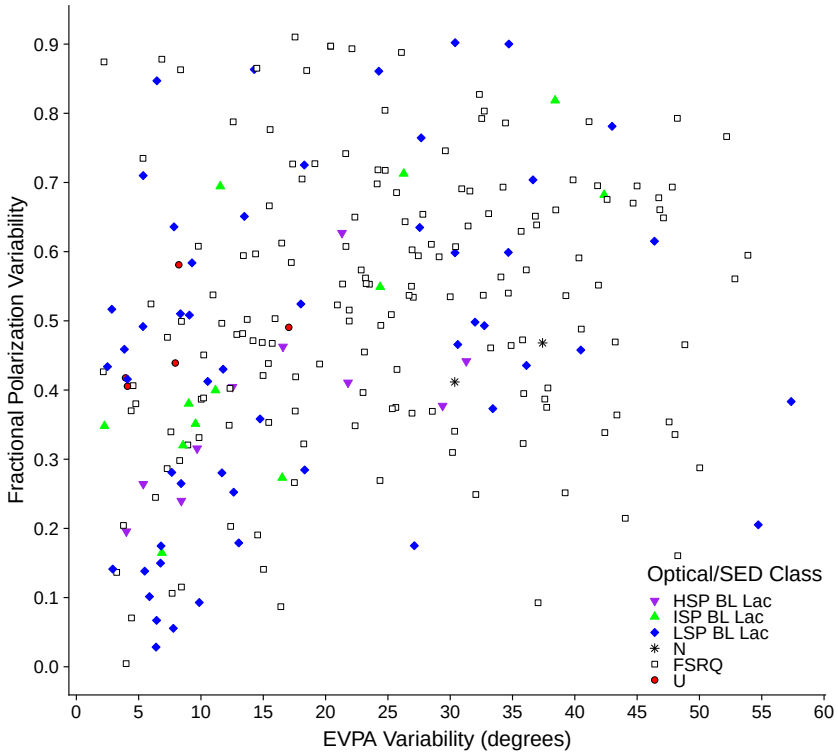

Figure 3.18. EVPA variability $EVPA_{\rm var}$ versus fractional polarization variability $m_{\rm var}$ for each AGN over time. Purple inverted triangles are HSP BL Lacs, green triangles are ISP BL Lacs, blue diamonds are LSP BL Lacs, black stars are NLSy1s, unfilled squares are FSRQs, and red circles have an unknown optical class or synchrotron peak frequency. A Kendall τ test of correlation yields $p = 4.1 \times 10^{-7}$ for no correlation.

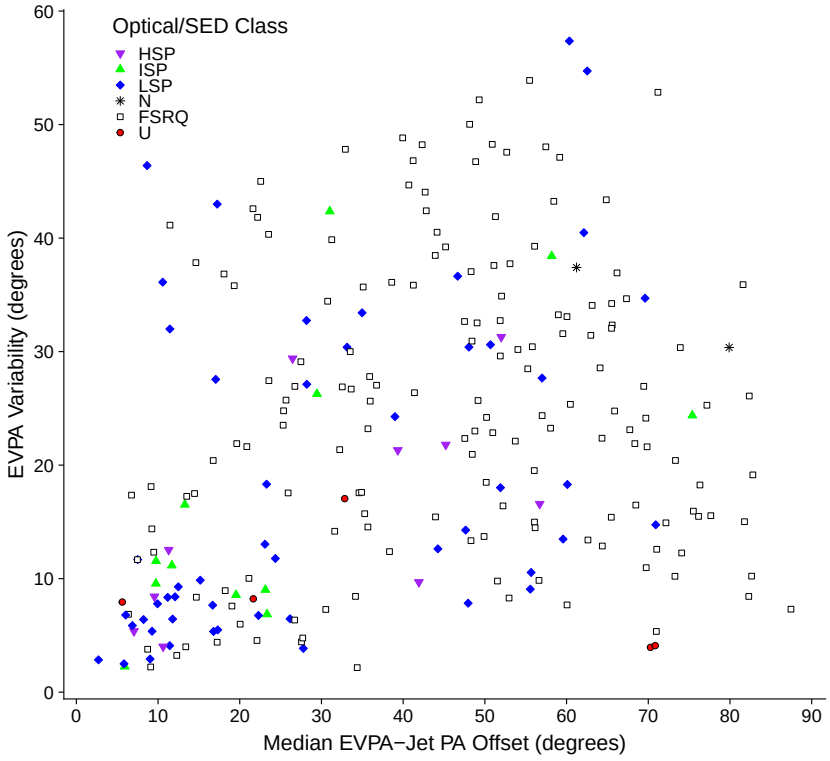

Figure 3.19. Median EVPA-jet PA offset $|EVPA - PA|_{\rm med}$ versus EVPA variability $EVPA_{\rm var}$ for each AGN over time. Purple inverted triangles are HSP BL Lacs, green triangles are ISP BL Lacs, blue diamonds are LSP BL Lacs, black stars are NLSy1s, unfilled squares are FSRQs, and red circles have an unknown optical class or synchrotron peak frequency.

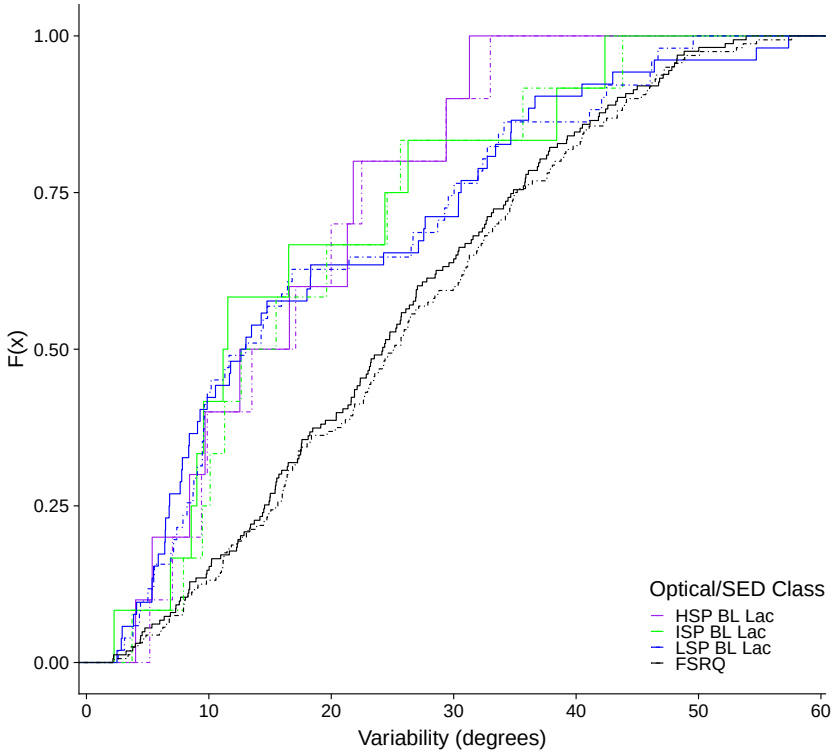

Figure 3.20. Cumulative distribution functions of EVPA (solid lines) and EVPA-PA (dash-dotted lines) variability ($EVPA_{\rm var}$ and $(EVPA - PA)_{\rm var}$), grouped by optical/synchrotron peak classification. HSP BL Lacs are purple, ISP BL Lacs are green, LSP BL Lacs are blue, and FSRQs are black.

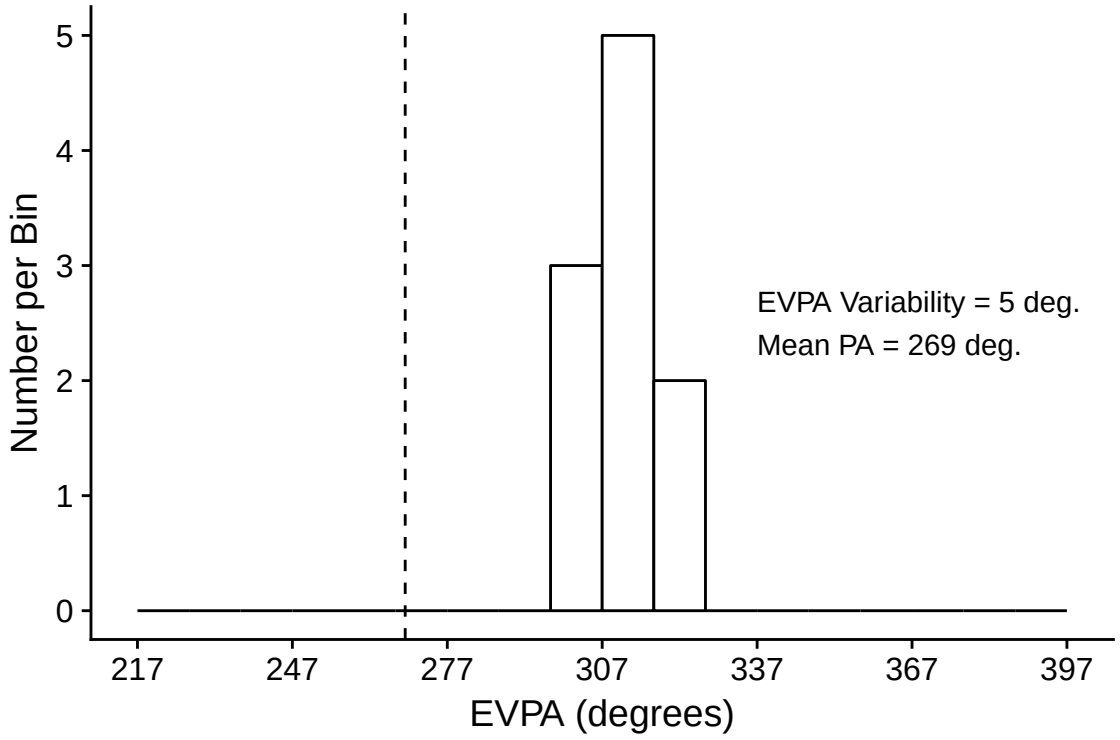

Figure 3.21. The EVPAs used in calculating the standard deviation over all epochs for OX 161. This AGN has the lowest EVPA variability $EVPA_{\rm var}$ in the sample when all epochs are used in calculation. The circular mean of the jet PAs measured over all epochs is displayed as a vertical dashed line.

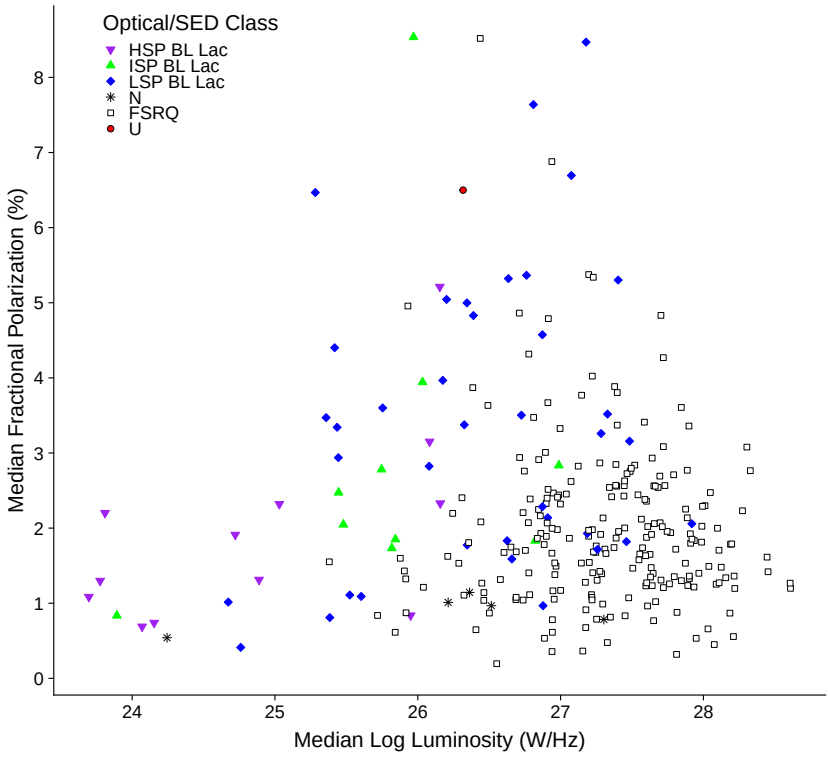

Figure 3.22. Median luminosity $L_{\rm med}$ versus median fractional polarization $m_{\rm med}$ for each AGN over time. Purple inverted triangles are HSP BL Lacs, green triangles are ISP BL Lacs, blue diamonds are LSP BL Lacs, black stars are NLSy1s, unfilled squares are FSRQs, and red circles have an unknown optical class or synchrotron peak frequency. There is no significant correlation. A Kendall τ test of correlation yields $p = 0.007$, $\tau = 0.23$ for no correlation if FSRQs are excluded, however.

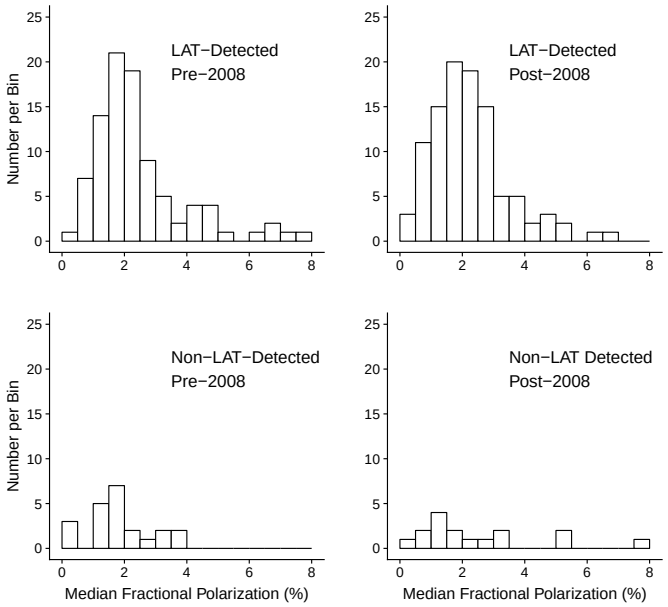

Figure 3.23. Distributions of median fractional polarization $m_{\rm med}$, calculated separately using all epochs pre-August 4th, 2008 (left) and all epochs after (right) based on the start of *Fermi*-LAT observations. AGN are grouped as LAT-detected (top) or non-LAT-detected (bottom).

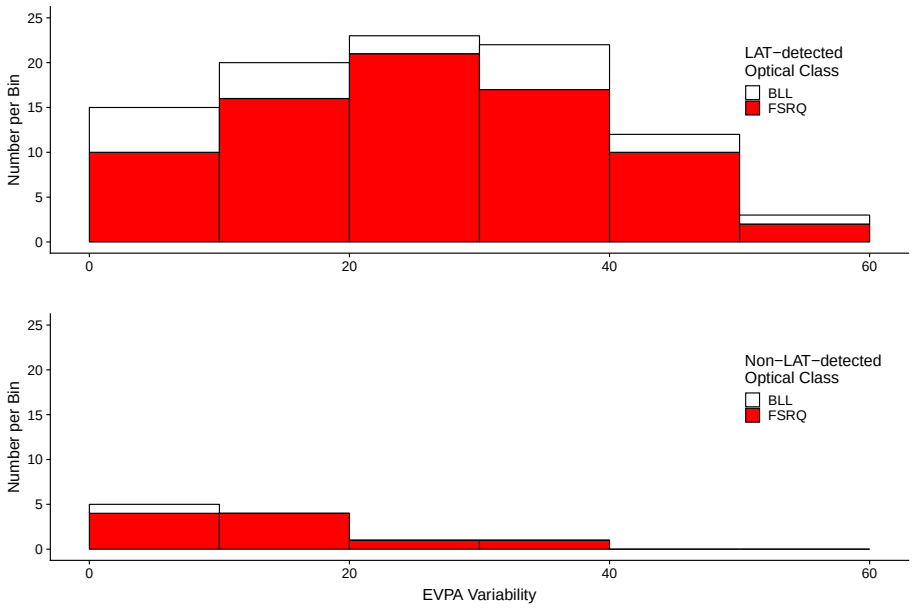

Figure 3.24. Distributions of EVPA variability $EVPA_{\rm var}$. AGN are grouped as LAT-detected (top) or non-LAT-detected (bottom). Unfilled bins represent the entire sample and red bins represent FSRQs.

4. Jet Speeds

In Chapter 3, differing Doppler boosting factors are given as a possible cause for the anti-correlation present between synchrotron SED peak frequency and fractional polarization. Additionally, the role of relativistic boosting in altering the statistics in Chapter 3 is highly relevant to the comparisons made concerning radio correlations with γ-ray detection. Since the Doppler boosting factor and the apparent jet speed both depend on the Lorentz factor and the jet viewing angle, this chapter explores the relationship between jet apparent speeds, fractional polarization, and variability measures through the use of angular proper motion measurements.

4.1 Measurements and Conversions

4.1.1 Angular Proper Motion

The VLBA's high, milliarcsecond-scale resolution allows measurements of the core as well as bright features moving down the jet. Many of these features can be observed over multiple epochs, and thus their kinematic properties can be fitted (Kellermann et al., 2004). The MOJAVE program attempts two types of fits: constant velocity (for components/features with at least five reliable epochs of identification) and constant acceleration (for components with at least ten reliable epochs of identification; Lister et al. 2016b). The most recent model is explained in Lister et al. 2019; due to the presence of non-radial motion in some components and the observational constraints on known ejection time, the model fits the feature's position at the midpoint in time between the first and last observation, rather than fitting for its epoch of origin (such as in Lister et al. 2009 and Homan et al. 2009.) The angular proper speed of the acceleration fit is used unless it gives a $< 3\sigma$ acceleration, or the component lacks the

number of epochs with identification described above. The error on the measurements of component positions is described in Lister et al. 2009, and constitutes the greatest source of error on the final derived apparent speeds.

This chapter only concerns the speeds for jets within the polarization sample described in Section 3.1. As in previous chapters, no epochs after December 31st, 2016 are used in the analysis; however, no bias corrections are performed on the speed data. The kinematic fits cannot support random sampling of epochs such as used for the polarization statistics. Observing statistics are also of less concern, though. Polarization phenomena such as EVPA rotations generally take place on shorter timescales than the emergence and subsequent fade of new jet components, such that only the former is likely to be missed with the typical MOJAVE observation cadence.

A "robust" component is one that can be identified over at least five epochs. Among the statistically significant ($\mu \geq 3\sigma_\mu$) speeds from a particular jet's robust components, the greatest is defined as the jet's maximum angular speed ($\mu_{\rm max}$). If a $\mu \geq 3\sigma_\mu$ speed is not available, $\mu_{\rm max}$ is picked from the $\mu \geq 2\sigma_\mu$ speeds; if this is also not possible, $\mu_{\rm max}$ is chosen to be the speed of the feature with the least error. The $\mu_{\rm max}$ statistic is available for 316 of the 387 sources within the sample. For the 89 sources with at least five robust components, a median speed ($\mu_{\rm med}$) is also calculated. Because $\mu_{\rm med}$ is calculated from the speeds of all robust components, regardless of their error σ_μ, in rare cases $\mu_{\rm med}$ can be greater than $\mu_{\rm max}$. In Figure 4.1, the two speed statistics are plotted against each other. While there are cases of pattern speeds dissimilar to a jet's median speed, Lister et al. 2013a and Lister et al. 2019 find that features are typically ejected within a narrow range around a "characteristic" speed.

4.1.2 Apparent Speed and Doppler Boosting

The angular speeds represent the observed proper motion in units of milliarcseconds/year (mas/yr). They can be converted to the apparent speed through

$$\beta_{app} = \frac{\mu D_L}{(1+z)}, \tag{4.1}$$

where D_L is the luminosity distance which relates the bolometric luminosity and bolometric flux (Hogg, 1999; Homan et al., 2009). The luminosity distance is calculated using the cosmological parameters stated in the beginning of Chapter 3.

Equation 1.5 expresses the Doppler boosting factor in terms of the Lorentz factor, γ, the speed, β, and the viewing angle, θ; these measures are also related by

$$\beta_{app} = \beta\Gamma\delta\sin\theta \tag{4.2}$$

(Cohen et al., 2007). The apparent speed alone can then only partially constrain the intrinsic properties of the jet. This can be seen in, e.g., Figure 5 of Vermeulen and Cohen 1994, which shows the value of β_{app} which are measured for different values of θ, γ, and δ. The apparent speed increases with Lorentz factor for a given viewing angle. However, the relationship between the Doppler boosting factor and the Lorentz factor depends on whether the jet is viewed above or inside the critical angle of $1/\Gamma$. The Doppler factor cannot be measured directly and attempts to estimate it must rely on several assumptions; see, e.g., the summary in Liodakis et al. 2018. The highest values of β_{app} in this analysis ($\sim$40c) necessitate a small viewing angle and high Doppler factor, but lower values of the apparent speed can result from a larger range of Lorentz factor values. A majority of sources in the sample must have at least some degree of beaming, considering their high redshift and the flux-limited nature of the catalogue (see Lister et al. 2009).

Figure 4.2 shows the distribution of apparent speeds in the sample, divided by optical/synchrotron peak SED frequency classification (one BL Lac with unknown synchrotron peak is not shown, as well as five Narrow Line Seyferts 1s with speeds generally similar to those discussed in Lister et al. 2016b). FSRQs are likely to have

the highest intrinsic speeds (e.g., Kharb et al. 2010), leading to their high apparent speeds; although their true viewing angles are unknown, it is possible that they are smaller than those of BL Lacs as well (Hovatta et al., 2009).

BL Lac speeds decrease with increasing synchrotron peak (see also Lister et al. 2019, suggesting some sort of inherent difference between the subclasses. The observing frequency of 15 GHz falls closer to the synchrotron SED peak of LSP sources than HSP sources, resulting in lower HSP BL Lac luminosities. Even at similiar redshifts, HSP BL Lacs have lower speeds than LSP BL Lacs; selection effects would favor beamed sources at greater speeds, in order for HSP BL Lacs to enter the flux-limited catalogue. It is more likely that HSP BL Lacs simply have lower intrinsic speeds. This would agree with the lower kinetic powers expected from HSP BL Lacs under the "blazar sequence" (Fossati et al., 1998; Ghisellini et al., 1998). The generally low apparent speeds of radio galaxies are thought to be due to their higher angles to the line of sight; 0415+379/3C 111 and 0430+052/3C 120 are the two major ($\beta_{app} > 6$) exceptions.

4.2 Analysis

4.2.1 Fractional Polarization

Figure 4.3 shows all available apparent maximum speeds plotted against the AGN's median core fractional polarization (as described in Chapter 3). There is no clear overall trend, but the locations of the distributions are as expected, with FSRQs largely present at low polarization and higher speeds while BL Lacs extend in the opposite dimensions. For clarity, Figure 4.4 shows the same data separated into two plots (see Section 4.2.3 regarding the locations of NLSy1s).

The BL Lac population, when considered on its own, shows a positive correlation between median fractional polarization and maximum apparent speed ($p = 0.019$, $\tau = 0.22$ when performing a Kendall τ non-parametric correlation test; the probability of the null hypothesis, as described in greater detail in Section A.3). Among FSRQs

alone, there is no correlation between median fractional polarization and maximum apparent speed. This also is true if the extreme polarization outlier (PKS 1236+077, $m = 8.52\%$) is not considered. The peak speed jets have an approximate fractional polarization $m \approx 2\%$, apparently due to the FSRQ population density rather than a specific preference for low speeds below $m \approx 1\%$ or above $m \approx 3\%$. Figure 4.5 shows the FSRQ data with overlaid apparent speed averages calculated from bins of size $m = 1\%$; the averages for each bin are approximately equal.

We also investigate the relationship between median fractional polarization and median apparent speed with data shown in Figure 4.6. Once again, there are no trends when blazar classes are combined together. When FSRQs are tested alone, though, there is a positive correlation between the two statistics ($p = 0.017$, $\tau = 0.22$; BL Lacs are not tested separately due to small numbers.) This would suggest a discrepancy between the typical and the fastest components within the jet in regards to the core's polarization. However, a median apparent speed and median fractional polarization is only available for 57 of the FSRQs which have at least five measured component speeds. When the maximum apparent speeds of the same 57 are analyzed, they also appear to correlate with the fractional polarization ($p = 0.002, \tau = 0.28$; see Figure 4.7).

This almost certainly represents the difference in observational metrics for the two groups. The FSRQs with an available $\beta_{\rm med}$ and $m_{\rm med}$ have a median $\beta_{\rm max} = 15.8c$, and have been observed for a median of 13.6 years. The FSRQs with $m_{\rm med}$ and $\beta_{\rm max}$, but no $\beta_{\rm med}$, have a median $\beta_{\rm max} = 7.2c$ and have been observed for a median of 5.1 years. Most AGN jets eject a new feature every few years (Lister et al., 2016a). This suggests that as the MOJAVE program continues, the maximum component speeds of the latter group will rise and approach a more linear relationship with the fractional polarization.

Because of blazars' low angles to the line of sight and other likely values for the intrinsic properties (see, e.g., the simulations in Lister et al. 2019), we can take their component apparent speeds to be indicative of the degree of beaming present. The

relationships between polarization and beaming characteristics have been rarely investigated. A study using an older version of the MOJAVE sample, Kharb et al. 2010, divided FSRQs into high optical polarization ($m_{opt} > 3$) and low optical polarization ($m_{opt} < 3$) categories and found that the former had significantly higher speeds. Hovatta et al. 2009 estimated the Doppler boosting factors for a sample of 67 sources from mm-wave flaring events; using MOJAVE speeds and the same optical polarization-based categories, they additionally found that the higher optically polarized FSRQs have significantly higher Doppler boosting factors.

The results from this section provide evidence that this trend between higher polarization and higher jet speeds exists for the radio core polarization as well as the optical polarization. The low polarization of HSP BL Lacs can then be explained by their suspected lower degree of Doppler boosting. In addition, we find that EVPA-based characteristics have no significant trends with apparent jet speeds, and in Chapter 3, we found that those characteristics also seemed unaffected by synchrotron peak within the BL Lac class. If processes within the jet increase the core fractional polarization as well as the speed of ejected components, they appear to have no effect on the EVPA. These results together then support a scenario where BL Lacs all have intrinsically different polarization properties than FSRQs — based on their EVPA behavior and extremely high fractional polarization relative to their apparent speeds — but synchrotron peak-based classes within the larger BL Lac group have a fractional polarization modified by the amount of Doppler boosting.

4.2.2 Variability Measures

In this section, we investigate the link between jet apparent speeds and variability measures, where the underlying variability is modified by several effects. One of these effects is the relativistic shortening of time scales. If a jet has a viewing angle close to zero such that $\cos(\theta) \approx 1$ and a Lorentz factor $\Gamma \approx 10$, for example, it is experiencing time a factor of twenty times slower than measured by the observer (Eq. 1.6). Because

the actual relativistic factors are not known, they cannot be easily accounted for — the statistical debiasing of variability measures described in Section 3.2.1 is based only in observer time. The fastest jets are still being measured over a shorter time (in their rest frame) than slower jets.

Another consideration is the assumptions regarding the core versus jet boosting factors. The features of a particular jet are measured as having a variety of speeds, potentially due to varying shock characteristics (Homan et al., 2015). In a sample of this size, is it reasonable to assume that the typical feature speed and likely Doppler factor range based on that speed is generally indicative of the core Doppler boosting factors. If the core Doppler factor changes — due to e.g. a particularly fast moving feature emerging from the core — then the flux measured at that epoch is changed from the intrinsic flux as described in Section 1.1.2. Because the formula is nonlinear, jets with higher Doppler factors will have a greater total intensity variability (Section 3.2.5) for similar intrinsic changes in the de-boosted flux. This may cause greater variability in jets with higher Doppler boosting factors (such as reported in the radio regime by Tingay et al. 2001 and Liodakis et al. 2018)

In Figure 4.8, we plot the total intensity variability indices $I_{\rm var}$ from Chapter 3 against the maximum jet component speed. We find no correlations for blazars as a whole or among the two blazar subgroups. Likewise, blazars and FSRQs specifically (there are too few BL Lacs to test separately) do not have an apparent correlation between their total intensity variability and median jet component speed. The variability in fractional polarization (Section 3.2.4) similarly has no correlations with either apparent speed measure across blazar groupings (for the maximum apparent component speeds, this can be seen in Figure 4.9).

For comparison purposes, we examine another measure of flux variability — the intrinsic modulation index of the OVRO 40m monitoring program (Richards et al., 2014). The modulation index is calculated from 4 years of data and is not restricted to the core feature. However, the OVRO program monitors much more frequently than MOJAVE, using considerably more measurements in its variability calculation.

Like the total intensity variability, the OVRO modulation index is de-biased in terms of observing statistics (Richards et al., 2011), hence the name "intrinsic."

In Figure 4.10 and Figure 4.11, we plot the OVRO intrinsic modulation index against the maximum jet apparent speeds and median jet apparent speeds, respectively. In the case of the maximum speeds, a very slight correlation is present among all blazars ($p = 0.038, \tau = 0.0992$), with the same true of BL Lac objects ($p = 0.040, \tau = 0.192$) but not FSRQs. A more certain correlation exists between the modulation index and the blazar median speeds ($p = 0.002, \tau = 0.269$); there are only 14 BL Lacs in this group, but the 51 FSRQs also show a correlation with $p = 0.013, \tau = 0.240$. Even with these results, a stronger correlation might be expected, especially given the findings of the previous section.

4.2.3 Narrow Line Seyfert 1s

The five Narrow Line Seyfert 1s discussed in this work represent a small minority within the class; they are extremely radio-loud, with properties similar to those of blazars (Lister, 2018). In particular, these and other γ ray-detected NLSy1s are most like FSRQs (see Paliya et al. 2019 and references therein), with some literature even suggesting that they are the young evolutionary equivalent of FSRQs (Foschini, 2017). As seen in Figure 4.4, the maximum apparent jet component speed and median fractional polarization of the NLSy1s in our sample are most like those of FSRQs, but clustered at relatively low values. The highest NLSy1 speed, $9.69c$, is above the median $\beta_{\rm max} = 7.27c$ for all available FSRQs. The highest NLSy1 fractional polarization is $m_{\rm med} = 1.41\%$; the median for FSRQs is $m_{\rm med} = 1.92\%$. With so few data points, it cannot be said whether the low polarization is by chance or representative for this rare type within the NLSy1 class.

4.2.4 Correlations with γ-ray Emission

In Section 3.2.10, we defined a blazar subsample for the purpose of exploring how radio properties differ based on whether a population of AGN has associations in the *Fermi* third source catalog (Acero et al., 2015b). Here, we again use this subsample to analyze the relationship between median core fractional polarization and jet component speed between LAT-detected and non-LAT detected groups. The apparent speeds of γ-ray detected AGN are well known to be higher than those of non-detected AGN, with the main motivators for LAT detection thought to be high γ to radio ratio (dependent on synchrotron peak frequency location) and highly boosted emission (Lister et al., 2015). In Figure 4.12, we show the distribution of maximum apparent jet speeds for the blazars which meet the criteria in Section 3.2.10 (to summarize, radio-selected blazars).

These apparent speeds are plotted with median fractional polarization in Figure 4.13. We find no significant correlations among the LAT-detected or non-detected groups; this is true as well if tests are limited to include only FSRQs. LAT-detected median apparent speeds also show no significant correlations with fractional polarization (there are too few non-detected AGN to test separately). The LAT-detected group consists of a mix of FSRQs and mostly LSP BL Lacs, while the non-LAT detected group is almost entirely FSRQs. It is possible that BL Lacs have the widest range of potential Doppler boosting factors, resulting in a more obvious correlation than is more tenuously seen in FSRQs, and not seen at all among the populations divided by γ-ray detection status.

4.3 Summary

In this chapter, used maximum and median apparent jet speed statistics from the MOJAVE program to explore the relationships between relativistic boosting and fractional polarization, as well as the variability measures used in Chapter 3 and beyond. Our conclusions are:

1. The fractional polarization of BL Lacs is positively correlated with their maximum apparent jet speeds. This is also true of FSRQs when it comes to both measures of apparent speed, but only when a smaller subset of the most heavily observed FSRQs are tested. Since the values of the apparent jet speeds seem to have no relationship with EVPA-based statistics, this supports the idea that the HSP/LSP BL Lac divide in polarization is a result of differing relativistic beaming factors.

2. We find no correlations between maximum or median apparent jet speed and our total intensity and fractional polarization variability measures. However, the intrinsic modulation index, a total intensity flux variability measure from the OVRO 40m monitoring program, is by contrast correlated with our speed measues. Since variability is expected to increase with increasing jet Doppler factor, this highlights the need for more robust variability statistics.

3. NLSy1 sources have low polarization, even given their apparent jet speeds, but data on a larger sample are needed for definite conclusions.

4. We divided blazars by their *Fermi*-LAT γ-ray association or lack thereof, but found no correlations between fractional polarization and jet apparent speed within those groups. It is not surprising that a link between fractional polarization and apparent speed, indicating the level of beaming, would not be seen when the LAT-detected and non-detected groups are tested separately. However, it suggests that the correlation is rather weak, and most obvious when observed in BL Lacs due to their presumed wider range of Doppler factors and less spread fractional polarization values.

Overall, our results confirm the current literature regarding the blazar paradigm; some of our more preliminary results could benefit from future use of data on a larger sample of AGN.

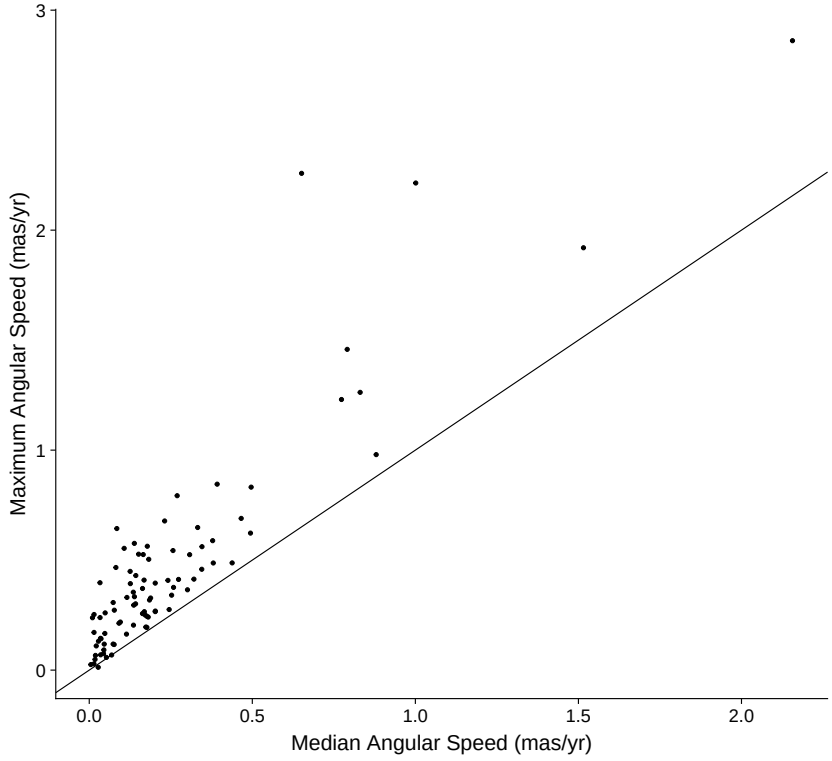

Figure 4.1. Median angular speed versus maximum angular speed in mas for each AGN. A 1:1 line is overlaid on the plot.

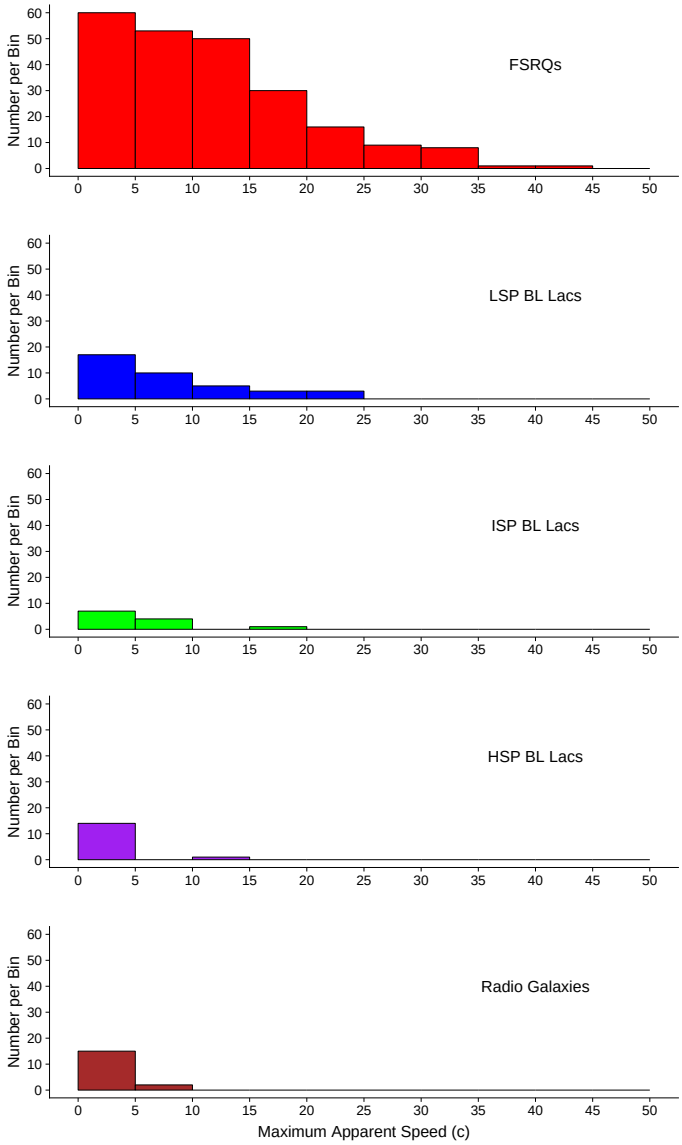

Figure 4.2. Distributions of maximum apparent speed $\beta_{\max}$, grouped by optical/synchrotron peak classification. The ISP outlier is 0716+714/TXS 0716+714 and the HSP outlier is 0219+428/3C 66A.

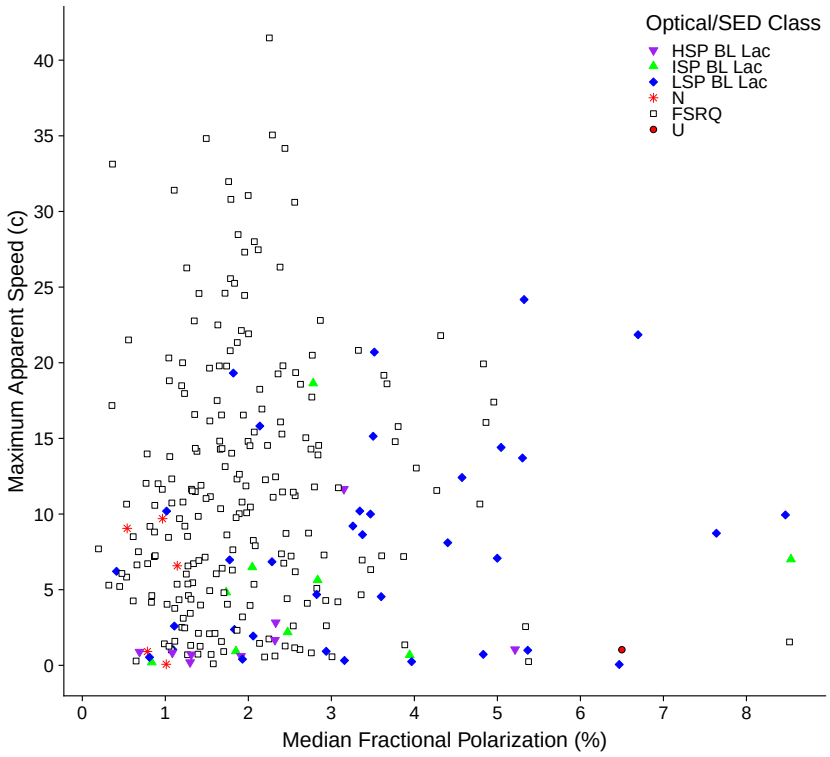

Figure 4.3. Median core fractional polarization $m_{\rm med}$ versus maximum apparent speed $\beta_{\rm max}$ for each AGN. Purple inverted triangles are HSP BL Lacs, green triangles are ISP BL Lacs, blue diamonds are LSP BL Lacs, red stars are NLSy1s, unfilled squares are FSRQs, and red circles have an unknown optical class or synchrotron peak frequency.

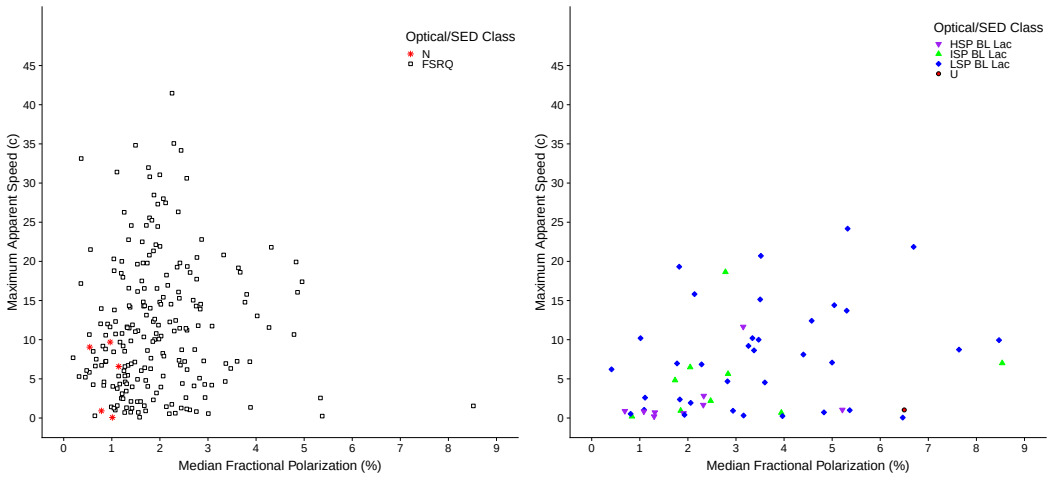

Figure 4.4. Median core fractional polarization $m_{\rm med}$ versus maximum apparent speed $\beta_{\rm max}$ for each AGN. Left panel: red stars are NLSy1s and unfilled squares are FSRQs. Right panel: purple inverted triangles are HSP BL Lacs, green triangles are ISP BL Lacs, blue diamonds are LSP BL Lacs, and the red circle has an unknown synchrotron peak frequency. A Kendall τ test of correlation yields $p = 0.019$ for no correlation in the BL Lac population.

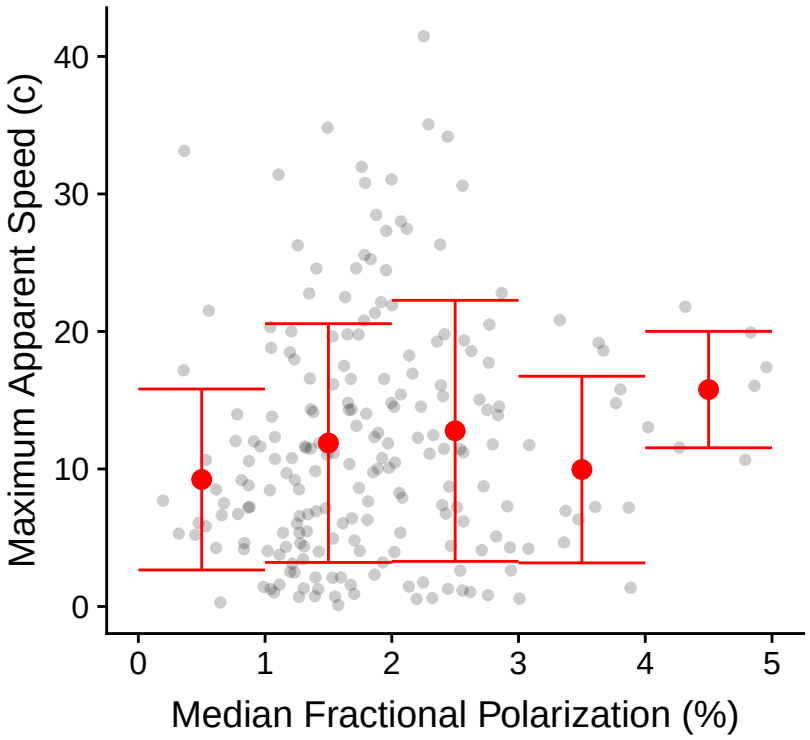

Figure 4.5. Median core fractional polarization $m_{\rm med}$ versus maximum apparent speed $\beta_{\rm max}$ for the FSRQ optical class, minus the 3 AGN with $m_{\rm med} > 5$. Red circles are based on apparent speeds averages for a particular bin of size $m_{\rm med} = 1\%$. Red error bars represent the mean apparent speed plus and minus one standard deviation in that bin.

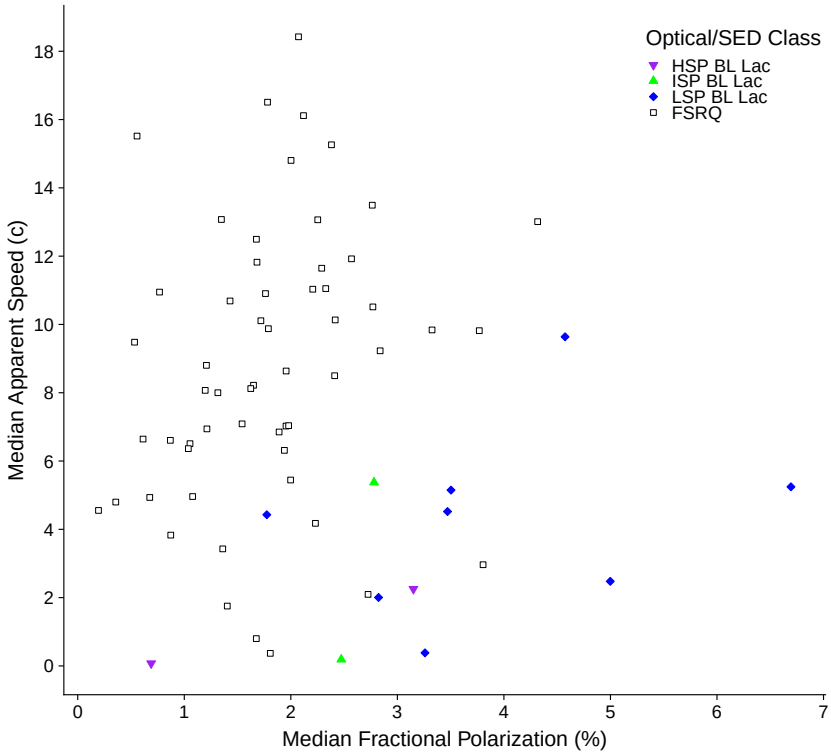

Figure 4.6. Median core fractional polarization $m_{\rm med}$ versus median apparent speed $\beta_{\rm med}$ for each AGN. Purple inverted triangles are HSP BL Lacs, green triangles are ISP BL Lacs, blue diamonds are LSP BL Lacs and unfilled squares are FSRQs.

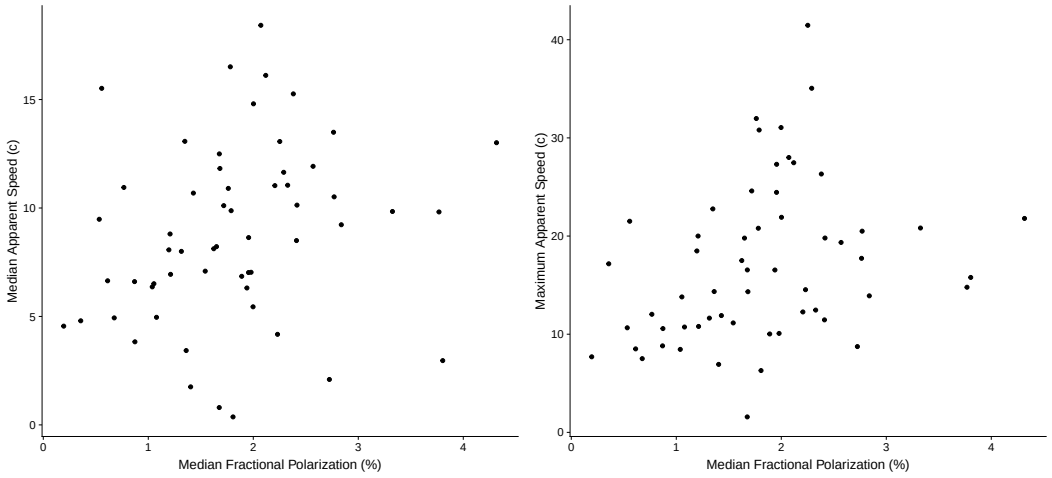

Figure 4.7. Left panel: median core fractional polarization $m_{\rm med}$ versus median apparent speed $\beta_{\rm med}$ for FSRQs with an available median speed, per Section 4.1.1. A Kendall τ test of correlation yields $p = 0.017$ for no correlation. Right panel: median core fractional polarization $m_{\rm med}$ versus median apparent speed $\beta_{\rm med}$ for the same group. A Kendall τ test of correlation yields $p = 0.002$ for no correlation.

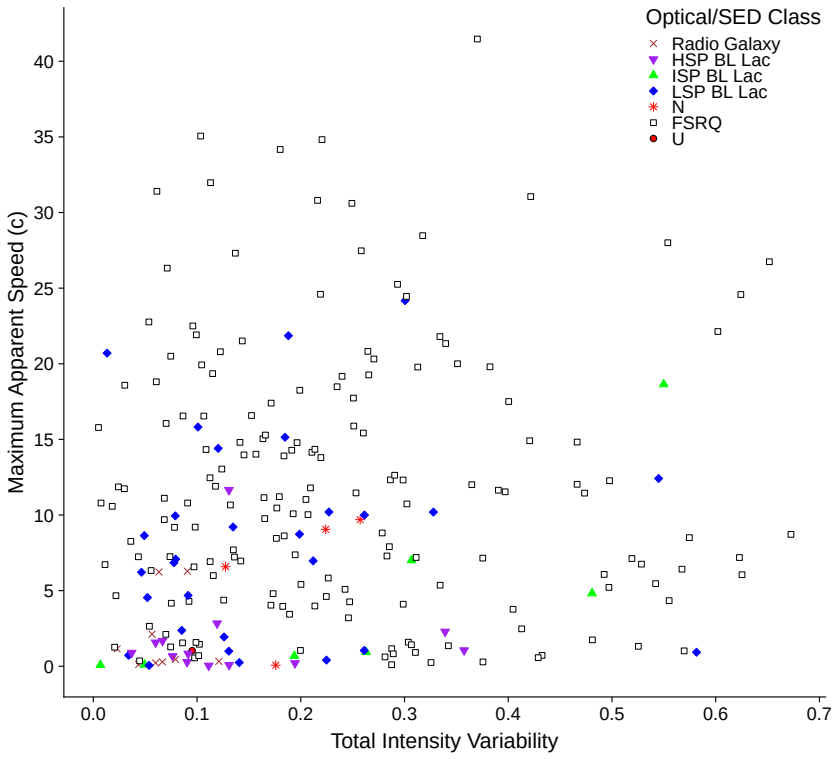

Figure 4.8. Total intensity variability index $I_{\rm var}$ versus maximum apparent speed $\beta_{\rm max}$ for each AGN. Brown crosses are radio galaxies, purple inverted triangles are HSP BL Lacs, green triangles are ISP BL Lacs, blue diamonds are LSP BL Lacs, red stars are NLSy1s, unfilled squares are FSRQs, and red circles have an unknown optical class or synchrotron peak frequency.

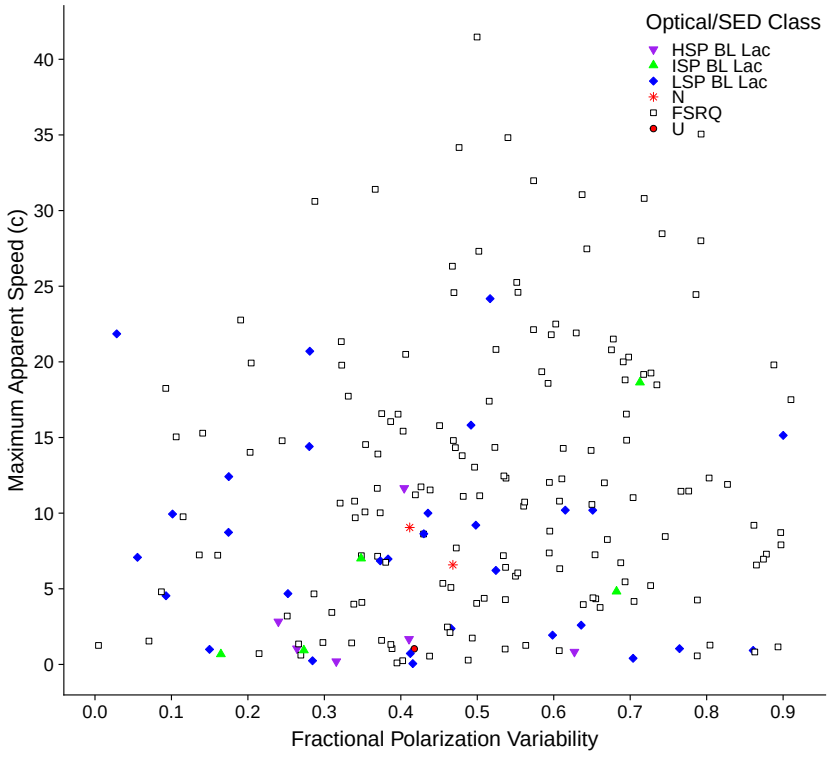

Figure 4.9. Fractional polarization variability index $m_{\rm var}$ versus maximum apparent speed $\beta_{\rm max}$ for each AGN. Purple inverted triangles are HSP BL Lacs, green triangles are ISP BL Lacs, blue diamonds are LSP BL Lacs, red stars are NLSy1s, unfilled squares are FSRQs, and red circles have an unknown optical class or synchrotron peak frequency.

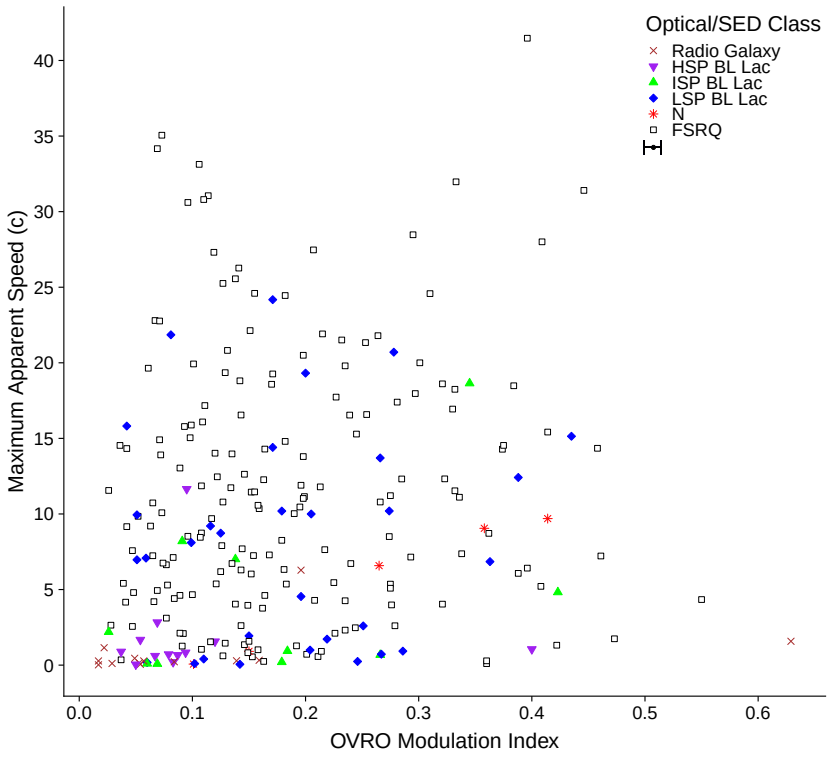

Figure 4.10. Intrinsic 15 GHz OVRO modulation index $\bar{m}$ versus maximum apparent speed $\beta_{\rm max}$ for each AGN. Brown crosses are radio galaxies, purple inverted triangles are HSP BL Lacs, green triangles are ISP BL Lacs, blue diamonds are LSP BL Lacs, red stars are NLSy1s, unfilled squares are FSRQs, and red circles have an unknown optical class or synchrotron peak frequency. The median upper and lower uncertainties for the modulation index are shown under the legend. A Kendall τ test of correlation yields $p = 0.038$ for no correlation.

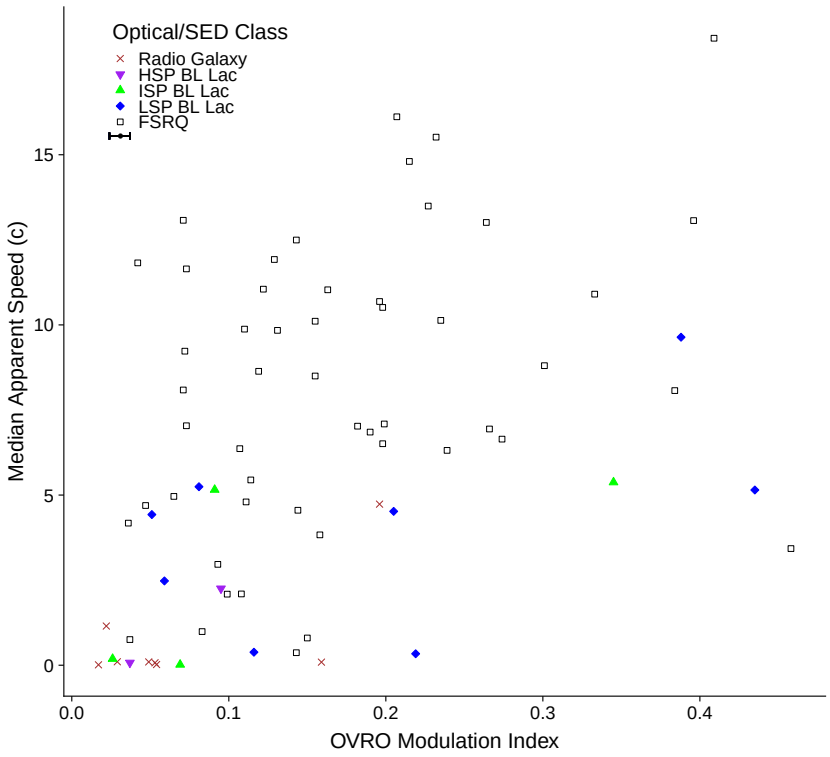

Figure 4.11. Intrinsic modulation index $\bar{m}$ versus median apparent speed $\beta_{\rm med}$ for each AGN. Brown crosses are radio galaxies, purple inverted triangles are HSP BL Lacs, green triangles are ISP BL Lacs, blue diamonds are LSP BL Lacs, red stars are NLSy1s, unfilled squares are FSRQs, and red circles have an unknown optical class or synchrotron peak frequency. The median upper and lower uncertainties for the modulation index are shown under the legend. A Kendall τ test of correlation yields $p = 0.002$ for no correlation.

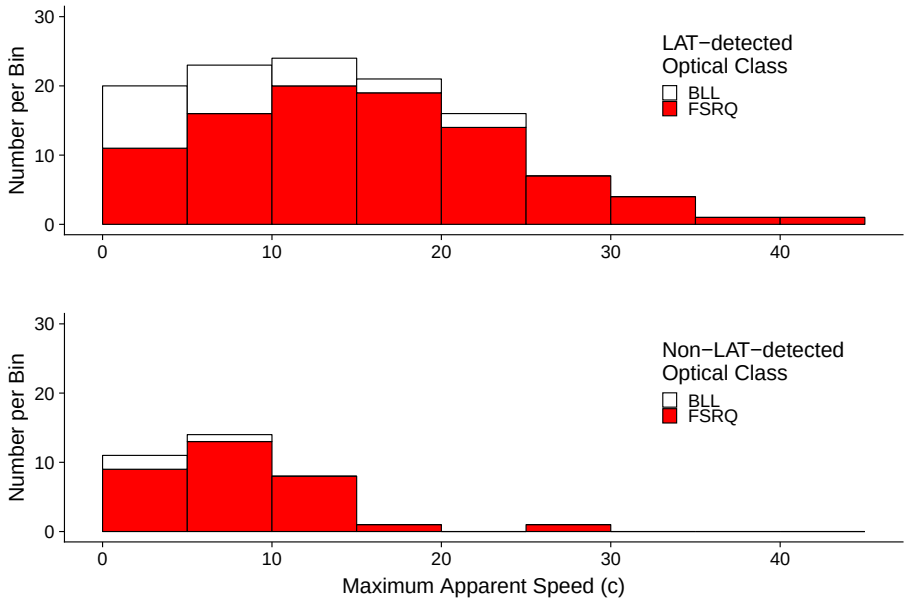

Figure 4.12. Distributions of maximum apparent speed $\beta_{\rm max}$. AGN are grouped as LAT-detected (top) or non-LAT-detected (bottom). Unfilled bins represent all blazars and red bins represent FSRQs.

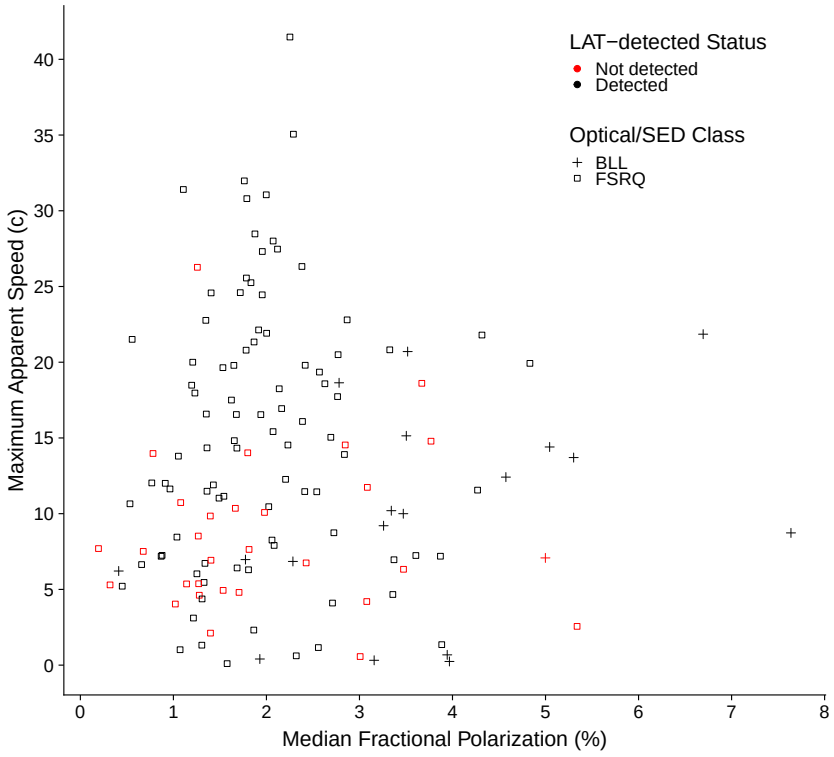

Figure 4.13. Median core fractional polarization $m_{\rm med}$ versus maximum apparent speed $\beta_{\rm max}$. LAT-detected AGN are black and non-LAT-detected AGN are red. BL Lacs of all synchrotron peak frequency classes are represented by crosses, and FSRQs by squares. The non-detected high apparent speed outlier is 2223+210/DA 550.

5. Summary

There is much still unknown about AGN jets; their linear polarization properties offer only indications about how they are formed, powered and collimated to large distances. The primary purpose of this thesis is to investigate these properties, with an emphasis on how they differ across categories of jet, and how they connect to other jet characteristics.

This is done through the use of MOJAVE data taken with the VLBA at 15 GHz. There are few programs currently observing jet polarization, with most of those monitoring at optical wavelengths. In contrast to other work, the conclusions here are based on high-resolution radio images covering a span of ≈15 years. Chapter 2 describes the addition of polarization data, increasing the time and length of coverage for many jets, based on new processing of archival observation epochs. With this data, a large-scale (≈400 sources) statistical study is undertaken to better understand jet behavior at large.

5.1 Goals and Results

5.1.1 Linear Polarization

I show that LSP BL Lacs have higher fractional polarization than FSRQs, and fractional polarization within the BL Lac class is dependent on synchrotron SED peak frequency. Historically results have been mixed regarding the behavior of the EVPA in jets; this work supports a scenario where BL Lacs, regardless of synchrotron SED peak frequency, have EVPAs which are more aligned with the jet and more stable in time compared to FSRQs. Across blazar optical classes, jets which have aligned EVPAs tend to have less variability in their EVPAs and a higher fractional polarization. This

predilection could be interpreted under several of the the currently popular theories, e.g. regarding jet magnetic field structures (Gabuzda, 2003) or shock behavior within the jet Aller et al. 1999 — it can, however, also provide useful constraints for future, more specific theories.

5.1.2 Variability

Blazars are known to be quite variable in flux (Hovatta et al., 2007), but the variability in fractional polarization is less well known, and most literature concerning total intensity is focused on specific source studies. Based on the sample described in this dissertation, HSP BL Lacs have less variability in polarization compared to FSRQs, but this is not true to a statistically significant degree for other SED peak classes of BL Lacs. BL Lacs as a class have less total intensity variability than FSRQs. Jets with high EVPA-jet PA alignment have lower variability in fractional polarization. These results support the possibility that the same processes leading to high EVPA-jet PA alignment also lead to higher, more constant fractional polarization and more stability in the EVPA.

5.1.3 Jet Speeds

One of the difficulties in studying AGN jets is determining the degree to which certain properties are affected by typically unknown relativistic beaming factors. I investigate this issue, first by comparing statistics across *Fermi*-LAT detected and non-detected groupings, and then by using apparent speed measurements as an estimate of the level of relativistic beaming in the jet population.

Unlike previous findings, the only significant difference between γ-detected and non-γ detected populations is their variability in EVPA. However, the fastest jets — and the ones most likely to be detected by *Fermi* — show no preference in the level of EVPA stability. There is some evidence of correlation between higher apparent speeds and greater fractional polarization. Based on these findings, it is likely that

the separation between the HSP and LSP BL Lacs properties can be attributed to differing beaming factors, while the BL Lac/FSRQ divide appears to be due to inherent differences.

5.2 Potential Future Work

5.2.1 Sample Additions

A benefit of this sample is its size — 387 sources, including 5 NLSy1s and 21 HSP BL Lacs. Findings here and in the literature show that HSP BL Lacs have distinct properties from the LSP BL Lac majority. Considering a larger sample of HSP AGN jets may provide more information or confirm some of the milder trends discussed here, such as regarding the variability of different SED peak classes, or the link between fractional polarization and apparent jet speed.

The NLSy1s also show interesting characteristics — while they are thought to be most related to FSRQs, the fractional polarization of the limited number studied here is quite low even for FSRQs. Their EVPA-jet PA alignment, EVPA stability, and similar characteristics are also somewhat extreme, but not odd for a FSRQ of similarily low polarization. Studying a larger number of NLSy1 sources would clarify whether these values are typical for the class or simply a product of small sample size.

5.2.2 Fermi 4FGL Comparisons

Doppler beaming and synchotron SED peak location are thought to be the main motivators of whether a jet is detected at γ-ray energies (Lister et al., 2015), but the full relationship is still unclear. Blazars in this work are listed as detected or not detected based on the *Fermi*-LAT Third Source Catalog (3FGL). As of this writing, the *Fermi*-LAT Fourth Source Catalog (4FGL, The Fermi-LAT collaboration 2019) is in a preliminary stage, but contains several of the AGN which were undetected in

the 3FGL (e.g., the mentioned outlier in Figure 4.13). This lessens the already small group of non-detected radio bright blazars. However, replacing the Boolean detection status with *Fermi* measured median or time-averaged flux is a more informational alternative which could confirm and expand on the results presented here.

REFERENCES

Abdo, A. A., Ackermann, M., Ajello, M., Allafort, A., Antolini, E., Atwood, W. B., Axelsson, M., Baldini, L., Ballet, J., Barbiellini, G., and et al.: 2010a, ApJS **188**, 405

Abdo, A. A., Ackermann, M., Ajello, M., Atwood, W. B., Axelsson, M., Baldini, L., Ballet, J., Barbiellini, G., Bastieri, D., Baughman, B. M., Bechtol, K., Bellazzini, R., Blandford, R. D., Bloom, E. D., Bonamente, E., Borgland, A. W., Bouvier, A., Bregeon, J., Brez, A., Brigida, M., Bruel, P., Burnett, T. H., Caliandro, G. A., Cameron, R. A., Caraveo, P. A., Casandjian, J. M., Cavazzuti, E., Cecchi, C., Charles, E., Chekhtman, A., Chen, A. W., Cheung, C. C., Chiang, J., Ciprini, S., Claus, R., Cohen-Tanugi, J., Colafrancesco, S., Collmar, W., Cominsky, L. R., Conrad, J., Costamante, L., Cutini, S., Dermer, C. D., de Angelis, A., de Palma, F., Digel, S. W., do Couto e Silva, E., Drell, P. S., Dubois, R., Dumora, D., Farnier, C., Favuzzi, C., Fegan, S. J., Ferrara, E. C., Finke, J., Focke, W. B., Foschini, L., Frailis, M., Fuhrmann, L., Fukazawa, Y., Funk, S., Fusco, P., Gargano, F., Gasparrini, D., Gehrels, N., Germani, S., Giebels, B., Giglietto, N., Giommi, P., Giordano, F., Giroletti, M., Glanzman, T., Godfrey, G., Grenier, I. A., Grondin, M.-H., Grove, J. E., Guillemot, L., Guiriec, S., Hanabata, Y., Harding, A. K., Hartman, R. C., Hayashida, M., Hays, E., Healey, S. E., Horan, D., Hughes, R. E., Jóhannesson, G., Johnson, A. S., Johnson, R. P., Johnson, T. J., Johnson, W. N., Kadler, M., Kamae, T., Katagiri, H., Kataoka, J., Kerr, M., Knödlseder, J., Kocian, M. L., Kuehn, F., Kuss, M., Lande, J., Latronico, L., Lemoine-Goumard, M., Longo, F., Loparco, F., Lott, B., Lovellette, M. N., Lubrano, P., Madejski, G. M., Makeev, A., Massaro, E., Mazziotta, M. N., McConville, W., McEnery, J. E., McGlynn, S., Meurer, C., Michelson, P. F., Mitthumsiri, W., Mizuno, T., Moiseev, A. A., Monte, C., Monzani, M. E., Moretti, E., Morselli, A., Moskalenko, I. V., Murgia, S., Nolan, P. L., Norris, J. P., Nuss, E., Ohsugi, T., Omodei, N., Orlando, E., Ormes, J. F., Ozaki, M., Paneque, D., Panetta, J. H., Parent, D., Pelassa, V., Pepe, M., Pesce-Rollins, M., Piron, F., Porter, T. A., Rainò, S., Rando, R., Razzano, M., Razzaque, S., Reimer, A., Reimer, O., Reposeur, T., Reyes, L. C., Ritz, S., Rochester, L. S., Rodriguez, A. Y., Romani, R. W., Ryde, F., Sadrozinski, H. F.-W., Sanchez, D., Sander, A., Saz Parkinson, P. M., Scargle, J. D., Schalk, T. L., Sellerholm, A., Sgrò, C., Shaw, M. S., Smith, D. A., Smith, P. D., Spandre, G., Spinelli, P., Starck, J.-L., Strickman, M. S., Suson, D. J., Tajima, H., Takahashi, H., Takahashi, T., Tanaka, T., Taylor, G. B., Thayer, J. B., Thayer, J. G., Thompson, D. J., Tibaldo, L., Torres, D. F., Tosti, G., Tramacere, A., Uchiyama, Y., Usher, T. L., Vilchez, N., Villata, M., Vitale, V., Waite, A. P., Winer, B. L., Wood, K. S., Ylinen, T., and Ziegler, M.: 2009, ApJ **700**, 597

Abdo, A. A., Ackermann, M., Ajello, M., Axelsson, M., Baldini, L., Ballet, J., Barbiellini, G., Bastieri, D., Baughman, B. M., Bechtol, K., and et al.: 2010b, Nature **463**, 919

Acero, F., Ackermann, M., Ajello, M., Albert, A., Atwood, W. B., Axelsson, M., Baldini, L., Ballet, J., Barbiellini, G., Bastieri, D., Belfiore, A., Bellazzini, R., Bissaldi, E., Blandford, R. D., Bloom, E. D., Bogart, J. R., Bonino, R., Bottacini, E., Bregeon, J., Britto, R. J., Bruel, P., Buehler, R., Burnett, T. H., Buson, S., Caliandro, G. A., Cameron, R. A., Caputo, R., Caragiulo, M., Caraveo, P. A., Casandjian, J. M., Cavazzuti, E., Charles, E., Chaves, R. C. G., Chekhtman, A., Cheung, C. C., Chiang, J., Chiaro, G., Ciprini, S., Claus, R., Cohen-Tanugi, J., Cominsky, L. R., Conrad, J., Cutini, S., D'Ammando, F., de Angelis, A., DeKlotz, M., de Palma, F., Desiante, R., Digel, S. W., Di Venere, L., Drell, P. S., Dubois, R., Dumora, D., Favuzzi, C., Fegan, S. J., Ferrara, E. C., Finke, J., Franckowiak, A., Fukazawa, Y., Funk, S., Fusco, P., Gargano, F., Gasparrini, D., Giebels, B., Giglietto, N., Giommi, P., Giordano, F., Giroletti, M., Glanzman, T., Godfrey, G., Grenier, I. A., Grondin, M.-H., Grove, J. E., Guillemot, L., Guiriec, S., Hadasch, D., Harding, A. K., Hays, E., Hewitt, J. W., Hill, A. B., Horan, D., Iafrate, G., Jogler, T., Jóhannesson, G., Johnson, R. P., Johnson, A. S., Johnson, T. J., Johnson, W. N., Kamae, T., Kataoka, J., Katsuta, J., Kuss, M., La Mura, G., Landriu, D., Larsson, S., Latronico, L., Lemoine-Goumard, M., Li, J., Li, L., Longo, F., Loparco, F., Lott, B., Lovellette, M. N., Lubrano, P., Madejski, G. M., Massaro, F., Mayer, M., Mazziotta, M. N., McEnery, J. E., Michelson, P. F., Mirabal, N., Mizuno, T., Moiseev, A. A., Mongelli, M., Monzani, M. E., Morselli, A., Moskalenko, I. V., Murgia, S., Nuss, E., Ohno, M., Ohsugi, T., Omodei, N., Orienti, M., Orlando, E., Ormes, J. F., Paneque, D., Panetta, J. H., Perkins, J. S., Pesce-Rollins, M., Piron, F., Pivato, G., Porter, T. A., Racusin, J. L., Rando, R., Razzano, M., Razzaque, S., Reimer, A., Reimer, O., Reposeur, T., Rochester, L. S., Romani, R. W., Salvetti, D., Sánchez-Conde, M., Saz Parkinson, P. M., Schulz, A., Siskind, E. J., Smith, D. A., Spada, F., Spandre, G., Spinelli, P., Stephens, T. E., Strong, A. W., Suson, D. J., Takahashi, H., Takahashi, T., Tanaka, Y., Thayer, J. G., Thayer, J. B., Thompson, D. J., Tibaldo, L., Tibolla, O., Torres, D. F., Torresi, E., Tosti, G., Troja, E., Van Klaveren, B., Vianello, G., Winer, B. L., Wood, K. S., Wood, M., Zimmer, S., and Fermi-LAT Collaboration: 2015a, ApJS **218**, 23

Acero, F., Ackermann, M., Ajello, M., Albert, A., Atwood, W. B., Axelsson, M., Baldini, L., Ballet, J., Barbiellini, G., Bastieri, D., Belfiore, A., Bellazzini, R., Bissaldi, E., Blandford, R. D., Bloom, E. D., Bogart, J. R., Bonino, R., Bottacini, E., Bregeon, J., Britto, R. J., Bruel, P., Buehler, R., Burnett, T. H., Buson, S., Caliandro, G. A., Cameron, R. A., Caputo, R., Caragiulo, M., Caraveo, P. A., Casandjian, J. M., Cavazzuti, E., Charles, E., Chaves, R. C. G., Chekhtman, A., Cheung, C. C., Chiang, J., Chiaro, G., Ciprini, S., Claus, R., Cohen-Tanugi, J., Cominsky, L. R., Conrad, J., Cutini, S., D'Ammando, F., de Angelis, A., DeKlotz, M., de Palma, F., Desiante, R., Digel, S. W., Di Venere, L., Drell, P. S., Dubois, R., Dumora, D., Favuzzi, C., Fegan, S. J., Ferrara, E. C., Finke, J., Franckowiak, A., Fukazawa, Y., Funk, S., Fusco, P., Gargano, F., Gasparrini, D., Giebels, B., Giglietto, N., Giommi, P., Giordano, F., Giroletti, M., Glanzman, T., Godfrey, G., Grenier, I. A., Grondin, M. H., Grove, J. E., Guillemot, L., Guiriec, S., Hadasch, D., Harding, A. K., Hays, E., Hewitt, J. W., Hill, A. B., Horan, D., Iafrate, G., Jogler, T., Jóhannesson, G., Johnson, R. P., Johnson, A. S., Johnson, T. J., Johnson, W. N., Kamae, T., Kataoka, J., Katsuta, J., Kuss, M., La Mura, G., Landriu, D., Larsson, S., Latronico, L., Lemoine-Goumard, M., Li, J., Li, L., Longo, F., Loparco, F., Lott, B., Lovellette, M. N., Lubrano, P., Madejski, G. M., Massaro, F., Mayer, M., Mazziotta, M. N., McEnery, J. E., Michelson, P. F., Mirabal, N., Mizuno, T., Moiseev, A. A., Mongelli, M., Monzani, M. E., Morselli, A., Moskalenko, I. V., Murgia, S., Nuss, E., Ohno, M., Ohsugi, T., Omodei, N., Orienti, M., Orlando, E., Ormes, J. F., Paneque, D., Panetta, J. H., Perkins, J. S., Pesce-Rollins, M., Piron, F., Pivato, G., Porter,

T. A., Racusin, J. L., Rando, R., Razzano, M., Razzaque, S., Reimer, A., Reimer, O., Reposeur, T., Rochester, L. S., Romani, R. W., Salvetti, D., Sánchez-Conde, M., Saz Parkinson, P. M., Schulz, A., Siskind, E. J., Smith, D. A., Spada, F., Spandre, G., Spinelli, P., Stephens, T. E., Strong, A. W., Suson, D. J., Takahashi, H., Takahashi, T., Tanaka, Y., Thayer, J. G., Thayer, J. B., Thompson, D. J., Tibaldo, L., Tibolla, O., Torres, D. F., Torresi, E., Tosti, G., Troja, E., Van Klaveren, B., Vianello, G., Winer, B. L., Wood, K. S., Wood, M., Zimmer, S., and Fermi-LAT Collaboration: 2015b, *The Astrophysical Journal Supplement Series* 218

Ackermann, M., Ajello, M., Allafort, A., Antolini, E., Atwood, W. B., Axelsson, M., Baldini, L., Ballet, J., Barbiellini, G., Bastieri, D., Bechtol, K., Bellazzini, R., Berenji, B., Blandford, R. D., Bloom, E. D., Bonamente, E., Borgland, A. W., Bottacini, E., Bouvier, A., Bregeon, J., Brigida, M., Bruel, P., Buehler, R., Burnett, T. H., Buson, S., Caliandro, G. A., Cameron, R. A., Caraveo, P. A., Casandjian, J. M., Cavazzuti, E., Cecchi, C., Charles, E., Cheung, C. C., Chiang, J., Ciprini, S., Claus, R., Cohen-Tanugi, J., Conrad, J., Costamante, L., Cutini, S., de Angelis, A., de Palma, F., Dermer, C. D., Digel, S. W., Silva, E. d. C. e., Drell, P. S., Dubois, R., Escande, L., Favuzzi, C., Fegan, S. J., Ferrara, E. C., Finke, J., Focke, W. B., Fortin, P., Frailis, M., Fukazawa, Y., Funk, S., Fusco, P., Gargano, F., Gasparrini, D., Gehrels, N., Germani, S., Giebels, B., Giglietto, N., Giommi, P., Giordano, F., Giroletti, M., Glanzman, T., Godfrey, G., Grenier, I. A., Grove, J. E., Guiriec, S., Gustafsson, M., Hadasch, D., Hayashida, M., Hays, E., Healey, S. E., Horan, D., Hou, X., Hughes, R. E., Iafrate, G., Jóhannesson, G., Johnson, A. S., Johnson, W. N., Kamae, T., Katagiri, H., Kataoka, J., Knödlseder, J., Kuss, M., Lande, J., Larsson, S., Latronico, L., Longo, F., Loparco, F., Lott, B., Lovellette, M. N., Lubrano, P., Madejski, G. M., Mazziotta, M. N., McConville, W., McEnery, J. E., Michelson, P. F., Mitthumsiri, W., Mizuno, T., Moiseev, A. A., Monte, C., Monzani, M. E., Moretti, E., Morselli, A., Moskalenko, I. V., Murgia, S., Nakamori, T., Naumann-Godo, M., Nolan, P. L., Norris, J. P., Nuss, E., Ohno, M., Ohsugi, T., Okumura, A., Omodei, N., Orienti, M., Orlando, E., Ormes, J. F., Ozaki, M., Paneque, D., Parent, D., Pesce-Rollins, M., Pierbattista, M., Piranomonte, S., Piron, F., Pivato, G., Porter, T. A., Rainò, S., Rando, R., Razzano, M., Razzaque, S., Reimer, A., Reimer, O., Ritz, S., Rochester, L. S., Romani, R. W., Roth, M., Sanchez, D. A., Sbarra, C., Scargle, J. D., Schalk, T. L., Sgrò, C., Shaw, M. S., Siskind, E. J., Spandre, G., Spinelli, P., Strong, A. W., Suson, D. J., Tajima, H., Takahashi, H., Takahashi, T., Tanaka, T., Thayer, J. G., Thayer, J. B., Thompson, D. J., Tibaldo, L., Tinivella, M., Torres, D. F., Tosti, G., Troja, E., Uchiyama, Y., Vandenbroucke, J., Vasileiou, V., Vianello, G., Vitale, V., Waite, A. P., Wallace, E., Wang, P., Winer, B. L., Wood, D. L., Wood, K. S., and Zimmer, S.: 2011, ApJ **743**, 171

Ackermann, M., Ajello, M., Atwood, W. B., Baldini, L., Ballet, J., Barbiellini, G., Bastieri, D., Becerra Gonzalez, J., Bellazzini, R., Bissaldi, E., Blandford, R. D., Bloom, E. D., Bonino, R., Bottacini, E., Brandt, T. J., Bregeon, J., Britto, R. J., Bruel, P., Buehler, R., Buson, S., Caliandro, G. A., Cameron, R. A., Caragiulo, M., Caraveo, P. A., Carpenter, B., Casandjian, J. M., Cavazzuti, E., Cecchi, C., Charles, E., Chekhtman, A., Cheung, C. C., Chiang, J., Chiaro, G., Ciprini, S., Claus, R., Cohen- Tanugi, J., Cominsky, L. R., Conrad, J., Cutini, S., D'Abrusco, R., D'Ammando, F., de Angelis, A., Desiante, R., Digel, S. W., Di Venere, L., Drell, P. S., Favuzzi, C., Fegan, S. J., Ferrara, E. C., Finke, J., Focke, W. B., Franckowiak, A., Fuhrmann, L., Fukazawa, Y., Furniss, A. K., Fusco, P., Gargano, F., Gasparrini, D., Giglietto, N., Giommi, P., Giordano, F., Giroletti, M., Glanzman, T., Godfrey, G., Grenier, I. A., Grove, J. E., Guiriec, S., Hewitt, J. W., Hill, A. B., Horan, D.,

Itoh, R., Jóhannesson, G., Johnson, A. S., Johnson, W. N., Kataoka, J., Kawano, T., Krauss, F., Kuss, M., La Mura, G., Larsson, S., Latronico, L., Leto, C., Li, J., Li, L., Longo, F., Loparco, F., Lott, B., Lovellette, M. N., Lubrano, P., Madejski, G. M., Mayer, M., Mazziotta, M. N., McEnery, J. E., Michelson, P. F., Mizuno, T., Moiseev, A. A., Monzani, M. E., Morselli, A., Moskalenko, I. V., Murgia, S., Nuss, E., Ohno, M., Ohsugi, T., Ojha, R., Omodei, N., Orienti, M., Orlando, E., Paggi, A., Paneque, D., Perkins, J. S., Pesce-Rollins, M., Piron, F., Pivato, G., Porter, T. A., Rainò, S., Rando, R., Razzano, M., Razzaque, S., Reimer, A., Reimer, O., Romani, R. W., Salvetti, D., Schaal, M., Schinzel, F. K., Schulz, A., Sgrò, C., Siskind, E. J., Sokolovsky, K. V., Spada, F., Spandre, G., Spinelli, P., Stawarz, L., Suson, D. J., Takahashi, H., Takahashi, T., Tanaka, Y., Thayer, J. G., Thayer, J. B., Tibaldo, L., Torres, D. F., Torresi, E., Tosti, G., Troja, E., Uchiyama, Y., Vianello, G., Winer, B. L., Wood, K. S., and Zimmer, S.: 2015, ApJ 810

Agudo, I.: 2009, in Y. Hagiwara, E. Fomalont, M. Tsuboi, and M. Yasuhiro (eds.), *Approaching Micro-Arcsecond Resolution with VSOP-2: Astrophysics and Technologies*, Vol. 402 of *Astronomical Society of the Pacific Conference Series*, p. 330

Agudo, I., Bach, U., Krichbaum, T. P., Marscher, A. P., Gonidakis, I., Diamond, P. J., Perucho, M., Alef, W., Graham, D. A., Witzel, A., Zensus, J. A., Bremer, M., Acosta-Pulido, J. A., and Barrena, R.: 2007, A&A **476**, L17

Agudo, I., Thum, C., Gómez, J. L., and Wiesemeyer, H.: 2014, A&A **566**, A59

Agudo, I., Thum, C., Ramakrishnan, V., Molina, S. N., Casadio, C., and Gómez, J. L.: 2018, MNRAS **473**, 1850

Albareti, F. D., Allende Prieto, C., Almeida, A., Anders, F., Anderson, S., Andrews, B. H., Aragón-Salamanca, A., Argudo-Fernández, M., Armengaud, E., Aubourg, E., and et al.: 2017, ApJS **233**, 25

Aller, M., Hughes, P., Aller, H., Hovatta, T., and Ramakrishnan, V.: 2016, *Galaxies* **4**, 35

Aller, M. F., Aller, H. D., and Hughes, P. A.: 2003, ApJ **586**, 33

Aller, M. F., Aller, H. D., Hughes, P. A., and Latimer, G. E.: 1999, ApJ **512**, 601

Aller, M. F., Hughes, P. A., Aller, H. D., Latimer, G. E., and Hovatta, T.: 2014, ApJ **791**, 53

Angelakis, E., Hovatta, T., Blinov, D., Pavlidou, V., Kiehlmann, S., Myserlis, I., Böttcher, M., Mao, P., Panopoulou, G. V., Liodakis, I., King, O. G., Baloković, M., Kus, A., Kylafis, N., Mahabal, A., Marecki, A., Paleologou, E., Papadakis, I., Papamastorakis, I., Pazderski, E., Pearson, T. J., Prabhudesai, S., Ramaprakash, A. N., Readhead, A. C. S., Reig, P., Tassis, K., Urry, M., and Zensus, J. A.: 2016, MNRAS **463**, 3365

Asada, K., Inoue, M., Uchida, Y., Kameno, S., Fujisawa, K., Iguchi, S., and Mutoh, M.: 2002, PASJ **54**, L39

Bagchi, J., Vivek, M., Vikram, V., Hota, A., Biju, K. G., Sirothia, S. K., Srianand, R., Gopal-Krishna, and Jacob, J.: 2014, ApJ **788**, 174

Bennett, A. S.: 1962, MNRAS **125**, 75

Bicknell, G. V., de Ruiter, H. R., Parma, P., Morganti, R., and Fanti, R.: 1990, ApJ **354**, 98

Blandford, R. D. and Payne, D. G.: 1982, MNRAS **199**, 883

Blandford, R. D. and Znajek, R. L.: 1977, MNRAS **179**, 433

Blinov, D., Pavlidou, V., Papadakis, I., Kiehlmann, S., Liodakis, I., Panopoulou, G. V., Angelakis, E., Baloković, M., Hovatta, T., King, O. G., Kus, A., Kylafis, N., Mahabal, A., Maharana, S., Myserlis, I., Paleologou, E., Papamastorakis, I., Pazderski, E., Pearson, T. J., Ramaprakash, A., Readhead, A. C. S., Reig, P., Tassis, K., and Zensus, J. A.: 2018, MNRAS **474**, 1296

Bloom, S. D. and Marscher, A. P.: 1996, ApJ **461**, 657

Burn, B. J.: 1966, MNRAS **133**, 67

Cawthorne, T. V., Wardle, J. F. C., Roberts, D. H., and Gabuzda, D. C.: 1993, ApJ **416**, 519

Clark, B. G.: 1999, in *Synthesis Imaging in Radio Astronomy II*, Vol. 180, p. 1

Cohen, M. H., Aller, H. D., Aller, M. F., Hovatta, T., Kharb, P., Kovalev, Y. Y., Lister, M. L., Meier, D. L., Pushkarev, A. B., and Savolainen, T.: 2018, *Reversals in the Direction of Polarization Rotation in OJ 287*, accepted ApJ

Cohen, M. H., Lister, M. L., Homan, D. C., Kadler, M., Kellermann, K. I., Kovalev, Y. Y., and Vermeulen, R. C.: 2007, ApJ **658**, 232

Conselice, C. J., Wilkinson, A., Duncan, K., and Mortlock, A.: 2016, ApJ **830**, 83

Cornwell, T., Braun, R., and Briggs, D. S.: 1999, in *Synthesis Imaging in Radio Astronomy II*, Vol. 180, p. 151

Cotton, W. D.: 1999, in G. B. Taylor, C. L. Carilli, and R. A. Perley (eds.), *Synthesis Imaging in Radio Astronomy II*, Vol. 180 of *Astronomical Society of the Pacific Conference Series*, p. 111

Fanaroff, B. L. and Riley, J. M.: 1974, MNRAS **167**, 31P

Foschini, L.: 2017, *Frontiers in Astronomy and Space Sciences* **4**, 6

Fossati, G., Maraschi, L., Celotti, A., Comastri, A., and Ghisellini, G.: 1998, MNRAS **299**, 433

Gabuzda, D. C.: 2003, New A Rev. **47**, 599

Gabuzda, D. C.: 2015, in I. Contopoulos, D. Gabuzda, and N. Kylafis (eds.), *The Formation and Disruption of Black Hole Jets*, Vol. 414 of *Astrophysics and Space Science Library*, p. 117

Gabuzda, D. C., Murray, É., and Cronin, P.: 2004, MNRAS **351**, L89

Gabuzda, D. C., Pushkarev, A. B., and Cawthorne, T. V.: 2000, MNRAS **319**, 1109

Ghisellini, G.: 2016, *Galaxies* **4**, 36

Ghisellini, G., Celotti, A., Fossati, G., Maraschi, L., and Comastri, A.: 1998, MNRAS **301**, 451

Ghisellini, G., Tavecchio, F., Foschini, L., and Ghirlanda, G.: 2011, MNRAS **414**, 2674

Gómez, J. L., Lobanov, A. P., Bruni, G., Kovalev, Y. Y., Marscher, A. P., Jorstad, S. G., Mizuno, Y., Bach, U., Sokolovsky, K. V., Anderson, J. M., Galindo, P., Kardashev, N. S., and Lisakov, M. M.: 2016, ApJ **817**, 96

Gomez, J. L., Marscher, A. P., Alberdi, A., Jorstad, S. G., and Agudo, I.: 2002, in *VLBA Scientific Memos*, Vol. 30

Hartman, R. C., Bertsch, D. L., Bloom, S. D., Chen, A. W., Deines-Jones, P., Esposito, J. A., Fichtel, C. E., Friedlander, D. P., Hunter, S. D., McDonald, L. M., Sreekumar, P., Thompson, D. J., Jones, B. B., Lin, Y. C., Michelson, P. F., Nolan, P. L., Tompkins, W. F., Kanbach, G., Mayer-Hasselwander, H. A., Mücke, A., Pohl, M., Reimer, O., Kniffen, D. A., Schneid, E. J., von Montigny, C., Mukherjee, R., and Dingus, B. L.: 1999, ApJS **123**, 79

Helmboldt, J. F., Taylor, G. B., Tremblay, S., Fassnacht, C. D., Walker, R. C., Myers, S. T., Sjouwerman, L. O., Pearson, T. J., Readhead, A. C. S., Weintraub, L., Gehrels, N., Romani, R. W., Healey, S., Michelson, P. F., Blandford, R. D., and Cotter, G.: 2007, ApJ **658**, 203

Hodge, M. A., Lister, M. L., Aller, M. F., Aller, H. D., Kovalev, Y. Y., Pushkarev, A. B., and Savolainen, T.: 2018, ApJ **862**, 151

Högbom, J. A.: 1974, A&AS **15**, 417

Hogg, D. W.: 1999, *ArXiv Astrophysics e-prints*

Homan, D. C., Kadler, M., Kellermann, K. I., Kovalev, Y. Y., Lister, M. L., Ros, E., Savolainen, T., and Zensus, J. A.: 2009, ApJ **706**, 1253

Homan, D. C., Lister, M. L., Kovalev, Y. Y., Pushkarev, A. B., Savolainen, T., Kellermann, K. I., Richards, J. L., and Ros, E.: 2015, ApJ **798**, 134

Hovatta, T., Lister, M. L., Aller, M. F., Aller, H. D., Homan, D. C., Kovalev, Y. Y., Pushkarev, A. B., and Savolainen, T.: 2012, AJ **144**, 105

Hovatta, T., Lister, M. L., Kovalev, Y. Y., Pushkarev, A. B., and Savolainen, T.: 2010, *IJMP D* **19**, 943

Hovatta, T., Tornikoski, M., Lainela, M., Lehto, H. J., Valtaoja, E., Torniainen, I., Aller, M. F., and Aller, H. D.: 2007, A&A **469**, 899

Hovatta, T., Valtaoja, E., Tornikoski, M., and Lähteenmäki, A.: 2009, A&A **494**, 527

Jones, D. H., Saunders, W., Read, M., and Colless, M.: 2005, PASA **22**, 277

Jorstad, S. G., Marscher, A. P., Mattox, J. R., Aller, M. F., Aller, H. D., Wehrle, A. E., and Bloom, S. D.: 2001, ApJ **556**, 738

Jorstad, S. G., Marscher, A. P., Morozova, D. A., Troitsky, I. S., Agudo, I., Casadio, C., Foord, A., Gómez, J. L., MacDonald, N. R., Molina, S. N., Lähteenmäki, A., Tammi, J., and Tornikoski, M.: 2017, ApJ **846**, 98

Jorstad, S. G., Marscher, A. P., Stevens, J. A., Smith, P. S., Forster, J. R., Gear, W. K., Cawthorne, T. V., Lister, M. L., Stirling, A. M., Gómez, J. L., Greaves, J. S., and Robson, E. I.: 2007, AJ **134**, 799

Kellermann, K. I., Lister, M. L., Homan, D. C., Vermeulen, R. C., Cohen, M. H., Ros, E., Kadler, M., Zensus, J. A., and Kovalev, Y. Y.: 2004, ApJ **609**, 539

Kellermann, K. I., Sramek, R., Schmidt, M., Shaffer, D. B., and Green, R.: 1989, AJ **98**, 1195

Kellermann, K. I., Vermeulen, R. C., Zensus, J. A., and Cohen, M. H.: 1998, AJ **115**, 1295

Kharb, P., Lister, M. L., and Cooper, N. J.: 2010, ApJ **710**, 764

Kiehlmann, S., Savolainen, T., Jorstad, S. G., Sokolovsky, K. V., Schinzel, F. K., Marscher, A. P., Larionov, V. M., Agudo, I., Akitaya, H., Benítez, E., Berdyugin, A., Blinov, D. A., Bochkarev, N. G., Borman, G. A., Burenkov, A. N., Casadio, C., Doroshenko, V. T., Efimova, N. V., Fukazawa, Y., Gómez, J. L., Grishina, T. S., Hagen-Thorn, V. A., Heidt, J., Hiriart, D., Itoh, R., Joshi, M., Kawabata, K. S., Kimeridze, G. N., Kopatskaya, E. N., Korobtsev, I. V., Krajci, T., Kurtanidze, O. M., Kurtanidze, S. O., Larionova, E. G., Larionova, L. V., Lindfors, E., López, J. M., McHardy, I. M., Molina, S. N., Moritani, Y., Morozova, D. A., Nazarov, S. V., Nikolashvili, M. G., Nilsson, K., Pulatova, N. G., Reinthal, R., Sadun, A., Sasada, M., Savchenko, S. S., Sergeev, S. G., Sigua, L. A., Smith, P. S., Sorcia, M., Spiridonova, O. I., Takaki, K., Takalo, L. O., Taylor, B., Troitsky, I. S., Uemura, M., Ugolkova, L. S., Ui, T., Yoshida, M., Zensus, J. A., and Zhdanova, V. E.: 2016, A&A **590**, A10

Komatsu, E., Dunkley, J., Nolta, M. R., Bennett, C. L., Gold, B., Hinshaw, G., Jarosik, N., Larson, D., Limon, M., Page, L., Spergel, D. N., Halpern, M., Hill, R. S., Kogut, A., Meyer, S. S., Tucker, G. S., Weiland, J. L., Wollack, E., and Wright, E. L.: 2009, ApJS **180**, 330

Konigl, A.: 1981, ApJ **243**, 700

Lawrence, C. R., Pearson, T. J., Readhead, A. C. S., and Unwin, S. C.: 1986, AJ **91**, 494

Lee, L.: 2017, *NADA: Nondetects and Data Analysis for Environmental Data*, R package version 1.6-1

Linford, J. D., Taylor, G. B., Romani, R. W., Helmboldt, J. F., Readhead, A. C. S., Reeves, R., and Richards, J. L.: 2012a, ApJ **744**, 177

Linford, J. D., Taylor, G. B., and Schinzel, F. K.: 2012b, ApJ **757**, 25

Liodakis, I., Hovatta, T., Huppenkothen, D., Kiehlmann, S., Max-Moerbeck, W., and Readhead, A. C. S.: 2018, ApJ **866**, 137

Lister, M.: 2018, in *Revisiting narrow-line Seyfert 1 galaxies and their place in the Universe. 9-13 April 2018. Padova Botanical Garden*, p. 22

Lister, M. L., Aller, M., Aller, H., Hovatta, T., Kellermann, K. I., Kovalev, Y. Y., Meyer, E. T., Pushkarev, A. B., Ros, E., MOJAVE Collaboration, Ackermann, M., Antolini, E., Baldini, L., Ballet, J., Barbiellini, G., Bastieri, D., Bechtol, K., Bellazzini, R., Berenji, B., Blandford, R. D., Bloom, E. D., Boeck, M., Bonamente, E., Borgland, A. W., Bregeon, J., Brigida, M., Bruel, P., Buehler, R., Buson, S., Caliandro, G. A., Cameron, R. A., Caraveo, P. A., Casandjian, J. M., Cavazzuti, E., Cecchi, C., Chang, C. S., Charles, E., Chekhtman, A., Cheung, C. C., Chiang, J., Ciprini, S., Claus, R., Cohen-Tanugi, J., Conrad, J., Cutini, S., de Palma, F., Dermer, C. D., Silva, E. d. C. e., Drell, P. S., Drlica-Wagner, A., Favuzzi, C., Fegan, S. J., Ferrara, E. C., Finke, J., Focke, W. B., Fortin, P., Fukazawa, Y., Fusco, P., Gargano, F., Gasparrini, D., Gehrels, N., Germani, S., Giglietto, N., Giordano, F., Giroletti, M., Glanzman, T., Godfrey, G., Grenier, I. A., Guiriec, S., Hadasch, D., Hayashida, M., Hays, E., Horan, D., Hughes, R. E., Jóhannesson, G., Johnson, A. S., Kadler, M., Katagiri, H., Kataoka, J., Knödlseder, J., Kuss, M., Lande, J., Longo, F., Loparco, F., Lott, B., Lovellette, M. N., Lubrano, P., Madejski, G. M., Mazziotta, M. N., McConville, W., McEnery, J. E., Mehault, J., Michelson, P. F., Mizuno, T., Monte, C., Monzani, M. E., Morselli, A., Moskalenko, I. V., Murgia, S., Naumann-Godo, M., Nishino, S., Nolan, P. L., Norris, J. P., Nuss, E., Ohno, M., Ohsugi, T., Okumura, A., Omodei, N., Orlando, E., Ozaki, M., Paneque, D., Parent, D., Pesce-Rollins, M., Pierbattista, M., Piron, F., Pivato, G., Rainò, S., Readhead, A., Reimer, A., Reimer, O., Richards, J. L., Ritz, S., Sadrozinski, H. F.-W., Sgrò, C., Shaw, M. S., Siskind, E. J., Spandre, G., Spinelli, P., Takahashi, H., Tanaka, T., Thayer, J. G., Thayer, J. B., Thompson, D. J., Tosti, G., Tramacere, A., Troja, E., Usher, T. L., Vandenbroucke, J., Vasileiou, V., Vianello, G., Vitale, V., Waite, A. P., Wang, P., Winer, B. L., Wood, K. S., Zimmer, S., and Fermi LAT Collaboration: 2011, ApJ **742**, 27

Lister, M. L., Aller, M. F., Aller, H. D., Hodge, M. A., Homan, D. C., Kovalev, Y. Y., Pushkarev, A. B., and Savolainen, T.: 2018, ApJS **234**, 12

Lister, M. L., Aller, M. F., Aller, H. D., Homan, D. C., Kellermann, K. I., Kovalev, Y. Y., Pushkarev, A. B., Richards, J. L., Ros, E., and Savolainen, T.: 2013a, AJ **146**, 120

Lister, M. L., Aller, M. F., Aller, H. D., Homan, D. C., Kellermann, K. I., Kovalev, Y. Y., Pushkarev, A. B., Richards, J. L., Ros, E., and Savolainen, T.: 2013b, AJ **146**, 120

Lister, M. L., Aller, M. F., Aller, H. D., Homan, D. C., Kellermann, K. I., Kovalev, Y. Y., Pushkarev, A. B., Richards, J. L., Ros, E., and Savolainen, T.: 2016a, AJ **152**, 12

Lister, M. L., Aller, M. F., Aller, H. D., Homan, D. C., Kellermann, K. I., Kovalev, Y. Y., Pushkarev, A. B., Richards, J. L., Ros, E., and Savolainen, T.: 2016b, AJ **152**, 12

Lister, M. L., Aller, M. F., Aller, H. D., Hovatta, T., Max-Moerbeck, W., Readhead, A. C. S., Richards, J. L., and Ros, E.: 2015, ApJ **810**, L9

Lister, M. L., Cohen, M. H., Homan, D. C., Kadler, M., Kellermann, K. I., Kovalev, Y. Y., Ros, E., Savolainen, T., and Zensus, J. A.: 2009, AJ **138**, 1874

Lister, M. L. and Homan, D. C.: 2005, AJ **130**, 1389

Lister, M. L., Homan, D. C., Hovatta, T., Kellermann, K. I., Kiehlmann, S., Kovalev, Y. Y., Max-Moerbeck, W., Pushkarev, A. B., Readhead, A. C. S., Ros, E., and Savolainen, T.: 2019, *MOJAVE: XVII. Jet Kinematics and Parent Population Properties of Relativistically Beamed Radio-Loud Blazars*, submitted ApJ

Longair, M. S.: 2011, *High Energy Astrophysics*, Cambridge University Press

Lyutikov, M., Pariev, V. I., and Gabuzda, D. C.: 2005, MNRAS **360**, 869

Mannheim, K.: 1993, A&A **269**, 67

Mannheim, K. and Biermann, P. L.: 1992, A&A **253**, L21

Marcaide, J. M. and Shapiro, I. I.: 1984, ApJ **276**, 56

Marscher, A.: 2016, *Galaxies* **4**, 37

Meyer, M., Scargle, J. D., and Blandford, R. D.: 2019, *arXiv e-prints* p. arXiv:1902.02291

Paliya, V. S., Parker, M. L., Jiang, J., Fabian, A. C., Brenneman, L., Ajello, M., and Hartmann, D.: 2019, *arXiv e-prints*

Pavlidou, V., Angelakis, E., Myserlis, I., Blinov, D., King, O. G., Papadakis, I., Tassis, K., Hovatta, T., Pazderska, B., Paleologou, E., Baloković, M., Feiler, R., Fuhrmann, L., Khodade, P., Kus, A., Kylafis, N., Modi, D., Panopoulou, G., Papamastorakis, I., Pazderski, E., Pearson, T. J., Rajarshi, C., Ramaprakash, A., Readhead, A. C. S., Reig, P., and Zensus, J. A.: 2014, MNRAS **442**, 1693

Pollack, L. K., Taylor, G. B., and Zavala, R. T.: 2003, ApJ **589**, 733

Press, W. H., Teukolsky, S. A., Vetterling, W. T., and Flannery, B. P.: 2002, *Numerical recipes in C++ : the art of scientific computing*, Cambridge University Press

Pushkarev, A. B., Kovalev, Y. Y., Lister, M. L., and Savolainen, T.: 2017, MNRAS **468**, 4992

R Core Team: 2017, *R: A Language and Environment for Statistical Computing*, R Foundation for Statistical Computing, Vienna, Austria

Richards, J. L., Hovatta, T., Max-Moerbeck, W., Pavlidou, V., Pearson, T. J., and Readhead, A. C. S.: 2014, MNRAS **438**, 3058

Richards, J. L., Max-Moerbeck, W., Pavlidou, V., King, O. G., Pearson, T. J., Readhead, A. C. S., Reeves, R., Shepherd, M. C., Stevenson, M. A., Weintraub, L. C., Fuhrmann, L., Angelakis, E., Zensus, J. A., Healey, S. E., Romani, R. W., Shaw, M. S., Grainge, K., Birkinshaw, M., Lancaster, K., Worrall, D. M., Taylor, G. B., Cotter, G., and Bustos, R.: 2011, ApJS **194**, 29

Roberts, D. H., Potash, R. I., Wardle, J. F. C., Rogers, A. E. E., and Burke, B. F.: 1984, in *VLBI and Compact Radio Sources. Symposium no. 110 held in Bologna, Italy, June 27-July 1, 1983. Edited by R. Fanti, K. Kellermann, and G. Setti. p. 35, 1984*, Vol. 110, p. 35

Rybicki, G. B. and Lightman, A. P.: 1979, *Radiative processes in astrophysics*, Wiley-Interscience

Sargent, W. L. W.: 1970, ApJ **160**, 405

Schramm, K.-J., Borgeest, U., Kuehl, D., von Linde, J., Linnert, M. D., and Schramm, T.: 1994, A&AS **106**, 349

Shaw, M. S., Romani, R. W., Cotter, G., Healey, S. E., Michelson, P. F., Readhead, A. C. S., Richards, J. L., Max-Moerbeck, W., King, O. G., and Potter, W. J.: 2012, ApJ **748**, 49

Shaw, M. S., Romani, R. W., Cotter, G., Healey, S. E., Michelson, P. F., Readhead, A. C. S., Richards, J. L., Max-Moerbeck, W., King, O. G., and Potter, W. J.: 2013, ApJ **764**, 135

Shepherd, M. C.: 1997, in G. Hunt and H. E. Payne (eds.), *Astronomical Data Analysis Software and Systems VI*, Vol. 125 of *Astronomical Society of the Pacific Conference Series*, p. 77, San Francisco: ASP

Sokolovsky, K. V., Kovalev, Y. Y., Pushkarev, A. B., and Lobanov, A. P.: 2011, A&A **532**, A38

Stokes, G. G.: 1851, *Transactions of the Cambridge Philosophical Society* **9**, 399

Stratta, G., Capalbi, M., Giommi, P., Primavera, R., Cutini, S., Gasparrini, D., and on behalf of the ASDC team: 2011, *ArXiv e-prints*

The Fermi-LAT collaboration: 2019, *arXiv e-prints*

Thompson, A. R.: 1999, in G. B. Taylor, C. L. Carilli, and R. A. Perley (eds.), *Synthesis Imaging in Radio Astronomy II*, Vol. 180 of *Astronomical Society of the Pacific Conference Series*, p. 11

Thompson, D. J., Djorgovski, S., Vigotti, M., and Grueff, G.: 1992, ApJS **81**, 1

Tingay, S. J., Preston, R. A., Lister, M. L., Piner, B. G., Murphy, D. W., Jones, D. L., Meier, D. L., Pearson, T. J., Readhead, A. C. S., Hirabayashi, H., Murata, Y., Kobayashi, H., and Inoue, M.: 2001, ApJ **549**, L55

Urry, C. M. and Padovani, P.: 1995, PASP **107**, 803

Vermeulen, R. C. and Cohen, M. H.: 1994, ApJ **430**, 467

Vermeulen, R. C., Ogle, P. M., Tran, H. D., Browne, I. W. A., Cohen, M. H., Readhead, A. C. S., Taylor, G. B., and Goodrich, R. W.: 1995, ApJ **452**, L5

Wardle, J. F. C.: 2013, in *European Physical Journal Web of Conferences*, Vol. 61 of *European Physical Journal Web of Conferences*, p. 06001

A. Bias and Statistical Methods

A.1 Bias Avoidance

In 3.2.1, I briefly discuss the steps taken to avoid bias from the observational sampling. Here, I will go into more detail on why these steps were chosen and what alternatives were possible.

I began by compiling three statistics for each AGN: the total number of observations, the median length of time between consecutive observations, and the total length of time between the earliest observation and December 31st, 2016 (using only observations with polarization data). Graphs of these statistics are shown in Figures A.1, A.2, and A.3. The range between AGN is large for all of them, causing difficulties in large-scale comparisons. When computed from all available epochs, some of the statistics have a large dependence on the number of epochs available per source. An example of this is shown in Figure A.4.

Programs such UMRAO and OVRO have developed variability statistics dependent on a mean, taking advantage of the relatively consistent amount of time between epochs and greater number of observations (see e.g., Aller et al. 2003 and Richards et al. 2011). Restricting the sample in such a way to remove observational bias is simpler than attempting to define all used statistical measures in a way which represents all AGN accurately.

I first attempted to calculate the statistics from five randomly chosen epochs per source, in order to address the problem of the differing number of observations between sources. This was done with no constraints on the length of coverage time or the length of time between epochs. Figure A.5 is similar to Figure A.4, but with the total intensity variabilities found in this manner. An apparent correlation still exists. Evidence for why this occurred is shown in Figure A.6, where 2251+158/3C 454.3

undergoes over a decade of stability before long-term flaring. Neglecting to account for the discrepancies in overall coverage time led to preferentially high variability and fractional polarization maximums for long-observed sources, and the possibilities for spacing of the five random epochs led to occasionally large differences between random seeds. I therefore restricted most of the calculated quantities to not only a set number of epochs, but also a set number of years. Five epochs in a space of 2.3 years was achievable for the majority of sources in the sample, and led to reasonable spacings between epochs. The total intensity variabilities calculated by this final method are shown in Figure A.7. Although the medians in Chapter 3 were also tested for correlation with the three defined observational statistics, they did not show any dependence, and so were calculated without these limits.

The relationship between median fractional polarization and redshift is discussed to some extent in Section 3.2.2. The other statistical quantities analyzed in Chapter 3 had no correlation with redshift. This is not a universal finding or something that can be assumed. Richards et al. 2014 found an anti-correlation between total flux variability and redshift, while Angelakis et al. 2016 found a positive correlation between polarization variability and redshift in an optical band. While the intersection of the flux-limited samples has been handled with care (e.g. in 3.2.10), it is worth noting that redshift dependence in the form of the Malmquist bias is unavoidable, and we are limited to AGN that are bright enough to be observed with the VLBA.

A.2 Censored Data

One of the complications of this thesis was the handling of left-censored data points. Many of the measured polarizations, as discussed in Section 3.1, fell below the required threshold for a detection. In these cases, the accompanying fractional polarizations was considered to exist at or below an upper limit defined by the relevant polarization contour. Many studies throw such points out due to the difficulty of their inclusion in statistics; however, they are important sources of information. A simple

example is in Section 3.2.2, where the frequency of censored data points for radio galaxies is compared to the frequency for HSP BL Lacs.

The censored data points have been included in statistical measures when possible, but with more difficulty. For example, the median fractional polarizations from Section 3.2.2 were first calculated assuming all upper limits to be non-censored data points. Then, they were run through two flagging procedures. The first flagged any medians where at least half the points used in calculation were censored. The second flagged any medians where a censored data point existed above the calculated median. The first group were not used in any subsequent analysis. If an AGN belonged to the second group but not the first, I inspected it individually. In the majority of cases, a censored data point was also the maximum fractional polarization for that source, meaning that the calculated median was likely not accurate; if the median did appear accurate, however, it was included in analysis.

The rationale behind excluding upper limit treatment in Section 3.2.4 is somewhat subtle. The variability index described therein is essentially a measure of the minimum value subtracted from the maximum value. In a group of mixed censored and non-censored values, the true minimum is likely one of the left-censored points. If the variability index is calculated with the upper limit points assumed to be definite (i.e. non-censored), this estimates the minimum as higher than the probable actual value. If the calculation is done using only the non-censored data points, excluding each source's upper limit measurements, the same effect occurs to a greater degree. Although this procedures reduces the number of sources available in comparison, I therefore only calculated a variability index for sources with no upper limit points among the five used epochs of measurement.

A.3 Statistical Tests

Three statistical tests are used in this thesis: 1. KS tests for sample comparison; 2. correlation tests using Kendall's τ coefficient; and 3. the Peto & Peto modification

of the Gehan-Wilcoxon test for comparison of samples with censored values. The accompanying statistical software is stated in section 3.2.1. While the Anderson-Darling (AD) test is of increasing popularity, I have used the KS test when appropriate, due to its greater recognizability. Kendall's τ was chosen over e.g. Spearman's ρ because it is more nonparametric — it is more robust and less sensitive to ties, or repeated values (Press et al., 2002). This is particularly important for the EVPA and PA, since ties are more common when there is limitation to a range of 180° or 90° for ≈100s of values. Overall, however, they are rare enough that the choice of correlation coefficient should not affect significance.

The use of "p" refers exclusively to the probability of a result assuming the null hypothesis is true. All of the mentioned p-values are two-tailed; tests have been run without assuming significance in a certain direction. Two-tailed is most often specified in the text of other publications, and because it is the default for most software, it is likely the most used when not specified. Note that there has been no accounting for false positives arising from the number of tests in this thesis. E.g., if one hundred tests are run, a one percent probability result is expected to occur. This is one reason I have, therefore, taken care to state the approximate values of tests, rather than simply quantifying them as below or above the standard threshold of 0.05. Kendall's τ coefficient is also specified when applicable, and indicates the strength of the correlation on a scale from -1 to 1, with the former value indicating strong anti-correlation.

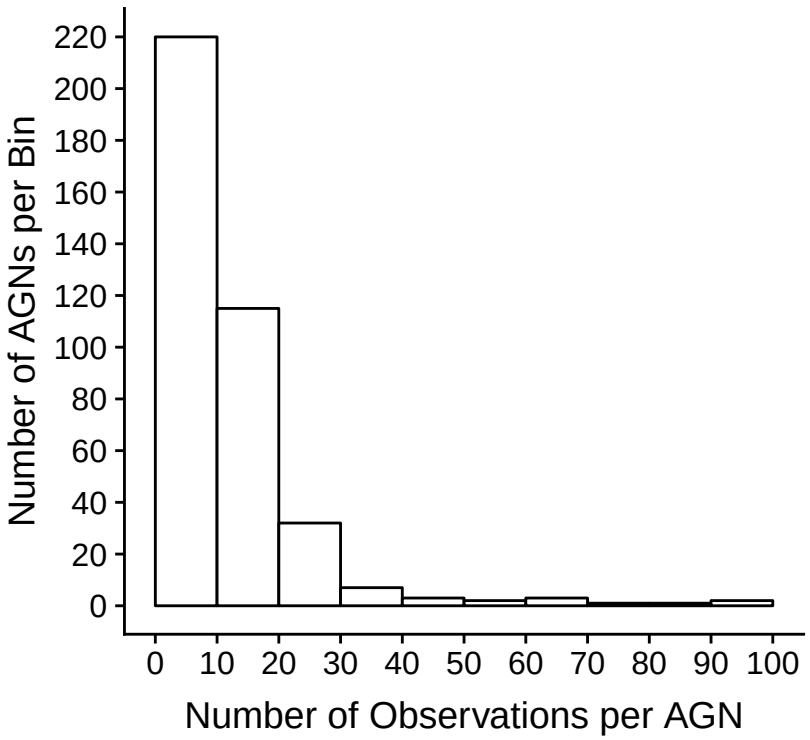

Figure A.1. Histogram of the number of epochs for each source with at least five measurements of polarization. 2200+420/BL Lac is an unshown outlier at 128 epochs.

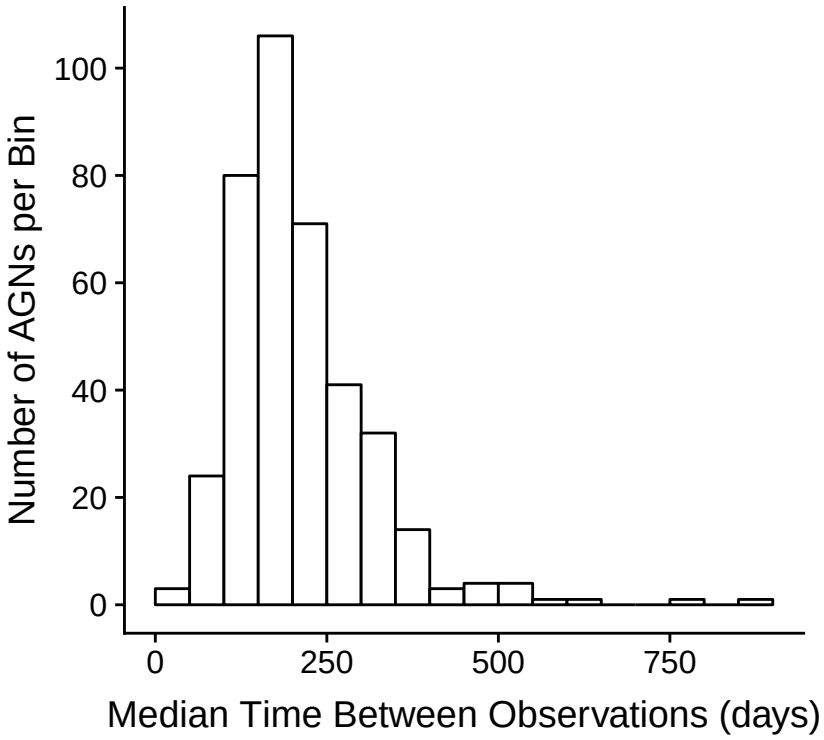

Figure A.2. Histogram of the median time in days between observing epochs for each source with at least five measurements of polarization. 2150+173/OX 183 is an unshown outlier at approximately 1400 days.

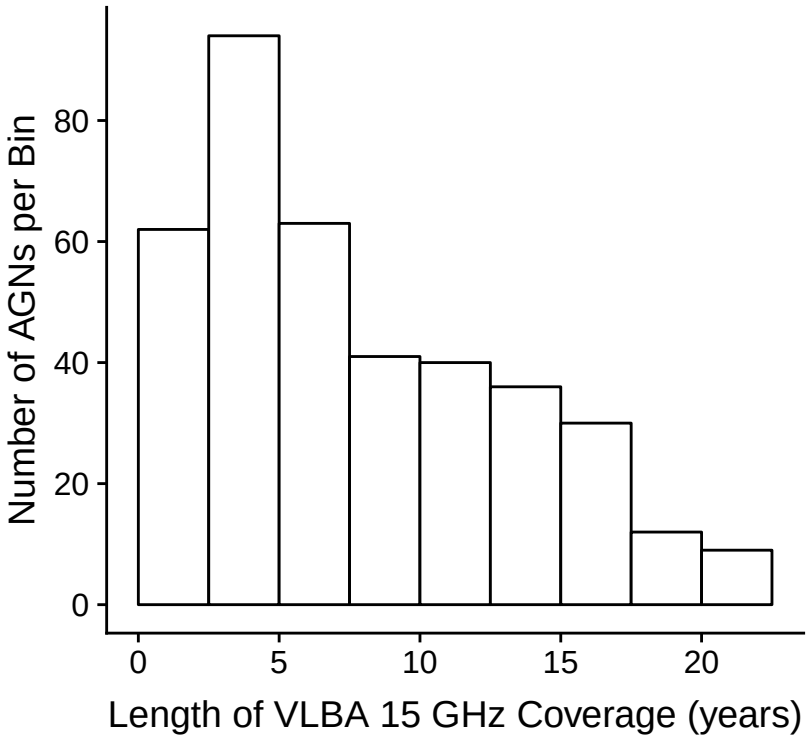

Figure A.3. Histogram of the total coverage time in years for each source with at least five measurements of polarization.

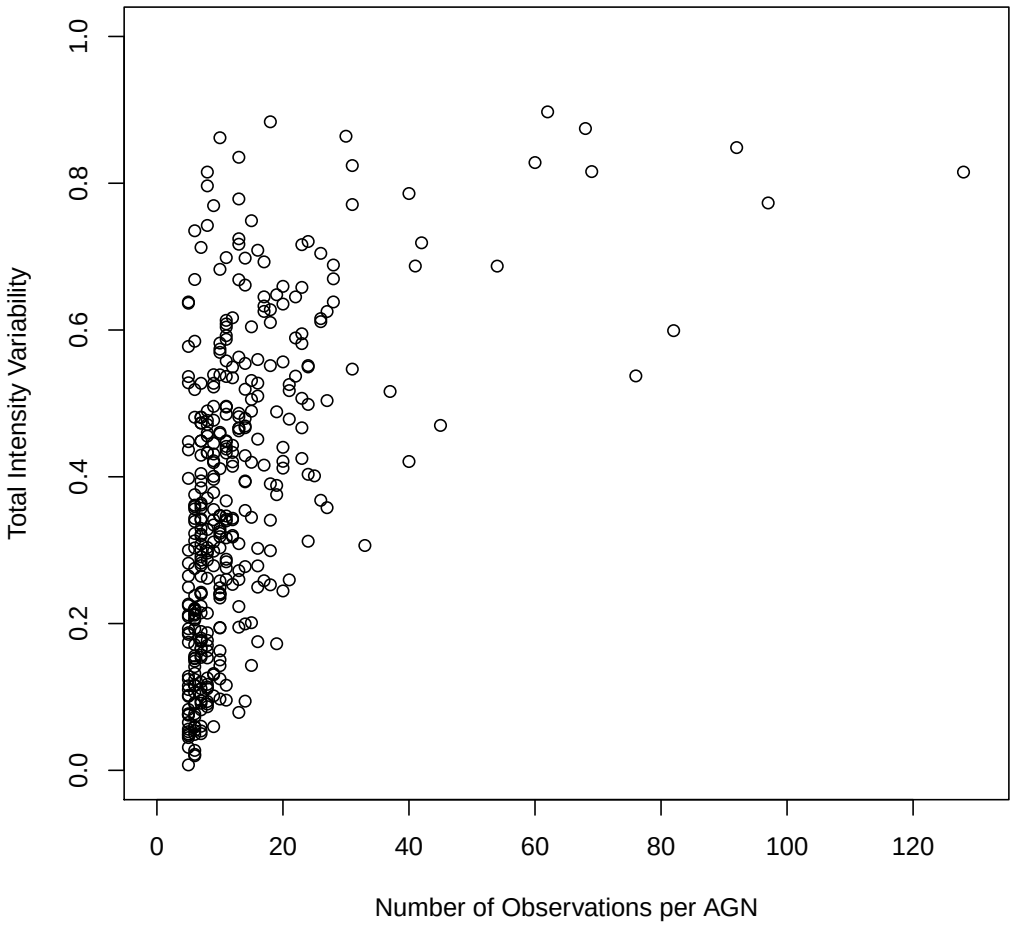

Figure A.4. Number of epochs per source versus the total intensity variability, with the latter calculated from all polarized epochs.

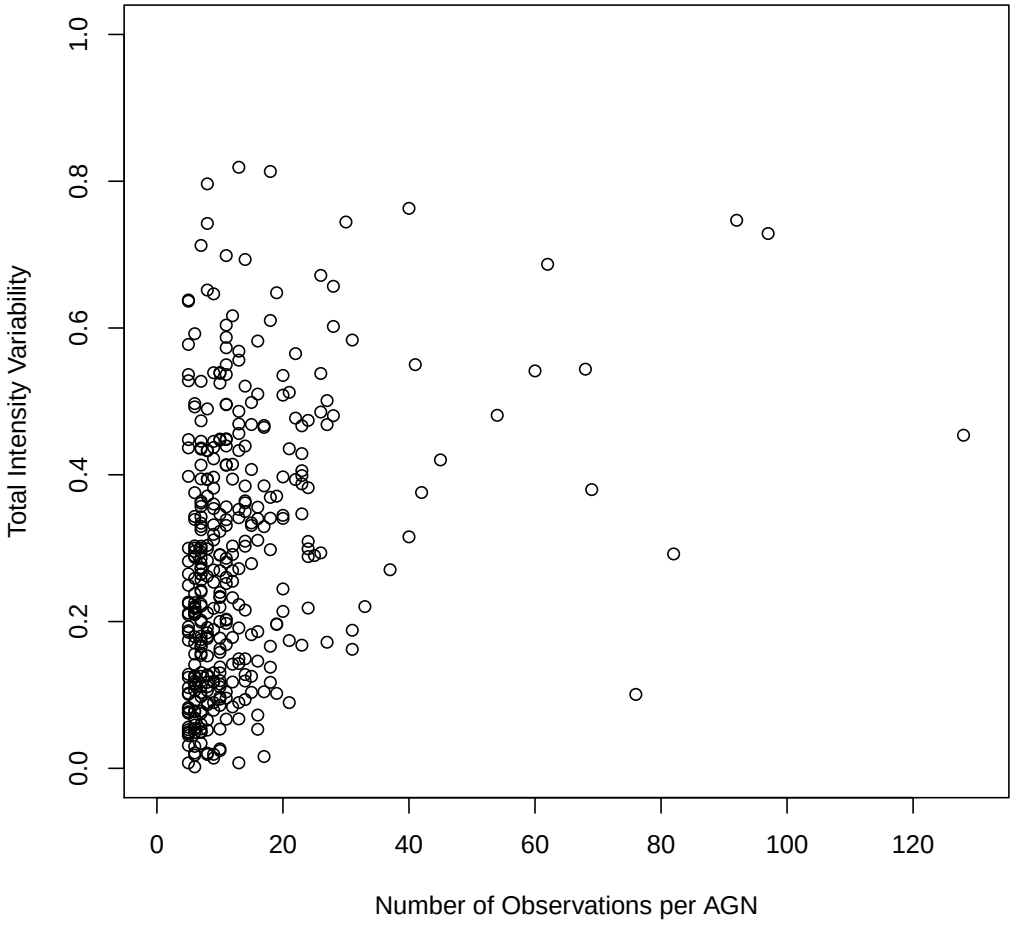

Figure A.5. Number of epochs per source versus the total intensity variability, with the latter calculated from five random epochs.

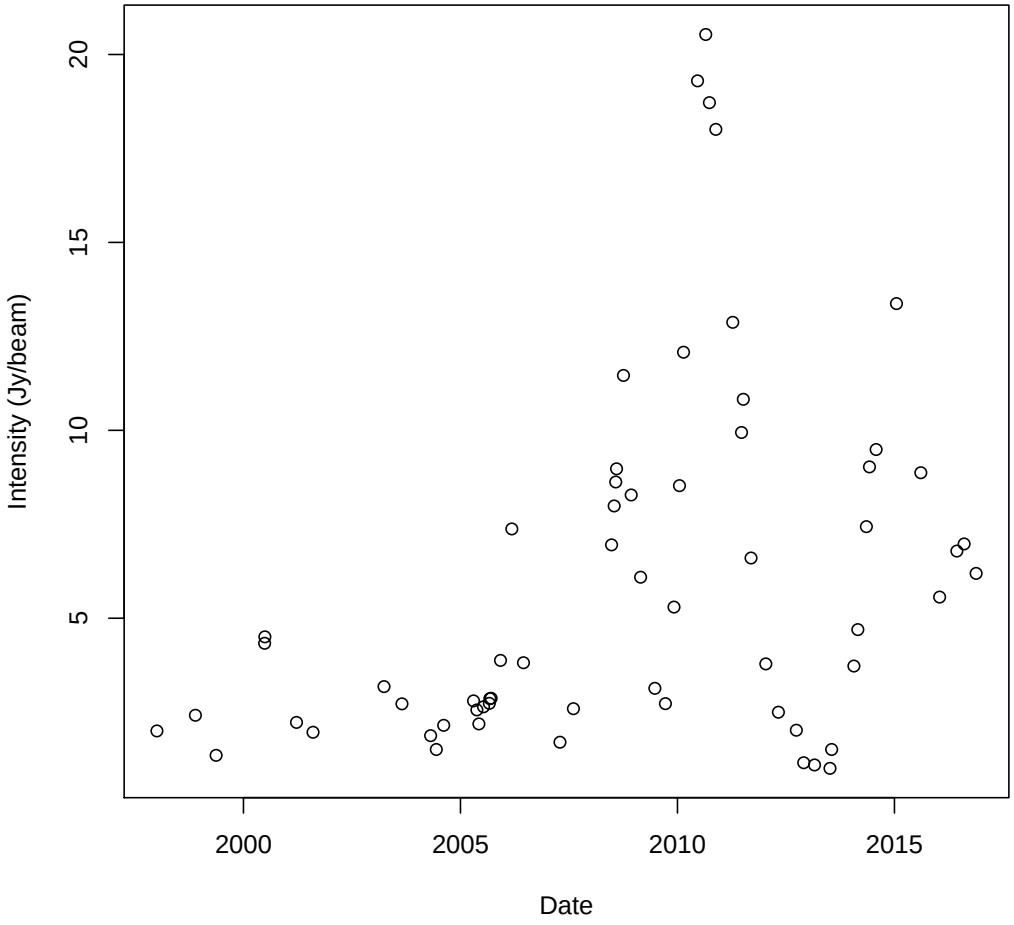

Figure A.6. Evolution of the core total intensity for 2251+158/3C 454.3.

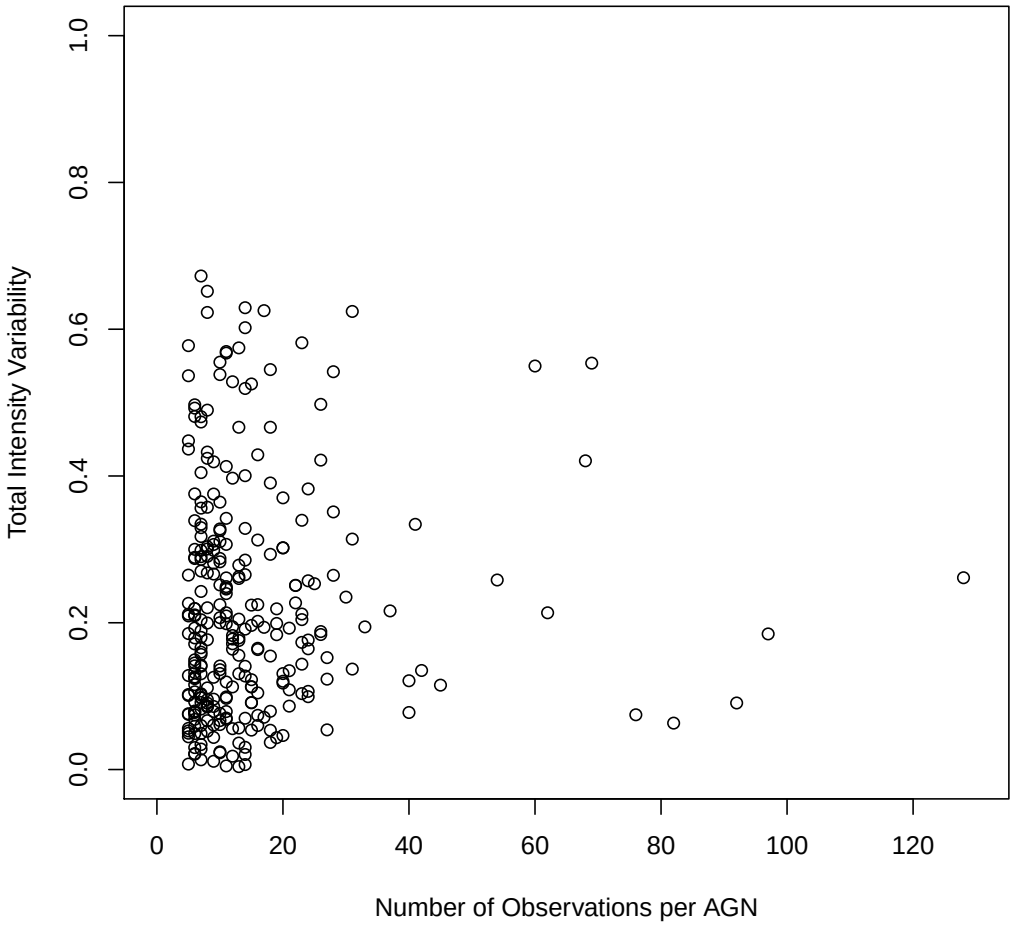

Figure A.7. Number of epochs per source versus the total intensity variability, with the latter calculated from five limited epochs based on the described observational bias corrections.